Spring 2013

Regional pulmonary function analysis using image registration and 4DCT

Kaifang Du
University of Iowa

REGIONAL PULMONARY FUNCTION ANALYSIS USING IMAGE REGISTRATION AND 4DCT

by

Kaifang Du

An Abstract

Of a thesis submitted in partial fulfillment of the
requirements for the Doctor of Philosophy
degree in Biomedical Engineering
in the Graduate College of
The University of Iowa

May 2013

Thesis Supervisors: Professor Joseph M. Reinhardt
Associate Professor John E. Bayouth

ABSTRACT

Current radiation therapy (RT) planning for limiting lung toxicity assumes a uniform distribution of lung function with little consideration to the spatial and temporal pattern of lung function. Establishment of relationships between radiation dose and pulmonary function change can help predict and reduce the RT-induced pulmonary toxicity. Baseline measurement uncertainty of pulmonary function across scans needs to be assessed, and there is a great interest to compensate the pulmonary function for respiratory effort variations.

Respiratory-gated 4DCT imaging and image registration can be used to estimate the regional lung volume change by a transformation-based ventilation metric which is computed directly from the deformation field, or an intensity-based metric which is based on CT density change in the registered image pair. In this thesis, we have evaluated the reproducibility of regional pulmonary function measures using two repeated 4D image acquisitions taken within a short time interval for both transformation-based and intensity-based metrics. Furthermore, we have proposed and compared normalization schemes that correct ventilation images for variations in respiratory effort and assess the reproducibility improvement after effort correction.

The major contributions of this thesis include: 1) develop and validate a process for establishing measurement reproducibility in 4DCT-based ventilation, 2) evaluate reproducibility of the transformation-based ventilation measurement, 3) evaluate reproducibility of the intensity-based ventilation measurement, 4) develop and

compare different ventilation normalization methods to correct for respiratory effort variation across scans.

Abstract Approved: _____

Thesis Supervisor

_____

Title and Department

_____

Date

_____

Thesis Supervisor

_____

Title and Department

_____

Date

REGIONAL PULMONARY FUNCTION ANALYSIS USING IMAGE REGISTRATION AND 4DCT

by

Kaifang Du

A thesis submitted in partial fulfillment of the
requirements for the Doctor of Philosophy
degree in Biomedical Engineering
in the Graduate College of
The University of Iowa

May 2013

Thesis Supervisors: Professor Joseph M. Reinhardt
Associate Professor John E. Bayouth

Graduate College
The University of Iowa
Iowa City, Iowa

CERTIFICATE OF APPROVAL

PH.D. THESIS

This is to certify that the Ph.D. thesis of

Kaifang Du

has been approved by the Examining Committee for the thesis requirement for the Doctor of Philosophy degree in Biomedical Engineering at the May 2013 graduation.

Thesis Committee: _____
Joseph M. Reinhardt, Thesis Supervisor

_____
John E. Bayouth, Thesis Supervisor

_____
Gary E. Christensen

_____
Madhavan L. Raghavan

_____
Edwin L. Dove

ACKNOWLEDGEMENTS

First and foremost, I would like to thank my advisors Prof. Reinhardt and Dr. Bayouth, for the huge support and guidance I have received throughout this work. I am most gracious to Prof. Reinhardt for his great help, inspiration-provoking conversations, and encouragement in tough times. I remember many times I received the revised manuscripts from him full of his meticulous handwritings. I am most fortunate to have become a student of Dr. Bayouth who has inspired me throughout my research with his passion, expertise, and invaluable advice. I appreciate Dr. Bayouth for introducing me to the exciting field of medical physics.

I would also like to thank Prof. Christensen. I have interacted with him throughout the entire project and I have benefited a lot from him. I would like to express my sincere gratitude to Dr. Kai Ding, who directed me step-by-step to lung research and medical physics. He helped me a lot in both work and life, with his aggressive research spirit, profound knowledge and optimistic heart. We had many informative discussions and he is always willing to provide assistance. A special thanks goes to Dr. Kunlin Cao for her help on image registration. Prof. Raghavan and his student Ryan Amelon deserve a special thanks for the talented suggestions on lung mechanical analysis. In addition, I would like to thank Prof. Edwin Dove for serving on my committee.

Thanks too to my lab mates and friends Xiayu Xu, Panfang Hua, Lijun Shi, Vinayak Joshi, Tarunashree Yavarna, Sandeep Bodduluri, Richard Amendola, and

Yang Wook Kim, who have made the last few years fun and enjoyable. Li Zhang, Xin Dou, Shanhui Sun, and Mingqing Chen deserve a special thanks for the great help.

Finally, last but not least, I would like to extend a special thanks to my grandmother, my parents and my little sister for all of their love and support. A very special thank you to Zhen Yuan, for your patience, understanding and encouragement.

This work was supported in part by grants HL079406, HL064368, and EB004126 from the National Institutes of Health and by a University of Iowa Carver College of Medicine Pilot Grant.

ABSTRACT

Current radiation therapy (RT) planning for limiting lung toxicity assumes a uniform distribution of lung function with little consideration to the spatial and temporal pattern of lung function. Establishment of relationships between radiation dose and pulmonary function change can help predict and reduce the RT-induced pulmonary toxicity. Baseline measurement uncertainty of pulmonary function across scans needs to be assessed, and there is a great interest to compensate the pulmonary function for respiratory effort variations.

Respiratory-gated 4DCT imaging and image registration can be used to estimate the regional lung volume change by a transformation-based ventilation metric which is computed directly from the deformation field, or an intensity-based metric which is based on CT density change in the registered image pair. In this thesis, we have evaluated the reproducibility of regional pulmonary function measures using two repeated 4D image acquisitions taken within a short time interval for both transformation-based and intensity-based metrics. Furthermore, we have proposed and compared normalization schemes that correct ventilation images for variations in respiratory effort and assess the reproducibility improvement after effort correction.

The major contributions of this thesis include: 1) develop and validate a process for establishing measurement reproducibility in 4DCT-based ventilation, 2) evaluate reproducibility of the transformation-based ventilation measurement, 3) evaluate reproducibility of the intensity-based ventilation measurement, 4) develop and

compare different ventilation normalization methods to correct for respiratory effort variation across scans.

TABLE OF CONTENTS

LIST OF TABLES

Table

LIST OF FIGURES

Figure

CHAPTER 1

INTRODUCTION

Lung cancer is the biggest cancer killer of the human for both men and women [3], making up to about 29% of cancer caused deaths [4, 5]. Up to half of lung cancer patients chose to receive radiation therapy (RT) after tumor diagnosis [3]. Studies have found higher radiation dose improves the overall survival after RT [6, 7]. However, to irradiate and kill the lung tumors, normal lung tissue will also be irradiated [5]. Patients after RT often develop some degree of lung injury, with an associated decline in pulmonary function, tissue pneumonitis or tissue fibrosis. Patients may benefit from less lung toxicity and preserve more pulmonary function after therapy if the regions that are high-ventilated during respiration or more sensitive to radiation can be avoided or less irradiated in RT. The compromise between the two purposes of minimizing RT-induced lung toxicity and preserving more lung function creates a necessity to investigate the spatial and temporal pattern of lung function.

The current RT paradigm for limiting lung toxicity is based on the dose-volume relationship of the treated lung. Two predictors currently utilized in RT planning are the volume of lung receiving at least 20 Gy [8] and the mean radiation dose delivered to normal lung tissue [9, 10]. Current radiation toxicity estimation is based on a uniform lung function and little consideration has been given to spatial and temporal pattern of lung function. Regions of normal lung tissue with high ventilation can be avoided from radiation if we know the regional pulmonary function pattern. The

cancer can also be better treated with more focused radiation dose. A more accurate RT planning model should consider both the volume and the pulmonary function capacity of the portions of irradiated lung. Since 4DCT has become a routine examination for lung cancer RT treatment planning, it would be convenient to utilize 4DCT combined with image registration to generate high resolution ventilation map, which has been investigated by several groups [11, 12, 13, 14, 15]. The overall motivation of the study is to derive and model regional pulmonary function with 4DCT and image registration for use in radiation therapy of lung cancer. Currently, the complex inter-relationships between RT treatment schemes and pulmonary function change before and after RT are poorly defined. Meanwhile, to measure the real pulmonary function change caused by radiation, we need to establish the overall reproducibility of the method that is used to measure the regional pulmonary function. It is also worth investigating into the normalization schemes that correct ventilation images for variations in respiratory effort and their affect on change of the reproducibility after respiratory effort correction.

In this chapter we give a brief introduction to the general background of this study, such as respiratory physiology, pulmonary function imaging, and image processing, etc. Comprehensive literature reviews are presented in each section to show findings in previous studies and significance of our research work.

1.1 Respiratory Physiology

Breathing is vital for human life. During breathing oxygen is inhaled into the body and carbon dioxide is expelled from the body [16]. As a crucial component of

respiratory system, lung is the site of gas exchange. The lung tissue consists of mixed structures such as bronchioles, bronchi, blood vessels, interstitium, and alveoli [2]. During each respiratory cycle, the lung undergoes tissue expansion and contraction, driven and facilitated by the ventilatory pump including the chest wall, diaphragm, inspiratory and expiratory muscles, and related neural controls of breathing [17]. The lung and chest wall have natural tendencies to recoil [18]. During lung expansion, if the atmospheric pressure is considered to be zero as reference, the respiratory muscles and diaphragm generate a negative enough intrapleural pressure within the thorax to overcome the recoiling force and increase the lung volume. The lung expansion creates a negative pressure within the lung alveoli relative to atmospheric pressure, resulting in oxygen-rich air-flowing into the lung through conducting airways [2]. Within the lung, the air reaches the respiratory zone, composed of alveoli, through the transitional zone, which consists many generations of airways and bronchioles [2]. The alveoli are the sites of gas exchange, where the oxygen in the alveoli exchanges with carbon dioxide in the venous blood in the pulmonary capillaries surrounding each alveolus, in the passive diffusion way [19]. The whole process is shown in Figure 1.1. In the opposite direction, the exchanged air rich in carbon dioxide is expelled to the environment during lung contraction, which mainly depends on the recoiling force. The constant, synchronous functioning of the breathing system ensures reliable gas delivery for whole body.

Many lung diseases affect pulmonary function by changing the tissue material and mechanical properties. For example, pulmonary emphysema, a component

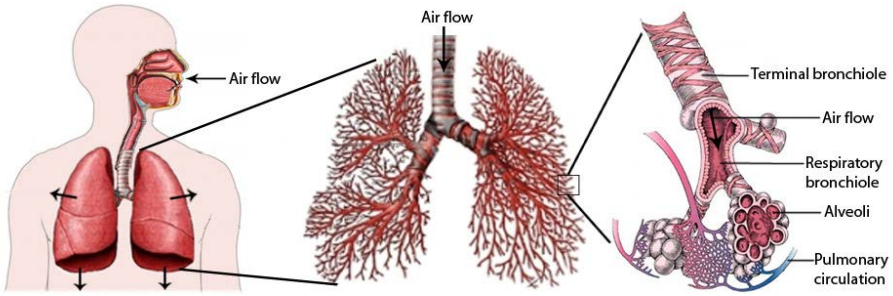

Figure 1.1. Lung function process illustration, from [20].

of chronic obstructive pulmonary disease (COPD), results from tissue elasticity decline (increased tissue compliance) with destruction of the structures supporting the alveoli and destruction of the capillaries feeding the alveoli [21, 2]. In the other direction, one interstitial lung disease called idiopathic pulmonary fibrosis (IPF) can cause symptoms of lung inflammation and fibrosis by making lung tissue thicker and stiffer (reduced tissue compliance). Lung breathing ability and breathing pattern can also be impacted and influenced by lung cancers [22]. Lung tumors may result in occlusion of the major airways causing breathlessness. 60% of lung cancer patients have dyspnea with associated symptoms including chronic cough and sputum production or hemoptysis [23, 24]. Radiation therapy can be curative, but may also bring damage to the lung and cause significant decline in lung function accompanied with many other symptoms [25]. Due to the sensitivity of the lung to radiation dose, unintended radiation-induced lung injury has been the major limit of therapeutic doses to lung cancer [26]. Figure 1.2 illustrates stages of radiation-induced lung injury. The radiation-induced lung injury in the intermediate acute phase and in the late and chronic phases are respectively marked by radiation pneumonitis and radiation

fibrosis, both of which may alter pulmonary function [27]. Since lung diseases and treatment are all associated with changes in lung tissue mechanics, it would be very helpful to develop a method to look into the regional mechanics which determine regional pulmonary function.

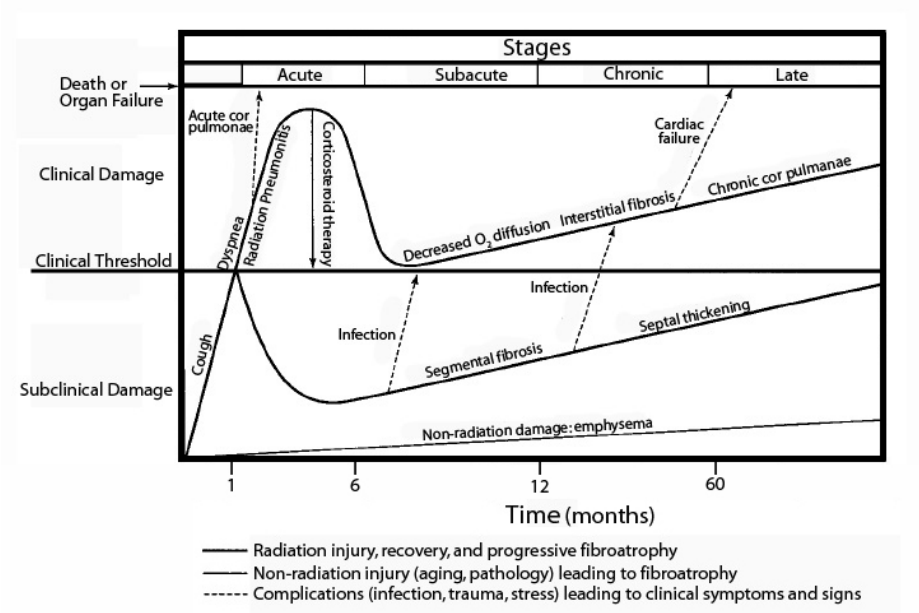

Figure 1.2. Stages of radiation-induced lung injury, from [28].

1.2 The Pulmonary Function Test

Current clinical methods for evaluating global lung function include spirometry, plethysmography, and diffusing capacity of carbon monoxide (DL_{CO}), etc. Despite the fact that these tests are easy to administer and can help in the diagnosis and the management of patients with pulmonary or cardiac diseases, they are highly effort dependent, and cannot reflect regional pulmonary function. A very simple but useful

test of lung function is FEV_1 test, measured in a single forced expiration in one second (Figure 1.3) [29]. The subject is asked to inhale maximally and then exhale as hard and as completely as he or she can. The volume of air exhaled in the first second is called FEV_1 (forced expired volume in 1 second), and the total volume exhaled in the forced expiration is the forced vital capacity (FVC) [29]. Normally, the FEV_1 is about 80% of the FVC. In restrictive diseases such as pulmonary fibrosis, both FEV_1 and FVC reduce, but the FEV_1/FVC% may be normal or even increased. In obstructive diseases such as bronchial asthma, FEV_1 reduces much more than FVC, giving a low FEV_1/FVC% [29].

Plethysmography is a lung test that is performed to see how much air the lung can hold and to compute static lung volumes following Boyle's Law. Lung volumes and capacities are illustrated in Figure 1.4, including tidal volume (TV), volume inspired or expired within a normal breath; inspiratory reserve volume (IRV), maximum volume that can be inspired over a normal tidal inspiration; expiratory reserve volume (ERV), maximal volume that can be expired after a normal tidal expiration; residual volume (RV), volume that resides in the lung after a forced maximal expiration; inspiratory capacity (IC), volume inhaled from tidal expiration to forced maximal inspiration; functional residual capacity (FRC), volume that remains in lung after a normal expiration; vital capacity (VC), volume difference between maximal inspiration and maximal expiration; total lung capacity (TLC), volume of the lung after forced maximal inspiration [2].

DL_{CO} is a measurement of diffusion of gas passing from lung alveoli into the

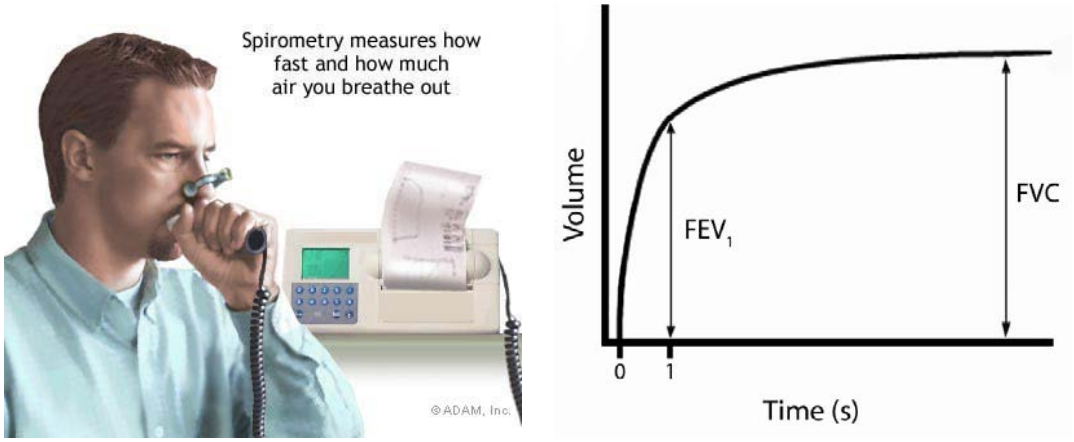

(a) (b)

Figure 1.3. Pulmonary function test. (a) A spirometer, from [30]. (b) Corresponding sample airflow curve during the forced expiration.

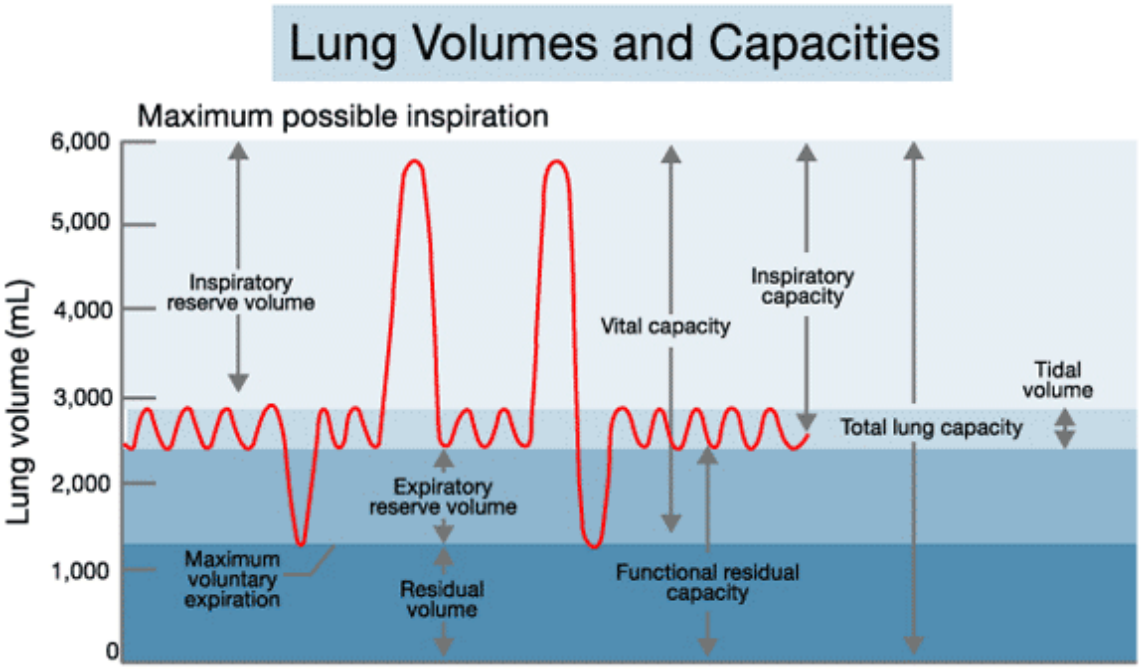

Figure 1.4. Concepts of lung volumes and capacities, from [31].

blood. The transfer of carbon monoxide is limited solely by diffusion, it is therefore the gas of choice for measuring the diffusion properties of the lung [19]. DL_{CO} means the volume of carbon monoxide transferred in milliliters per minute per mm Hg of alveolar partial pressure. DL_{CO} can be calculated from the inspired and expired concentration measurements of carbon monoxide in a dilute mixture. Similar to other diffusion measurements, DL_{CO} is related to the area and thickness of blood-gas barrier, and the blood volume in pulmonary capillaries [19].

1.3 Regional Pulmonary Function Measurement

The pulmonary function in the lungs is not homogeneous. However, the clinical pulmonary function test (PFT) cannot reveal regional differences. Various methods have been developed for regional lung function analysis. Invasive methods, such as percutaneously or surgically implanted parenchyma markers or inhaled fluorescent microspheres, are effective but not suited for translation to humans [32, 33, 34, 2]. Noninvasive methods include medical imaging approaches. Positron emission tomography (PET) and single photon emission computed tomography (SPECT) can provide a direct assessment of lung function [35, 36, 37, 38], but their application is limited by low spatial resolution [2]. Hyperpolarized noble gas MR imaging (such as ^{129}Xe and ^{3}He) has also been developed for functional imaging of pulmonary ventilation [39, 40, 41, 42, 43]. Hyperpolarized MRI can provide enough temporal resolution to observe the dynamics of gas flow through the lung. However, the method is only partially quantitative and depicts very little anatomic detail. Xenon-enhanced CT is another imaging modality that can directly assess pulmonary ventilation by observing

the wash-in and wash-out rates from series of CT images [44, 45, 46]. The need for extremely high temporal resolution to measure the wash-in/wash-out time constants limits the overall axial coverage to about 12 to 15 cm in the lung for the method of Xenon-CT.

With the development of multi-detector-row computed tomography (MDCT) and 3D non-rigid image registration, many groups have turned to pulmonary function analysis in the perspective of lung tissue mechanics, which in turn determine regional lung function. Guerrero et al. used an optical-flow registration to compute the ventilation map from 4DCT [13, 47]. After identifying corresponding voxels across the 4DCT data set by the optical flow image registration, the local ventilation (represented by change in fraction of air per voxel) was calculated from local averaged CT values. The calculated ventilation was summed and then compared to global lung volume change for validation. Christensen et al. applied image registration to cine-CT sequences and estimated local lung tissue expansion and contraction rate by Jacobian determinant [48]. Their study shows regional pulmonary measurements matched well with spirometry test. In four of five individuals, over multiple breathing periods, the mean log-Jacobian and the air flow rate correlated well for entire lung ($r^2 = 0.858$). Additionally, the mean log-Jacobian and the air flow rate near the diaphragm correlated well in all five individuals ($r^2 = 0.943$) [48]. Reinhardt et al. [11] compared the registration-based estimation on regional lung function to Xenon-CT and the average r^2 reached 0.73. Fuld et al. [49] validated registration-based regional specific volume change against Xenon-CT specific ventilation in four anesthetized and mechanically

ventilated sheep. Yamamoto et al. [50] presented the correlation between intensity-based ventilation and emphysema regions, indicating potential physiological use of the intensity-based ventilation. Castillo et al. [14] used image registration to compute both transformation-based and intensity-based measures of local lung function and compared them to SPECT functional measures. Their results demonstrated the mathematical equivalence of analytic and geometric Jacobian metrics for quantifying volume change, and show both methods correlate well with global ventilation measurements and the clinical SPECT [14]. Recently, Mathew et al. [51] observed good spatial and significant quantitative agreement for ventilation maps on hyperpolarized ^{3}He MRI and 4DCT imaging, despite rather large differences in image acquisition breathing maneuvers. All of the above results support the use of 4DCT and image registration to measure the regional pulmonary function.

1.4 4DCT Imaging

4D (3D + time) multi-detector CT imaging technology can provide a series of 3D volumetric image data at different respiratory states [52]. Though modern multi-detector scanners can acquire multiple slices at a time, due to spatial-temporal limitations of CT scanners, currently the entire lung cannot be imaged thoroughly in single respiratory cycle. Therefore, to obtain 4D time-resolved information during periodic lung motion, raw projection data must be collected at each couch position for a time interval equal to or longer than the duration of a full respiratory cycle [53]. Such continuous data acquisition per couch position can be achieved by scanning in either axial cine mode at a given couch position or in helical mode with couch moving

at a very low pitch.

In cine mode, the couch does not move during data acquisition for each couch position. After data acquisition at one couch position is completed, x rays are turned off and the couch advances to begin data acquisition again at next couch position until full coverage of the scan length has been obtained [54]. In helical mode, the image data are acquired in sequence with the continuous moving of couch [52]. During imaging the couch moves at a low enough pitch that enough number of slices can be collected for a full respiratory cycle [52]. If the CT tube rotation time is short compared to the period of motion, CT data acquisition can be finished over several tube rotations.

After data acquisition, 3D CT volumes at different respiratory states can be reconstructed by resorting and assembling the acquired data, with retrospective gating technology and according to simultaneously recorded internal or external respiratory surrogate signals [55]. In helical mode, because of the multi-detector scanner, a slab or image stack is formed from the 2D image slices acquired at each couch position, covering only part of the lung at a certain respiratory phase. Then in the reconstruction stage, the image stacks from all respiratory cycles associated with the same specific respiratory phase are stacked up and combined to form a complete 3D CT volume at that phase [52]. By viewing temporally the 3D images in all sequential phases, the reconstruction of a 4DCT image is complete (see Figure 1.5).

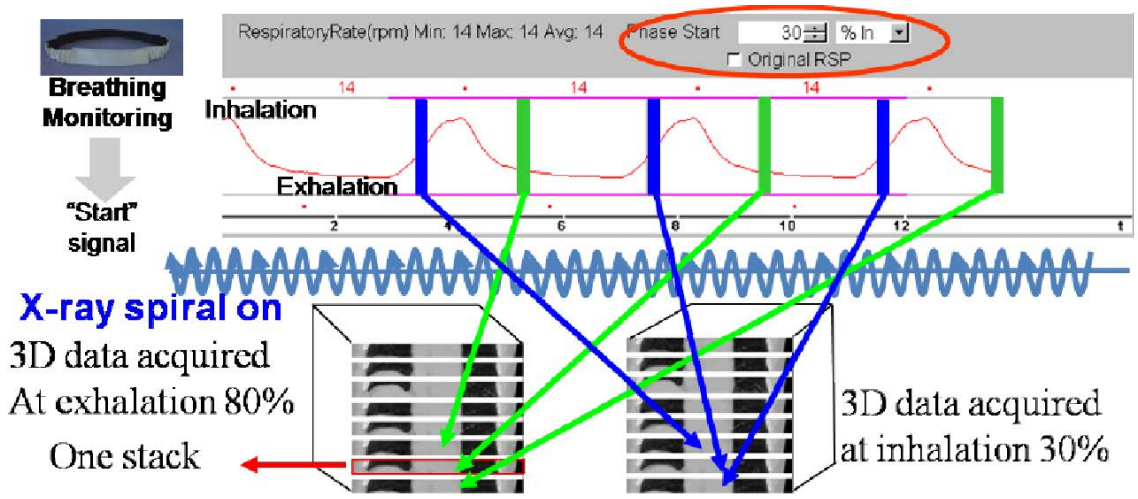

Figure 1.5. Illustration of 4DCT imaging. 4DCT image set includes series of 3D CT volumes at each reconstructed respiratory phase. A number of 2D slabs (or stacks) from multiple respiration cycles are reassembled to reconstruct the 3D CT volumes for each phase, according to the external respiratory surrogate. Figure is from [56].

1.5 Image Registration

Lung mechanics and regional pulmonary function information can be extracted from the motion of lung tissue from one breathing stage to another. Therefore first we need to map each image voxel to the corresponding voxel in the associated image. The problem can be solved by image registration whose task is to find the spatial transform that maps each point in one image to corresponding position in another image, as shown in Figure 1.6. Various image registration algorithms have been developed. The basic components of parameterized registration framework is shown in Figure 1.7 [57, 58].

1.5.1 Images

The registration framework usually requires two input images. One image is defined as the *moving* or *template* image I_1 and the other image as the *fixed* or *target*

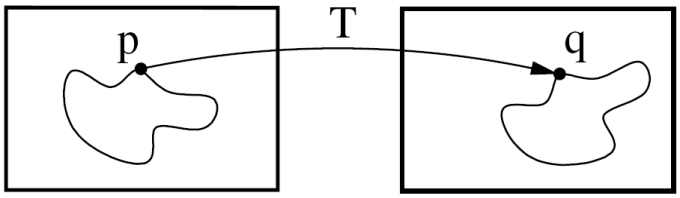

Figure 1.6. Image registration is an optimization problem that generates a spatial transformation mapping each point in one image to its correspondence in another image. Figure is from [57].

image I_2 [2]. The whole registration process can be considered as an optimization problem to find the best spatial mapping that aligns the moving image to the fixed image. Usually, a multi-resolution strategy is employed to speed up the registration and enhance the algorithm robustness. The multi-resolution strategy starts from registering the low resolution images of original input images [2, 59]. Then the acquired transform at the low resolution level will be used as initial input transform of the next higher resolution level. In this way, the transform is computed step by step from coarse to fine until reaching the last level. The final transform is computed at the finest level.

1.5.2 Transform

We use $\mathbf{h}(\mathbf{x})$ to indicate the transformation model which deforms each point in one image to its corresponding point in another image. The vector $\mathbf{x} = (x_1, x_2, x_3)^T$ is the voxel coordinate in one image. In order of increasing allowed flexibility, the transform models that can be used in image registration are translation, rigid, similarity, affine, nonrigid B-spline and nonrigid thin-plate spline-like transformations [59]. Among the non-rigid transformation models, B-splines [60] is widely

used in deformable registration of medical images like lung CT images. If we use $\phi_i = [\phi_x(\mathbf{x}_i), \phi_y(\mathbf{x}_i), \phi_z(\mathbf{x}_i)]^T$ to represent the coefficients of the i-th control point $\mathbf{x}_i$ on the spline grid G in each direction [61], then the transformation is represented as

$$\mathbf{h}(\mathbf{x}) = \mathbf{x} + \sum_{i \in G} \phi_i \beta^{(3)}(\mathbf{x} - \mathbf{x}_i), \tag{1.1}$$

Where ϕ_i describes the displacement information of controlling nodes on the image grid and $\beta^{(3)}(\mathbf{x})$ is a three dimensional tensor product of cubic B-spline basis functions [62]. $\beta^{(3)}(\mathbf{x})$ is defined as

$$\beta^{(3)}(\mathbf{x}) = \beta^{(3)}(x)\beta^{(3)}(y)\beta^{(3)}(z), \tag{1.2}$$

Where $\beta^{(3)}(\mathbf{x})$ is a separable convolution kernel. In the uniform cubic B-Spline model [62] the basis function is defined as

$$\beta^{(3)}(x) = \begin{cases} (4 - 6x^2 + 3|x|^3)/6, & 0 \le |x| < 1 \\ (2 - |x|)^3/6, & 1 \le |x| < 2 \\ 0, & |x| \ge 2 \end{cases} \tag{1.3}$$

$\beta^{(3)}(y)$ and $\beta^{(3)}(z)$ would have similar forms as $\beta^{(3)}(x)$.

1.5.3 Cost Function

The cost function measures how well the moving image is matched with the fixed image based on current transformation, and is passed into the optimizer for computing parameters of the transformation for the next iteration. A simple cost function metric commonly used is the sum of squared difference (SSD), which measures squared difference of CT Hounsfield units (HU) at paired corresponding points between two images [2]. It is defined as

$$C_{\text{SSD}} = \int_{\mathbf{\Omega}} \left\{ [I_2(\mathbf{x}) - I_1(\mathbf{h}(\mathbf{x}))]^2 \right\} d\mathbf{x}. \tag{1.4}$$

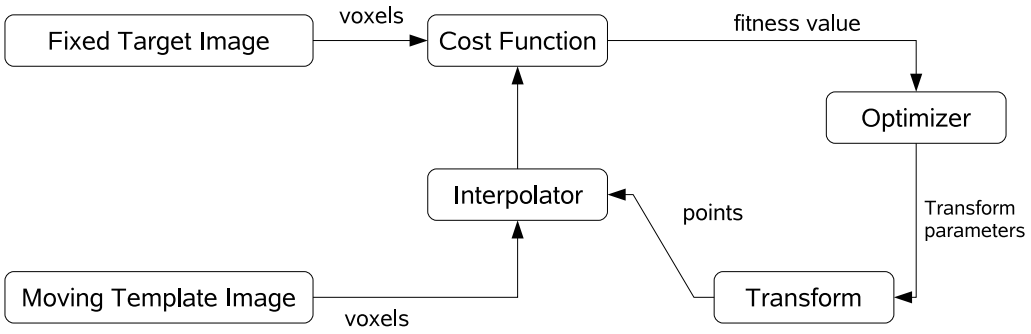

Figure 1.7. The framework of registration includes basic components as two input images (the fixed and the moving), a transform, a cost function, an interpolator and an optimizer, from [57].

A more complicated cost function metric, the sum of squared tissue volume difference (SSTVD) [63, 64, 65], has been specially designed to account for the intensity change in lung CT images. This cost function metric minimizes local difference of the lung tissue volume across different air pressure levels by improving the SSD metric to consider the fraction of tissue volume instead of the total volume of tissue and air [61]. Assume the HU of CT lung images is primarily formed by linear combination of tissue and air [12], then the tissue volume in a voxel at position $\mathbf{x}$ can be estimated as $\mathrm{V}(\mathbf{x}) = \mathrm{v}(\mathbf{x})\frac{\mathrm{HU}(\mathbf{x})-\mathrm{HU}_{\mathrm{air}}}{\mathrm{HU}_{\mathrm{tissue}}-\mathrm{HU}_{\mathrm{air}}}$ where $v(\mathbf{x})$ is the volume of voxel $\mathbf{x}$ [61]. If we assume $\mathrm{HU}_{\mathrm{air}} = -1000$ and $\mathrm{HU}_{\mathrm{tissue}} = 55$ [61], the cost function metric SSTVD is defined as

$$\begin{aligned} C_{\mathrm{SSTVD}} &= \int_{\mathbf{\Omega}} \left[V_2(\mathbf{x}) - V_1(\mathbf{h}(\mathbf{x}))\right]^2 d\mathbf{x} \\ &= \int_{\mathbf{\Omega}} \left[v_2(\mathbf{x})\frac{I_2(\mathbf{x})+1000}{1055} - v_1(\mathbf{h}(\mathbf{x}))\frac{I_1(\mathbf{h}(\mathbf{x}))+1000}{1055}\right]^2 d\mathbf{x} \end{aligned} \quad (1.5)$$

Other than intensity-based cost function metrics, feature-based information

can also be included in the cost function to help guide the image registration process. For example, the preservation of tubular shape and the tree structure of lung blood vessel can be utilized to improve algorithm accuracy [66]. There are also other proposed cost function metrics for different applications, such as mutual information (MI), normalized correlation coefficient (NCC), normalized mutual information (NMI), and kappa statistic (KS), etc [59].

1.5.4 Optimization

The solution of the optimization problem in image registration is to obtain the optimal transformation parameters after the transformation in the previous iteration moves in an optimized direction with a controlled step size. A limited-memory, quasi-Newton minimization method with bounds (L-BFGS-B) [67] algorithm is commonly used in B-spline based registration [61]. By constraining the search space of parameters, certain properties are preserved during the optimization process. Choi and Lee [68] have proven the sufficient conditions to guarantee the local injectivity (one-to-one mapping property) of functions parameterized by uniform cubic B-Splines. The B-spline coefficients are constrained to ensure and maintain the transformation topology of the two images during the optimization [2].

1.5.5 Interpolator

The intensity interpolation is needed for evaluation at non-voxel positions after intermediate transformations. Several methods can be used for interpolation with difference in quality and speed [59]. The nearest neighbor is the most simple technique and requires least computing resources, but it is low in quality. The returned value

of linear interpolator is a weighted average of the surrounding (neighborhood) voxels. B-spline interpolator with higher order requires more computation time [59]. Actually, the nearest neighbor and linear interpolation can also be considered as B-spline interpolator as the special cases when $N = 0$ and $N = 1$ respectively. To generate the deformed image at the final iteration of registration, higher-order interpolation ($N = 3$) is usually used [59].

1.5.6 Algorithms

A number of registration algorithms have been developed for lung CT images in the past few years. Modat et al. [69] developed the NiftyReg package. Ourselin et al [70] proposed a block-matching technique in the global stage and a free-form deformation (FFD) algorithm in the local stage. Staring et al. [71] proposed to maximize the normalized correlation coefficient during registration. Hybrid feature-constrained deformable registration was developed by Han et al. [72]. Diffeomorphic transformation and cross correlation cost function were proposed by Song et al. [73]. Kabus et al. [74] combined the cost function of sum of squared differences and the Navier-Lame operator as a regularization term in multi-resolution strategy. Yin et al. [63] proposed mass preserving nonrigid registration of lung CT images using a cubic B-spline transformation model. Guerrero et al. [75] proposed image registration using 3D optical flow method. The diffeomorphic morphons and diffeomorphic demons registration methods using morphons were also proposed [76, 77]. Cao et al. [62] presented a nonrigid registration algorithm combining a new vesselness similarity and SSTVD for cost function to improve registration accuracy for lung CT images.

Some research groups have started to investigate 4D image registration to preserve the spatial-temporal smoothness of tissue motion [78, 79, 80, 81, 82].

After image registration, we should have obtained a voxel-by-voxel transformation. Based on the transformation matrix, many mechanical and mathematical analysis can be performed for tracking the regions of interest of the lung at difference conditions.

1.6 Lung ventilation and mechanics measures

After image registration, we acquire a displacement field that maps the corresponding points in the fixed and moving image. The displacement field can be used to assess regional lung ventilation (volume change) and regional tissue motion pattern (stretch and strain, anisotropy, etc).

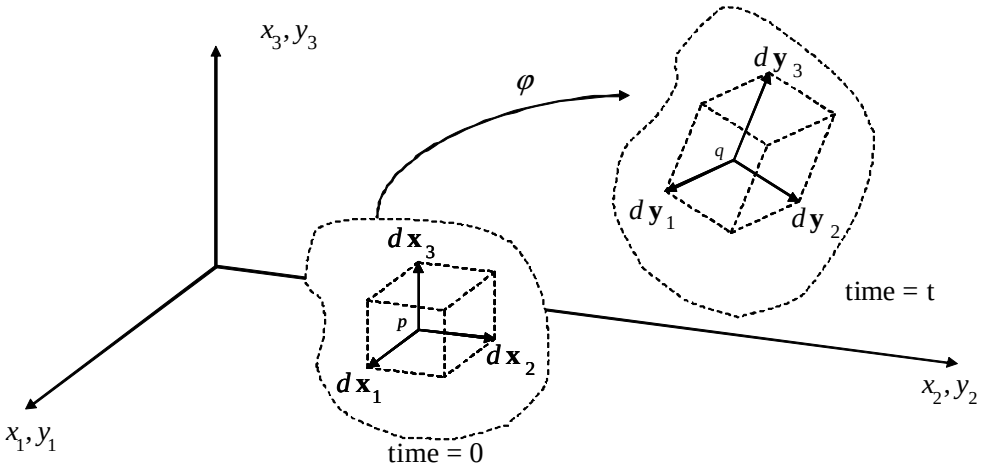

Figure 1.8. Deformation of a continuum body from reference configuration (left) at time t_0 to current configuration at time t (right), from [1, 2].

Figure 1.8 shows a continuum body deforms from the reference configuration

at time t_0 to current configuration at time t, generating deformation or transformation φ [1, 2]. Suppose domain $\Omega \in \mathbb{R}^3$ represents the set of points in the reference configuration of a moving body at time t_0, and $\mathbf{x} \in \Omega$ is one material point. At time t, Ω becomes deformed configuration Ω^{φ} (="$\varphi(\Omega)$"), and $\mathbf{y} \in \Omega^{\varphi}$ is the material point at time t. The transformation φ maps any point $\mathbf{y}$ in the deformed configuration Ω^{φ} to the corresponding point $\mathbf{x}$ in the reference configuration Ω at time t, i.e. $\mathbf{y} = \varphi(\mathbf{x})$; $\forall \mathbf{x} \in \Omega$ [2]. In Euclidean space, the displacement field is defined as:

$$\mathbf{u(x)} = \mathbf{y} - \mathbf{x} = \varphi(\mathbf{x}) - \mathbf{x}. \tag{1.6}$$

From the deformation computed by image registration, the deformation gradient tensor can be calculated as the partial differentiations:

$$\mathbf{F} = \begin{pmatrix} \frac{\partial \varphi_1}{\partial x_1} & \frac{\partial \varphi_1}{\partial x_2} & \frac{\partial \varphi_1}{\partial x_3} \\ \frac{\partial \varphi_2}{\partial x_1} & \frac{\partial \varphi_2}{\partial x_2} & \frac{\partial \varphi_2}{\partial x_3} \\ \frac{\partial \varphi_3}{\partial x_1} & \frac{\partial \varphi_3}{\partial x_2} & \frac{\partial \varphi_3}{\partial x_3} \end{pmatrix}. \tag{1.7}$$

Then the deformation gradient tensors $\mathbf{F}$ can be used to estimate the transformation-based lung ventilation, regional stretch and strain, and regional anisotropy.

1.6.1 Lung ventilation

Jacobian as an estimate of volume ratio:

As illustrated in Figure 1.8, if we consider the edges of an infinitesimal volume in the reference configuration are parallel to the Cartesian axes [2], then we can define the initial material volume as:

$$dv = dx_1 dx_2 dx_3. \tag{1.8}$$

Based on the elemental vectors in the deformed configuration,

$$\begin{aligned} d\mathbf{y}_1 &= \mathbf{F}d\mathbf{x}_1 = \frac{\partial \varphi_1}{\partial x_1}dx_1 \\ d\mathbf{y}_2 &= \mathbf{F}d\mathbf{x}_2 = \frac{\partial \varphi_2}{\partial x_2}dx_2 \\ d\mathbf{y}_3 &= \mathbf{F}d\mathbf{x}_3 = \frac{\partial \varphi_3}{\partial x_3}dx_3, \end{aligned} \tag{1.9}$$

we can calculate the corresponding material volume after deformation, dV, as:

$$dV = d\mathbf{y}_1 \cdot (d\mathbf{y}_2 \times d\mathbf{y}_3) = \frac{\partial \varphi_1}{\partial x_1} \cdot (\frac{\partial \varphi_2}{\partial x_2} \times \frac{\partial \varphi_3}{\partial x_3})dx_1dx_2dx_3 = Jdv, \tag{1.10}$$

where Jacobian J is the determinant of deformation gradient tensor $\mathbf{F}$,

$$J(\varphi(\mathbf{x})) = \det(\mathbf{F}) = \begin{vmatrix} \frac{\partial \varphi_1}{\partial x_1} & \frac{\partial \varphi_1}{\partial x_2} & \frac{\partial \varphi_1}{\partial x_3} \\ \frac{\partial \varphi_2}{\partial x_1} & \frac{\partial \varphi_2}{\partial x_2} & \frac{\partial \varphi_2}{\partial x_3} \\ \frac{\partial \varphi_3}{\partial x_1} & \frac{\partial \varphi_3}{\partial x_2} & \frac{\partial \varphi_3}{\partial x_3} \end{vmatrix}. \tag{1.11}$$

Therefore, the Jacobian calculated from image registration gives an estimate of local volume ratio $\frac{dV}{dv}$.

Intensity-based ventilation:

In contrast to the transformation-based Jacobian, which is directly computed from the deformation field from image registration, the lung ventilation can also be calculated by involving the intensity information of the registered CT images and the deformation field. Regional ventilation is defined as local air volume change per unit time. One commonly used measure of regional ventilation is the specific ventilation sV, which divides the air volume change by the initial air volume [12]. Specific ventilation sV was introduced when registration-based ventilation measure was validated with the ventilation calculated from Xe-CT [11]. The inverse of the time constant τ, which is calculated from the density changes in multiple Xe-CT wash-in and wash-out phases, is equivalent to specific ventilation sV per unit time.

We assume I_1 and I_2 are two CT images in registration, $\mathbf{x} = (x_1, x_2, x_3)^T$ is a voxel defined in I_1 coordinate, and $\mathbf{h}(\mathbf{x})$ is the corresponding point in I_2 image computed by transformation $\mathbf{h}$. Suppose region volumes are ν_1 and ν_2, and they are composed of tissue volume (V_1 and V_2) and air volume (V_1' and V_2') [12], then,

$$sV = \frac{V_1'(\mathbf{h}(\mathbf{x})) - V_2'(\mathbf{x})}{V_2'(\mathbf{x})}. \tag{1.12}$$

With deformation field and CT intensities, there are three different approaches for estimating the specific ventilation sV in Equation 1.12 [83].

- sV by specific volume change (SAJ), is based on the assumption that there is no tissue volume, i.e. the region volume is pure air volume, making $\nu_1 = V_1'$ and $\nu_2 = V_2'$. SAJ was used as an index of regional ventilation and compared to Xe-CT estimates of regional ventilation (average $r^2 = 0.73$) [11].

$$\text{SAJ} = \frac{\nu_1(\mathbf{h}(\mathbf{x})) - \nu_2(\mathbf{x})}{\nu_2(\mathbf{x})} = J(\mathbf{x}) - 1. \tag{1.13}$$

- sV by corrected Jacobian (SACJ), assumes both existence of tissue volume and air volume. SAJ is a special case of SACJ when tissue volume is assumed to be 0.

$$\text{SACJ} \quad = \quad J(\mathbf{x})\frac{I_1(\mathbf{h}(\mathbf{x}))}{I_2(\mathbf{x})} - 1. \tag{1.14}$$

- sV by intensity change (SAI, equivalent to SAC in Chapter 3), is derived from SACJ with assumption that tissue volume is preserved during deformation, i.e. regional volume change is only due to the air volume change [83]. This metric

has been commonly used by Simon [12], Guerrero et al. [13], and Fuld et al. [49].

$$\text{SAI} = 1000\frac{I_1(\mathbf{h}(\mathbf{x})) - I_2(\mathbf{x})}{I_2(\mathbf{x})(I_1(\mathbf{h}(\mathbf{x})) + 1000)} \tag{1.15}$$

1.6.2 lung mechanics

In addition to regional volume change, deformation field can also be used to estimate regional lung mechanics. Deformation of the lung is more than just volume change. Volume change may be related to regional stretch and strain, and may have oriental preference anisotropy in deformation. For example, the regions near the diaphragm are more likely to deform in the superior-inferior direction than other directions. Therefore, understanding lung mechanics properties can help better characterize the lung tissue deformation.

Regional stretch and strain:

The deformation gradient tensor $\mathbf{F}$ in Equation 1.7 can be decomposed into stretch and rotation components [2]:

$$\mathbf{F} = \mathbf{RU}, \tag{1.16}$$

where the $\mathbf{U}$ is the right stretch tensor and $\mathbf{R}$ is an orthogonal rotation tensor.

The Cauchy-Green deformation tensor is defined as

$$\mathbf{C} = \mathbf{F}^T\mathbf{F} = \mathbf{U}^T\mathbf{R}^T\mathbf{RU} = \mathbf{U}^T\mathbf{U}. \tag{1.17}$$

Principal analysis of $\mathbf{C}$ derives eigenvectors N_1, N_2 and N_3 and their corresponding eigenvalues λ_1^2, λ_2^2 and λ_3^2. We can get λ_1, λ_2 and λ_3 (ordered as $\lambda_1 > \lambda_2 > \lambda_3$) of $\mathbf{U}$ after eigendecomposition [2].

Strain measures how much a given displacement differs locally from a rigid body displacement [1, 2]. Other than linear strain tensor, Lagrangian finite strain tensor, also called the Green-Lagrangian strain tensor or Green-St. Venant strain tensor, is used for large deformations with consideration of rotation in the deformation. Green-Lagrangian strain tensor is defined as:

$$\mathbf{G} = \frac{1}{2}(\mathbf{C} - \mathbf{I}) = \frac{1}{2}(\mathbf{F}^T\mathbf{F} - \mathbf{I}). \tag{1.18}$$

Regional anisotropy:

In a deformation, a region may have no volume change but have changes in its shape. Anisotropy measurement considers orientational preference of deformation. Amelon et al. [84] proposed an anisotropic deformation index (ADI) and slab-rod index (SRI) to describe the relationships among the stretches with relevance to lung expansion. ADI measures the ratio of the length in the maximal extension direction and the length in the minimal extension direction. SRI captures another nature of anisotropy that whether the volume change is predominant along one or two directions. ADI and SRI are defined by

$$\text{ADI} = \sqrt{\left(\frac{\lambda_1 - \lambda_2}{\lambda_2}\right)^2 + \left(\frac{\lambda_2 - \lambda_3}{\lambda_3}\right)^2}, \tag{1.19}$$

and

$$\text{SRI} = \frac{\tan^{-1}\left(\frac{\lambda_3(\lambda_1 - \lambda_2)}{\lambda_2(\lambda_2 - \lambda_3)}\right)}{\pi/2}. \tag{1.20}$$

1.7 Accuracy and reproducibility

Lung ventilation estimation using 4DCT and image registration has become a new and exciting method. Before this method can be trusted for clinical applications,

it needs to be carefully validated to be both accurate and reproducible. Accuracy is the degree of closeness of measurements to the true value of the measured quantity. Reproducibility, also called precision or repeatability, is the degree to which repeated measurements show the same results under unchanged conditions [85]. As analogized to shotting at a target in Figure 1.9, accuracy describes the closeness of arrows to the target center, while reproducibility is the size of the arrow cluster, and high reproducibility means one can expect repeated measurements under the same conditions.

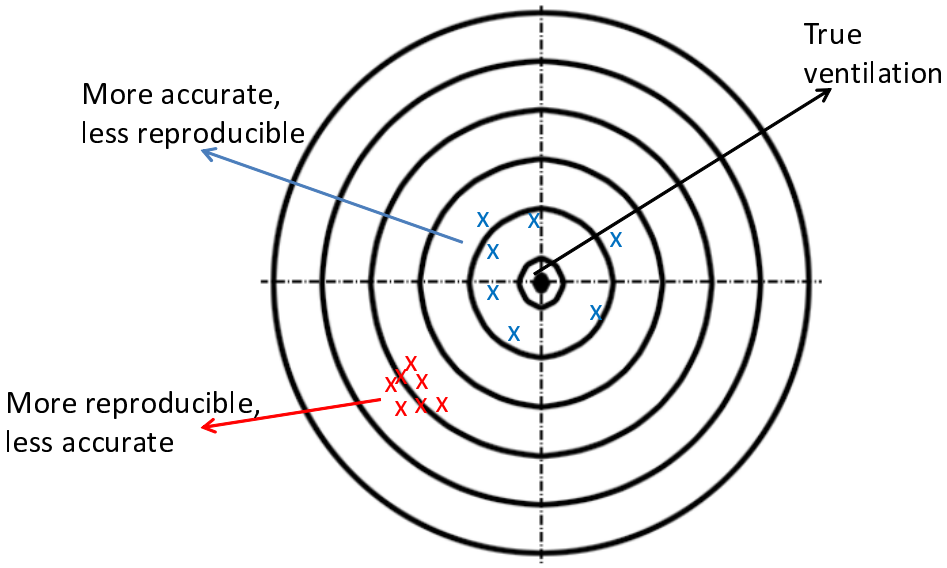

Figure 1.9. Analogy to explain the difference between accuracy and reproducibility using target comparison.

With regard to the 4DCT- and registration-based ventilation measurement, evaluation of accuracy has been performed by comparing it to ventilation measure-

ments from other imaging modalities, such as Xenon CT [11], SPECT perfusion [14], and hyperpolarized ^{3}He MRI [51]. While high correlation was found when compared to Xenon CT ($r^2 = 0.73$) using linear regression analysis, the Dice similarity coefficient used in the comparisons to SPECT perfusion and hyperpolarized MRI made weak qualitative comparison by comparing cover overlays and greatly limited the utility of the cross-modality accuracy validation.

Reproducibility needs to be established when 4DCT- and registration-based ventilation measures are used to identify the radiation induced pulmonary function changes across different 4DCT scans. Uncertainty in pulmonary function measurement can be caused by many factors including subject's irregular breathing patterns and change of tidal volume in spontaneous respiration, imaging protocol, image registration, and choice of ventilation metric [86, 87, 88]. The effectiveness of pulmonary function measures increases as the uncertainty in the measurement is reduced. If we analyze a pair of 4DCT images obtained prior to RT using the same technology, they should ideally yield identical pulmonary function maps. Variations in this measure will have an impact when being used as either input information into the radiation therapy treatment planning process, or for longitudinal study of pulmonary function (e.g., following RT). Du et al. investigated the reproducibility of transformation-based [87] (correlation coefficient 0.81±0.10) and intensity-based [88] (correlation coefficient 0.45±0.14) measures of lung tissue expansion in two repeat prior-RT 4DCT acquisitions. Similarly, Yamamoto et al. [86] investigated the reproducibility of lung ventilation over two different time frames and reported moderate voxel-based corre-

lation between two ventilation images (Spearman rank correlation 0.50±0.15).

1.8 Assess Radiation-induced Pulmonary Change

Regional pulmonary function assessment using 4DCT and image registration is an exciting method that has been developed recently. Since 4DCT has become a routine examination for lung cancer RT treatment planning, this approach could generate high resolution ventilation maps without adding extra radiation dose to the patients. With image registration between CT images reconstructed at certain phases of the breathing cycle, the generated deformation field can be used to compute regional pulmonary function. Several groups have contributed to this approach from the different aspects. Reinhardt et al. [11] directly calculated the determinant of the deformation gradient tensor and used the Jacobian metric to analyze regional ventilation. Simon [12] and Guerrero et al. [13] proposed a density-based ventilation calculation with the deformation field and its relationship with air fraction change. Castillo et al. [14] demonstrated analytic and geometric Jacobian are mathematically equivalent, and both Jacobian-based and density-based ventilation are highly correlated with clinically acquired SPECT ventilation. Recently Yamamoto et al. [86] investigated the reproducibility of 4DCT ventilation for two cohorts of subjects (imaging interval of 15 days and 5 minutes) and found that it was only moderately reproducible. They also reported that respiratory variation during 4DCT scans may deteriorate the reproducibility. Several groups have investigated regional pulmonary function change throughout RT using 4DCT and registration. Ding et al. [15] compared regional ventilation before and after RT. Yaremko et al. [7] and Yamamoto et al. [89] identified

high ventilated lung regions as avoidance structures in intensity modulated radiation therapy (IMRT) planning. Zhong et al. [90] presented a 4DCT-based regional compliance method for evaluation of radiation-induced lung damage. Vinogradskiy et al. [91] used ventilation maps calculated from weekly 4DCT data to study ventilation change throughout radiation therapy, but no consistent pattern of ventilation damage was reported to correlate with the radiation dose.

1.9 Organization of the Thesis

The thesis is broken up into 5 chapters. While the current chapter introduces the background and significance of this study with literature reviews, we organize the rest of thesis as:

- Chapter 2 examines the reproducibility of transformation-based measures of lung tissue expansion in two repeat 4DCT acquisitions within a short time interval of mechanically ventilated sheep and free breathing humans. A framework for evaluating reproducibility across scans is presented and the image registration is validated.
- Chapter 3 examines the reproducibility of intensity-based measures of lung tissue expansion and contraction in sheep and human subjects. Intensity-based Jacobian (IJAC) is introduced to make an intensity-based ventilation estimate comparable with transformation-based ventilation estimate. Analytic models are derived to study the impact of noise from CT images on intensity-based ventilation maps. Additional gamma index is introduced to assess reproducibility. We also investigates improvement in IJAC reproducibility with increasing

levels of denoising on the CT images in this chapter.

- Chapter 4 presents and compares normalization schemes that correct ventilation images for variations in respiratory effort and assess the reproducibility improvement after effort correction for 24 human subjects that need effort correction. The limits of global normalization are evaluated. Relationship between the improvement of reproducibility and respiratory effort difference is investigated.
- Chapter 5 summarizes the results in Chapter 2, 3, and 4, compares our results to others' work, discusses about potential applications of our results, and presents some philosophical thoughts on this study.
- Chapter 6 summarizes the major contributions in this thesis.
- Chapter 7 proposes some studies that are worth being investigated to in the future research.
- Chapter 8 concludes the thesis.

CHAPTER 2

REPRODUCIBILITY OF TRANSFORMATION-BASED MEASURES OF LUNG VENTILATION

This chapter is based on the following papers:

1. K. Du, J. E. Bayouth, K. Cao, G. E. Christensen, K. Ding, and J. M. Reinhardt: Reproducibility of Registration-Based Measures of Lung Tissue Expansion. Medical Physics, 2012
2. K. Du, K. Ding, K. Cao, J. E. Bayouth, G. E. Christensen and J. M. Reinhardt: Registration-Based Measurement of Regional Expiration Volume Ratio Using Dynamic 4DCT Imaging. IEEE International Symposium on Biomedical Imaging (ISBI), 2011

2.1 Introduction

The primary function of the respiratory system is gas exchange. Gas exchange depends on the complex mechanical inter-relationships between the lung tissue, diaphragm, chest wall, and ribs, the fluid dynamics behavior of the nose, mouth, and airways, and the gas diffusion properties of the alveoli. Since many diseases and injury conditions can affect these physical parameters, and thus, lung function, it is useful to be able to reliably measure indices of lung function at the global and regional level.

Global lung function can be assessed using spirometry. Spirometric indices such as forced expiratory volume in one second (FEV1) and forced vital capacity (FVC) are common indices of global respiratory system function. Regional pulmonary

function is more difficult to measure. Invasive methods, such as percutaneously or surgically implanted parenchyma markers or inhaled fluorescent microspheres, are effective but not suited for translation to humans [32, 33, 34]. Noninvasive methods include medical imaging approaches. Positron emission tomography (PET) and single photon emission computed tomography (SPECT) can provide a direct assessment of lung function [35, 36, 37, 38], but their application is limited by low spatial resolution. Hyperpolarized noble gas MR imaging (such as ^{129}Xe and ^{3}He) has been developed for functional imaging of pulmonary ventilation [39, 40, 41, 42, 43]. Hyperpolarized MRI can provide enough temporal resolution to observe the dynamics of gas flow through the lung. However, the method is only partially quantitative and depicts very little anatomic detail. Xenon-enhanced CT is another imaging modality that can directly assess pulmonary ventilation by observing wash-in and wash-out rate of serial CT images [44, 45, 46]. The need for very high temporal resolution to measure the wash-in/wash-out time constants limits the overall axial coverage to about 12 to 15 cm for this modality.

Respiratory-gated CT imaging and 3D image registration can be used to locally estimate lung tissue expansion and contraction (regional lung volume change) to obtain a ventilation map for the lung [11, 14]. Reinhardt et al. [11] compared registration-based estimation of regional lung function using the Jacobian to xenon-CT estimates of specific ventilation and reported average $r^2 \approx 0.73$. Castillo et al. [14] used image registration to compute both transformation-based and intensity-based of local lung function and compared these measures to SPECT functional measures.

Their results demonstrate the equivalence of the analytic and geometric Jacobian for quantifying volume change, and show both methods correlate well with global measurements and clinical SPECT. Recently Yaremko et al. [7] proposed a method incorporating image registration with 4DCT images to identify regions of highly functional lung for avoidance in intensity modulated radiation therapy (IMRT) planning in non-small-cell lung cancer. Ding et al. [15] quantitatively measured the regional changes in lung tissue function following a course of radiation therapy by using 4DCT and image registration techniques. Keall et al. [89] also quantified the dosimetric impact of 4DCT and registration-derived ventilation maps on functional treatment planning to avoid highly-functioning lung regions during radiation therapy. Vinogradskiy et al. [91] used ventilation maps calculated from weekly 4DCT data to study ventilation change throughout radiation therapy.

Along with the increased interest in registration-based estimates of lung function come questions about reproducibility and robustness of the overall approach. Nyeng et al. [92] imaged five patients repeatedly with thoracic 4DCT scans, one scan with respiration restricted by an abdominal compression plate and the other under free breathing, but the reproducibility of the ventilation measurement was not investigated. Before registration-based techniques can be trusted to provide clinically-meaningful measures of lung function or to track RT-induced changes in lung function over time, it is necessary to establish the uncertainty associated with such measurements.

A number of factors influence registration-based estimates of lung function.

Assuming that two volumes are registered to obtain a Jacobian map of lung volume change, these individual volumes may be acquired with the subject apneic or may be selected from a 4DCT series. In the former case, the specific lung volumes at which the inspiratory and expiratory scans are acquired will directly affect the magnitude of the Jacobian values calculated from the image registration. In the latter case, the tidal volume and reproducibility of the tidal breathing during acquisition may influence the Jacobian calculation and overall consistency as data from several breaths are assembled into a single 4DCT volume. Choice of registration algorithm, associated image pre-processing, and regularization strategy will impact the registration accuracy and smoothness of the deformation field [93, 89]. These factors will affect both the fidelity and noisiness of the resulting Jacobian maps.

If we consider the reproducibility of registration-based measures of lung function, subject-related factors become important. Even with pre-scan training and sophisticated pacing strategies, consistent and reproducible respiratory patterns may be difficult to maintain, as the subject must control breathing rate, tidal volume, and the interplay between thoracic vs. abdominal breathing. In the case of static image acquisitions (e.g., near TLC (total lung capacity) and FRC (functional residual capacity)), the ability of the subject to reach the same volumes each time will directly influence the registration-based Jacobians, and thus, the estimates of local lung function [15]. While the image processing and image registration factors also exist when considering reproducibility across two or more studies, it seems likely that subject variability is the major factor that determines overall measurement reproducibility.

However, because it is difficult to separate the effects of subject variability, image acquisition differences, algorithm factors, and other uncertainties, in this chapter we look at the combined effect of all of these factors as a starting point to establish the reproducibility of lung tissue expansion measurements in repeated 4DCT acquisitions of the same subject.

Two different groups are studied in this chapter: (1) spontaneously-breathing human subjects; and (2) anesthetized and mechanically ventilated sheep. In both cases two sets of image data are gathered for each group by scanning twice using 4DCT with a short time interval in-between acquisitions. From each 4DCT data set one volume near end expiration and one volume near end inspiration are reconstructed. These volumes are registered using a B-spline deformable registration technique (described in Section 2.2.3.2) and the Jacobian of the registration deformation field is calculated. The Jacobians computed using the two separate 4DCT acquisition are compared to assess reproducibility.

2.2 Material and methods

2.2.1 Method Overview

Figure 2.1 shows a block diagram of the entire process. Two 4DCT scans (denoted as scan one and scan two) are acquired for each subject with a short time interval between acquisitions. This so-called "coffee break" acquisition is intended to capture two separate images of the lung depicting the same anatomy and physiological condition. For each 4DCT scan, two volumes are selected and reconstructed: an image near full inspiration (denoted as EI) and an image near end exhalation (denoted as

EE). Three-dimensional B-spline deformable image registration is used to deform the EI image to the EE image, producing a registration deformation field. The Jacobian of this deformation field is computed and used to characterize the local lung tissue volume change. This process is performed for both the scan one and scan two data, producing registration transformations T1 and T2 and Jacobian images JAC_{T1} and JAC_{T2}.

Figure 2.1 and Table 2.1 describe the three registration transformations used in this study. The coordinate system of scan one EE is used as the reference coordinate system for all comparisons. Transformation T0 is used to convert the Jacobian maps into a common coordinate system for comparison. The ratio map JAC_{RATIO} is the voxel-by-voxel ratio of the scan one Jacobian and scan two Jacobian. JAC_{RATIO} is computed in the scan one EE coordinate system. The ratio map JAC_{RATIO} is analyzed to assess reproducibility.

2.2.2 Image Data Sets

2.2.2.1 Animal Subjects

Appropriate animal ethics approval was obtained for these protocols from the University of Iowa Animal Care and Use Committee and the study adhered to NIH guidelines for animal experimentation. Data from three adult male sheep (denoted as S-1, S-2, and S-3), with weights 44.0, 37.8, and 40.4 kg, was collected. The sheep were anesthetized using intravenous pentobarbital and pancuronium to ensure adequate sedation and to prevent spontaneous breathing. Animals were positive pressure ventilated during experiments using a custom built dual Harvard apparatus

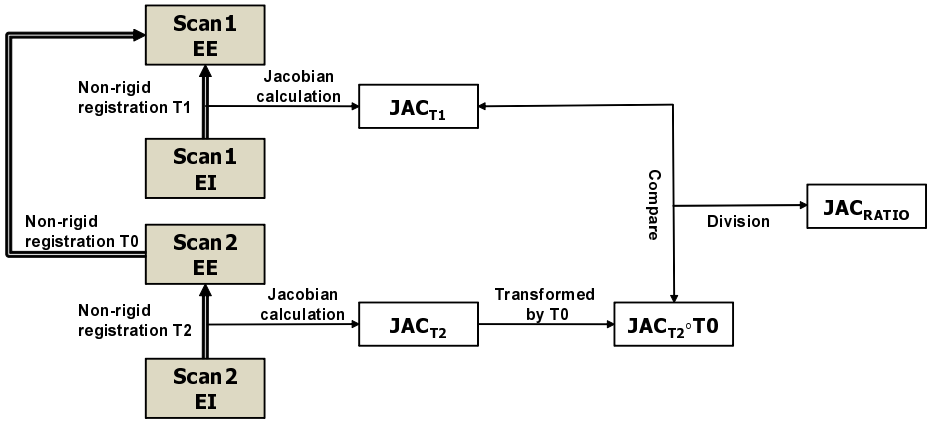

Figure 2.1. Block diagram shows the processing dataflow for the entire process. Scan one EE and scan two EE are volumes at end expiration and scan one EI and scan two EI are volumes at end inspiration. The Jacobians JAC_{T1} and JAC_{T2} are calculated from the registration displacement fields. The ratio image JAC_{RATIO}, computed in the scan one EE coordinate system, is used to assess Jacobian reproducibility.

Table 2.1. Summary of the image registrations performed to calculate lung function.

Transformation Name	Image Transformed	Transformation Is Used To
T0	scan two EE $\rightarrow$ scan one EE	Transform the scan two Jacobian into the scan one EE coordinate system for comparison, producing $JAC_{T2} \circ T0$
T1	scan one EI $\rightarrow$ scan one EE	Calculate scan one lung expansion map JAC_{T1}
T2	scan two EI $\rightarrow$ scan two EE	Calculate scan two lung expansion map JAC_{T2}

Refer to Figure 2.1 for names of the images and the transformations.

piston ventilator designed for computer control. Respiratory rate for animals ranged from 15 to 18 breaths per minute. Two 4DCT images were acquired for each animal with a short (less than 10 minutes) time interval in between scans. The animals were not moved between scans. Images were acquired in the prone position using the dynamic imaging protocol with a pitch of 0.1, slice collimation of 0.6 mm, rotation time of 0.5 sec, slice thickness of 0.75 mm, slice increment of 0.5 mm, 120 kV, and 400 mAs. The airway pressure signal was simultaneously recorded with the X-ray projections and images were reconstructed retrospectively using the B30f kernel to produce a full inspiration image (EI) and end exhalation image (EE).

2.2.2.2 Human Subjects

All data from human subjects was gathered under a protocol approved by the University of Iowa Institutional Review Board. The human data consists of 4DCT data from nine human subjects about to undergo radiation therapy for lung cancer. While twelve human subjects (denoted H-1 to H-12) enrolled in the study, two subjects withdrew prior to data acquisition and one subject experienced heavy coughing during the 4DCT scan making his images unusable. The remaining nine subjects included five males and four females, with ages ranging from 31 to 78 years, with an average age of 57±17 (mean ± standard deviation).

Prior to imaging, each subject was trained using a biofeedback system (RESP @ RATE, Intercure Ltd., Lod Israel) to provide guidance for maintaining a constant breathing rate. Musical cues were used to pace respiration during imaging, using a technique developed at our institution which was previously shown to have high

success [94].

Two 4DCT scans are acquired for each subject, with a short time between scans. The subject left the scanner table between scans. Patients were scanned in supine position using a 40-slice CT scanner (Siemens Biograph, Hoffman Estate, IL) operating in helical mode. Imaging parameters were 120 kV, 2.0 mm slice thickness, 0.5 mm slice increment, 1.2 mm collimator, B30F medium smooth kernel reconstruction filter. Acquisition occurred with a pitch of 0.1 and either a tube rotation speed of 500 ms per rotation (requiring each respiratory cycle to not exceed 5 seconds) or 1000 ms per rotation (for respiratory cycles to not exceed 10 seconds). The amplitude of the respiratory motion was monitored using a strain gauge belt with a pressure sensor (Anzai, Tokyo, Japan).

2.2.3 Data processing

2.2.3.1 Pre-processing

After image acquisition and reconstruction, all images were examined for evidence of severe breathing artifacts or other acquisition problems. Such artifacts may disrupt the image registration process and lead to poor registration results and erroneous lung expansion measurements. Although reconstruction artifacts are common in 4DCT [95] and are a source of variability in our analysis, with the exception of subject H-12, the images in this study were examined and found to contain minimal spatial reconstruction artifacts [96]. The reconstruction artifacts may have been reduced by the audio-coaching for patient respiration and by the ability of helical mode image acquisition to allow manual selection of projection data to be used for image

reconstruction at each phase. Subject H-12 had moderate motion artifacts but it was decided to not eliminate this case from analysis.

Prior to image registration, the images of the animal subjects were resampled to size 288 × 288 × 352 with voxel size 1 mm × 1 mm × 1 mm. Images of the human subjects were resampled to the same voxel size but with image size 304 × 304 × 320. The Pulmonary Workstation 2.0 software (VIDA Diagnostics, Inc., Iowa City, IA) was used to identify the lung regions in the CT images. The lung segmentations were manually inspected and modified if necessary. The binary mask obtained from the segmented lung was used to limit the spatial domain of image registration and subsequent lung function analysis. For each case, the lung volume was calculated by counting the number of voxels in the lung region and multiplying by the voxel volume. Tables 2.2 and 2.3 list the lung volumes measured for the subjects in this study.

2.2.3.2 Image Registration

For each subject, the EI image was registered to the EE image using tissue volume preserving nonrigid registration algorithm previously developed by our group [97]. The algorithm uses a cubic B-spline transformation model and multiresolution optimization procedure to minimize the sum of squared tissue volume difference (SSTVD) [63] subject to a Laplacian regularization constraint, as described in equation (2.1).

$$C_{\mathrm{TOTAL}} = C_{\mathrm{SSTVD}} + \rho\, C_{\mathrm{LAP}}, \tag{2.1}$$

where C_{SSTVD} is the SSTVD cost, C_{LAP} is the Laplacian regularization constraint, and ρ is a weighting parameter. The registration algorithm produces a dense voxel-

Table 2.2. Summary of lung volumes for scans 1 and 2 in EE and EI images for three animal subjects.

Subject	Scan	EE (L)	EI (L)	Tidal Vol. (L)
S-1	1	2.79	3.14	0.38
	2	2.87	3.24	0.37
S-2	1	2.50	2.88	0.38
	2	2.62	3.01	0.39
S-3	1	2.80	3.34	0.54
	2	2.93	3.49	0.56

The "Tidal Vol." column shows the volume difference from EE to EI. All volumes are in liters.

Table 2.3. Summary of lung volumes for scans 1 and 2 in EE and EI images for nine human subjects.

Subject	Scan	EE (L)	EI (L)	Tidal Vol. (L)	Before Reg. Median Lmk. Dist. (mm)	TRE $\mu \pm \sigma$ (mm)	Inter-scan Interval
H-1	1	1.24	1.72	0.48	9.30	0.85±0.41	54 minutes
	2	1.26	1.94	0.68	13.0	1.21±0.64	
H-2	1	5.24	5.86	0.62	7.10	0.80±0.50	61 minutes
	2	5.34	5.91	0.57	5.80	1.20±0.80	
H-4	1	2.90	3.39	0.49	10.9	1.32±1.40	20 hours
	2	2.83	3.41	0.58	12.9	1.68±1.65	
H-7	1	5.26	5.72	0.46	3.70	0.72±0.38	33 minutes
	2	5.69	6.37	0.68	4.10	0.97±0.43	
H-8	1	3.02	3.79	0.77	8.30	1.05±0.66	7 days
	2	3.12	4.35	1.23	8.70	1.41±0.97	
H-9	1	3.65	4.50	0.85	7.50	1.29±0.82	35 minutes
	2	3.81	4.33	0.52	5.10	1.25±0.88	
H-10	1	2.09	2.63	0.54	6.60	1.22±0.78	64 minutes
	2	2.14	2.61	0.47	6.60	1.73±1.24	
H-11	1	3.51	4.09	0.58	4.60	1.30±1.05	33 minutes
	2	3.54	4.22	0.67	4.50	1.36±0.93	
H-12	1	3.95	5.11	1.16	14.1	2.01±1.49	29 minutes
	2	3.91	5.14	1.23	13.5	1.66±0.87	

The "Tidal Vol." column shows the volume difference from EE to EI. All volumes are in liters. The "Inter-scan Interval" column gives the approximate time between the scan one and scan two acquisition. The "Before Reg. Median Lmk. Dist." column gives the median distance of landmark points in EE and EI before registration, which gives an indication of the amount of motion within the lung during inhalation. The "TRE" column gives the mean ± standard deviation of the target registration error.

by-voxel displacement field transforming the EI image to the EE image.

The SSTVD term in the cost function, first introduced by Yin et al. [63], provides a lung-specific intensity similarity criterion that can compensate for the expected change in CT intensity as air is inspired or expired during the respiratory process. For a given lung voxel at location $\mathbf{x}$, assumed to be composed of only air and tissue, the tissue volume V($\mathbf{x}$) at voxel coordinate $\mathbf{x}$ can be estimated as

$$V(\mathbf{x}) = v(\mathbf{x})\frac{\mathrm{HU}(\mathbf{x}) - \mathrm{HU}_{\mathrm{air}}}{\mathrm{HU}_{\mathrm{tissue}} - \mathrm{HU}_{\mathrm{air}}}, \tag{2.2}$$

where $v(\mathbf{x})$ is the total volume of voxel $\mathbf{x}$ and $\mathrm{HU}_{\mathrm{air}}$ and $\mathrm{HU}_{\mathrm{tissue}}$ are the CT values of air and tissue. Following [63], we use $\mathrm{HU}_{\mathrm{air}} = -1000$ HU and $\mathrm{HU}_{\mathrm{tissue}} = 55$ HU. In this case, the SSTVD metric can be written as

$$\begin{aligned} C_{\mathrm{SSTVD}} &= \int_{\mathbf{\Omega}} \left[V_2(\mathbf{x}) - V_1(\mathbf{h}(\mathbf{x}))\right]^2 d\mathbf{x} \\ &= \int_{\mathbf{\Omega}} \left[v_2(\mathbf{x})\frac{I_2(\mathbf{x}) + 1000}{1055} - v_1(\mathbf{h}(\mathbf{x}))\frac{I_1(\mathbf{h}(\mathbf{x})) + 1000}{1055}\right]^2 d\mathbf{x} \end{aligned} \tag{2.3}$$

where I_1 and I_2 represent the CT image data from the EI and EE images being registered, Ω denotes the union of the left and right lung regions, and $\mathbf{h}(\mathbf{x}) = (h_1(\mathbf{x}), h_2(\mathbf{x}), h_3(\mathbf{x}))^T$ represents the transformation being estimated.

The Laplacian regularization term enforces a smoothness constraint on the registration displacement fields $\mathbf{u}(\mathbf{x}) = \mathbf{h}(\mathbf{x}) - \mathbf{x}$ where $\mathbf{x} = (x_1, x_2, x_3)^T$. The regularization term is defined as in [98]:

$$C_{\mathrm{LAP}} = \int_{\mathbf{\Omega}} ||\nabla^2 \mathbf{u}(\mathbf{x})||^2 d\mathbf{x}, . \tag{2.4}$$

where $\nabla = \left[\frac{\partial}{\partial x_1}, \frac{\partial}{\partial x_2}, \frac{\partial}{\partial x_3}\right]$ and $\nabla^2 = \nabla \cdot \nabla = \left[\frac{\partial^2}{\partial x_1^2} + \frac{\partial^2}{\partial x_2^2} + \frac{\partial^2}{\partial x_3^2}\right]$. By adjusting the ρ parameter in equation (2.1), one can balance registration intensity matching per-

formance against deformation field smoothness. In this study, $\rho = 0.25$ was found to provide the best tradeoff between registration field smoothness and registration accuracy.

2.2.3.3 Image Registration Accuracy

Anatomic landmarks were used to assess registration accuracy in the T1 and T2 transformations (matching the EI image to the EE image in scans 1 and 2) and the T0 transformation (matching EE scan two to EE in scan one). A semi-automatic landmarking system was employed for landmark selection and establishing correspondence between images [99]. Approximately 100 to 140 vascular bifurcation points were manually identified within the lungs for each human data set. The landmarks were approximately uniformly distributed within the left and right lung. Landmark correspondence was established by visualizing both the EE and EI image simultaneously. Each landmark pair that was manually annotated by the observer was added to a thin-plate-spline to warp the image and predict the location for the next unmatched landmark pair. The thin-plate spline processing greatly increased the efficiency of the landmark annotation. To assess registration accuracy, the landmark positions predicted by the registration algorithm are compared to the actual landmark positions defined by the human expert.

2.2.3.4 Jacobian and Reproducibility

Regional tissue expansion can be estimated from the determinant of the Jacobian matrix (or simply, Jacobian) of the registration deformation field [11]. If we assume that lung expansion (contraction) is due solely to the flow in (out) of air during

respiration, the Jacobian can serve as a surrogate for regional lung function [100]. For a vector-valued registration deformation field $(h_1(x), h_2(x), h_3(x))$ at voxel location x, the Jacobian $J(h(x))$ is given by:

$$J(\mathbf{h}(\mathbf{x})) = \begin{vmatrix} \frac{\partial h_1(\mathbf{x})}{\partial x_1} & \frac{\partial h_2(\mathbf{x})}{\partial x_1} & \frac{\partial h_3(\mathbf{x})}{\partial x_1} \\ \frac{\partial h_1(\mathbf{x})}{\partial x_2} & \frac{\partial h_2(\mathbf{x})}{\partial x_2} & \frac{\partial h_3(\mathbf{x})}{\partial x_2} \\ \frac{\partial h_1(\mathbf{x})}{\partial x_3} & \frac{\partial h_2(\mathbf{x})}{\partial x_3} & \frac{\partial h_3(\mathbf{x})}{\partial x_3} \end{vmatrix}. \tag{2.5}$$

In a Lagrangian reference frame, if the Jacobian is greater than one, there is local tissue expansion; if the Jacobian is less than one, there is local tissue contraction. A Jacobian value equal to one indicates there is no expansion or contraction at that location. Finite differences were used to numerically compute Jacobian. For visualization, the Jacobian map is color-coded and overlaid onto the original CT data.

The Jacobian maps from scan one and scan two are compared to establish the level of reproducibility. The ratio of the Jacobian maps from scan one, $\mathrm{JAC}_{\mathrm{T1}}$, and scan two, $\mathrm{JAC}_{\mathrm{T2}}$, was computed voxel-by-voxel to produce a new map $\mathrm{JAC}_{\mathrm{RATIO}}$. If the two acquisitions and subsequent image processing produced exactly the same lung expansion estimates, $\mathrm{JAC}_{\mathrm{RATIO}}$ would be equal to one everywhere. The mean and standard deviation of $\mathrm{JAC}_{\mathrm{RATIO}}$ was calculated for all subjects.

2.2.3.5 Respiratory Effort Compensation

Respiratory effort differences, which may occur even with training and respiratory time cues during imaging, can cause scan-to-scan variation in tidal volume and the associated pulmonary function measurements. One possible approach to account for these variations is to apply a correction to the calculated Jacobian map. Since the average Jacobian should reflect the global volume change in the lung, the Jacobian

ratio for scans one and two should be approximately equal to the ratio of the EE and EI volume ratios for the two scans. Thus, these volume ratios can be used as a global linear normalization factor to adjust for lung volume differences between scans one and two. We apply this normalization strategy for all human scans in this study.

2.3 Results

2.3.1 Registration Accuracy

Figure 2.2 shows the cumulative histograms of the landmark distances pre- and post- registration for the T0, T1, and T2 transformations. The pre-registration histograms show the landmark distances after rigid registration was applied to align the data sets prior to the non-linear B-spline registration. The post-registration histograms show the landmark distributions after the B-spline registration is applied. Target registration error (TRE) values after registrations T1 and T2 are summarized in Table 2.3.

2.3.2 Reproducibility in Animal

Figure 2.3 shows transverse and coronal views of the original CT image, the Jacobian map calculated from scan one and from scan two, and the Jacobian ratio image for animal S-1. As illustrated in Figure 2.1, the Jacobian image from scan two (JAC_{T2}) is transformed through the T0 transformation to convert it into the coordinate system of scan one, producing $JAC_{T2} \circ T0$. The T0 transformation allows the two Jacobian images to be directly compared, and allows us to compute the voxel-by-voxel ratio image JAC_{RATIO}. The results for animals S-2 and S-3 are similar.

Figure 2.4 shows in the top row 2D kernel density estimates [101] for the

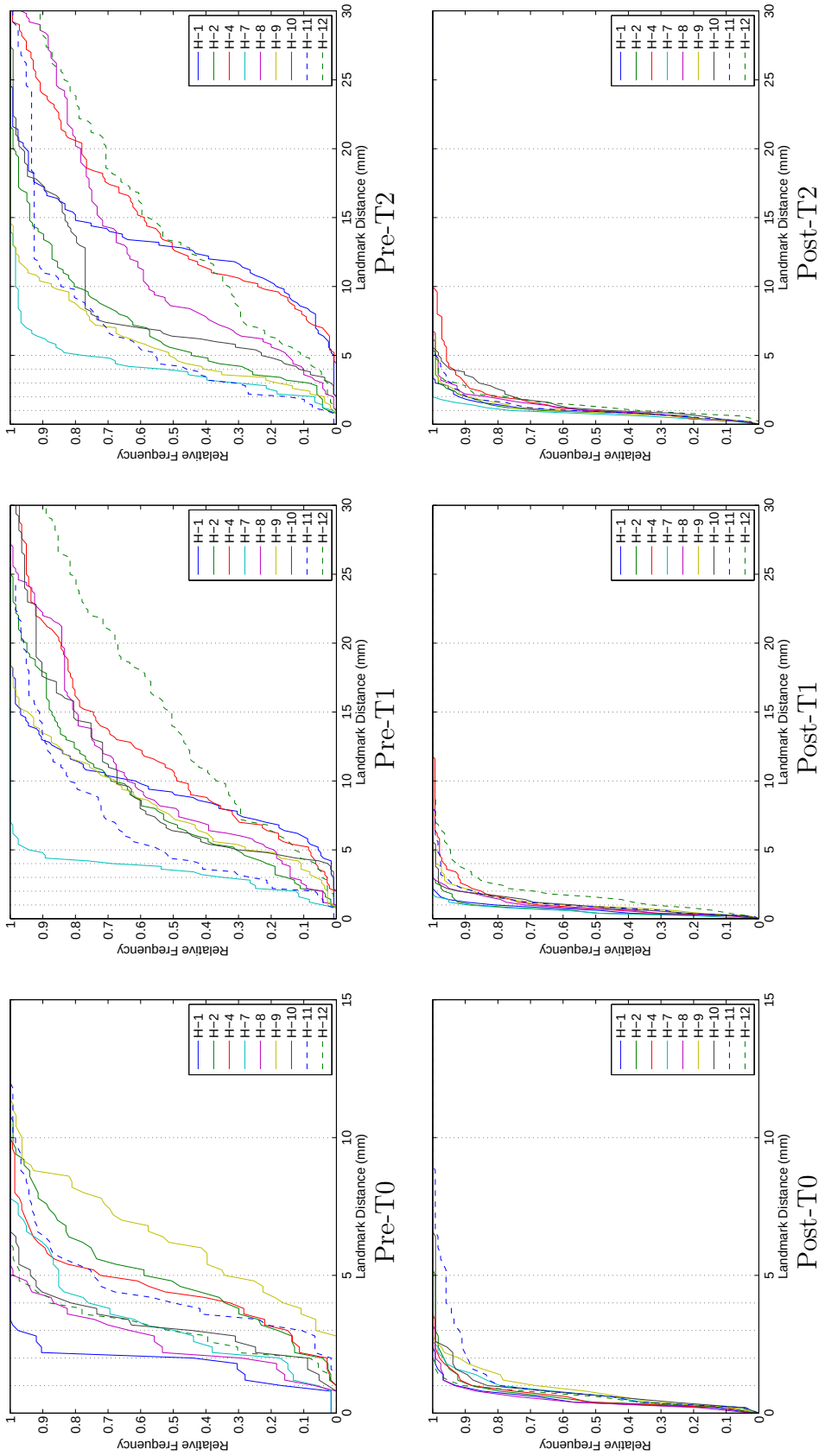

Figure 2.2. Cumulative histograms of the landmark distances pre- and post- image registration for the T0, T1, and T2 transformations.

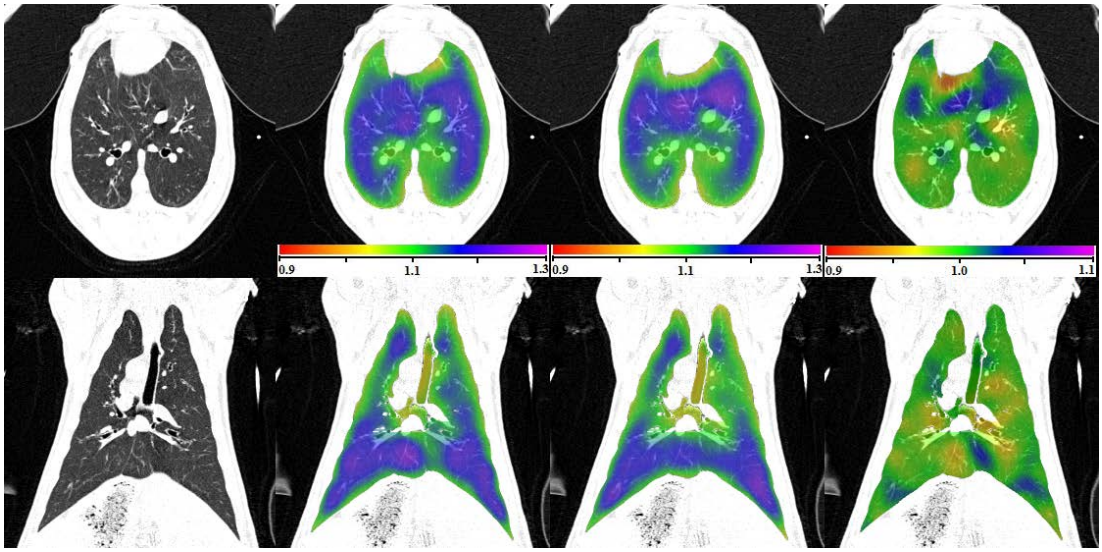

Figure 2.3. Transverse (top) and coronal (bottom) views of (left to right) the original CT, JAC_{T1}, $JAC_{T2} \circ T0$, and JAC_{RATIO} for animal subject S-1. Note the color scales for JAC_{T1} and $JAC_{T2} \circ T0$ are 0.9 to 1.3, and for JAC_{RATIO} the scale is 0.9 to 1.1.

voxel-by-voxel comparison of the scan one and scan two Jacobian data for the three animal subjects. These plots are displayed with a color overlay that shows the joint cumulative distribution of the JAC_{T1} and JAC_{T2} data. Marginal histograms of the JAC_{T1} and JAC_{T2} data are plotted along the top and right side of the figures. A linear regression analysis was performed to find the best fit linear model to represent the relationship between the scan one and scan two Jacobian data. Pearson's correlation coefficient was computed for the linear model, with an average correlation value of 0.88 in the three subjects. The bottom row of Figure 2.4 are modified Bland-Altman plots for the three animals. A Bland-Altman plot is a difference plot for analyzing the agreement between two different assays. The conventional Bland-Altman plot shows the difference of two measurements versus the mean of two measurements. Since the Jacobian represents the ratio of expansion or contraction in local lung volume,

we modified the Bland-Altman plot to show the ratio of JAC_{T1} and $JAC_{T2} \circ T0$ versus the geometric mean of JAC_{T1} and $JAC_{T2} \circ T0$. The modified Bland-Altman plot is overlaid with colors to show a 2D kernel density estimate. Histograms of the JAC_{RATIO} data are plotted along the right side of the figures. The solid line is the reference line where JAC_{RATIO} equals to one , representing perfect agreement in the two measurements. The dashed line is the average of JAC_{RATIO}. The closeness of the dashed line and solid line is one measure of the consistency of our measurement in lung expansion in two scans.

2.3.3 Reproducibility in Human

Figures 2.5 and 2.6 show the transverse and coronal views of the original CT image, the Jacobian map calculated from scan one and from scan two, and the Jacobian ratio image for human subjects H-2 and H-8. As with the animal subjects, the scan two Jacobian image has been transformed into the coordinate system of scan one using the T0 transformation. Subjects H-2 and H-8 were selected to illustrate cases with good and poor reproducibility when comparing the scan one to scan two results. Figure 2.7 shows the 2D kernel density estimate for the voxel-by-voxel comparison of the scan one and scan two and the modified Bland-Altman plot for subject H-2. Figure 2.7(b) shows the mean voxel-by-voxel Jacobian ratio is approximately 0.9922, which is very close to the ideal value of unity.

2.3.4 Respiratory Effort Compensation

Figure 2.8 shows the relationship between the mean Jacobian ratio and the ratio of EI to EE volumes for scan two to the ratio of those volumes in scan one

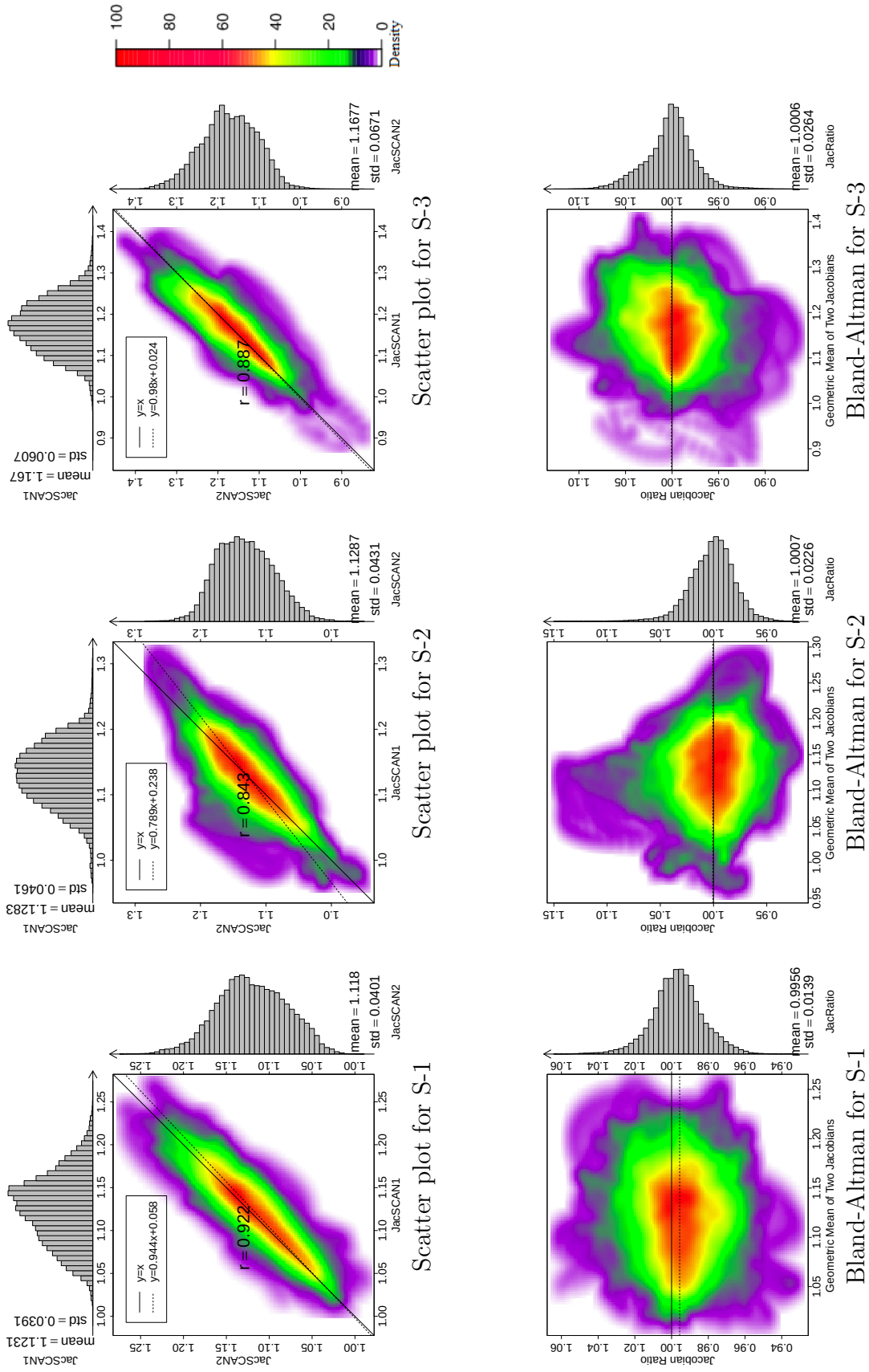

Figure 2.4. The top row shows density scatter plots and marginal histograms of $\mathrm{JAC}_{\mathrm{T1}}$ and $\mathrm{JAC}_{\mathrm{T2}} \circ \mathrm{T0}$ for animals S-1, S-2, and S-3, ordered left to right. The bottom row are modified Bland-Altman plots for the three animal subjects.

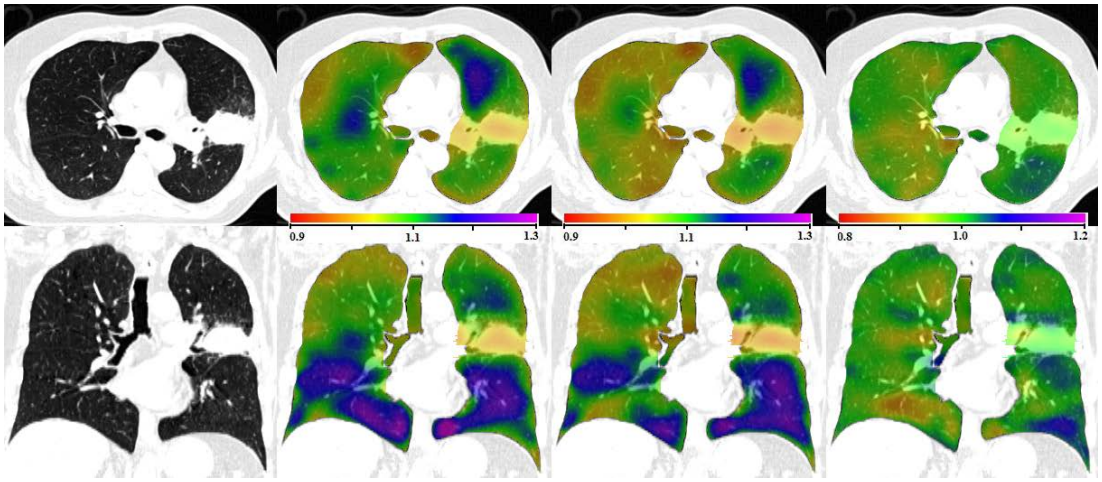

Figure 2.5. Transverse (top) and coronal (bottom) views of (left to right) the original CT, JAC_{T1}, $JAC_{T2} \circ T0$ and JAC_{RATIO} for human subject H-2. Note the color scales for JAC_{T1} and $JAC_{T2} \circ T0$ are 0.9 to 1.3, and for JAC_{RATIO} the scale is 0.8 to 1.2.

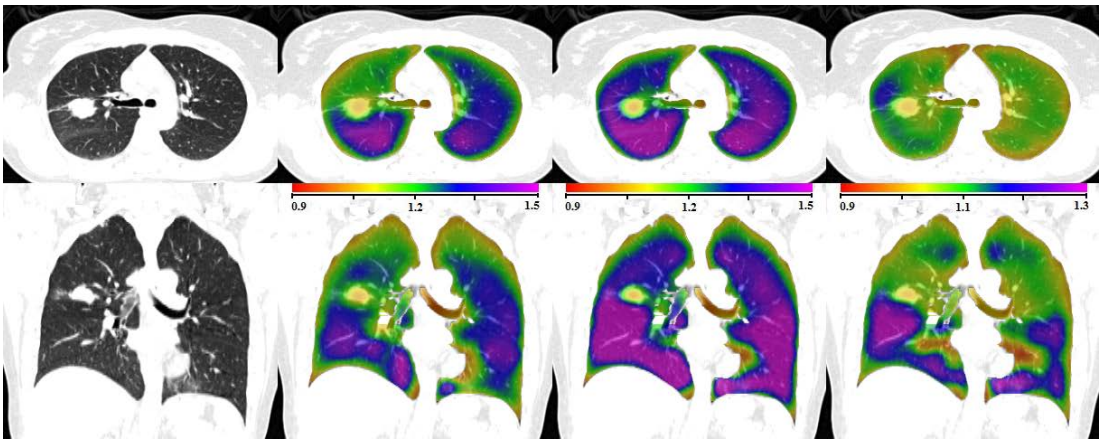

Figure 2.6. Transverse (top) and coronal (bottom) views of (left to right) the original CT, JAC_{T1}, $JAC_{T2} \circ T0$ and JAC_{RATIO} for human subject H-8. Note the color scales for JAC_{T1} and $JAC_{T2} \circ T0$ are 0.9 to 1.5, and for JAC_{RATIO} the scale is 0.9 to 1.3.

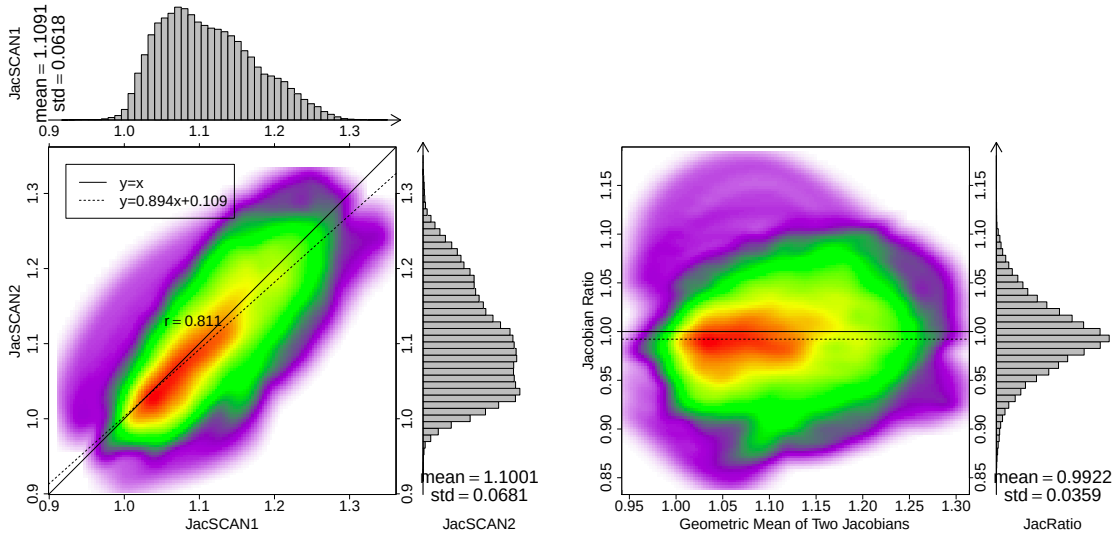

(a) (b)

Figure 2.7. Jacobian scatter plot and Bland-Altman plot for human subject H-2. (a) Smoothed color density scatter plot and marginal histograms of $\mathrm{JAC}_{\mathrm{T1}}$ and $\mathrm{JAC}_{\mathrm{T2}} \circ \mathrm{T0}$ for H-2. Histograms and summary statistics for the $\mathrm{JAC}_{\mathrm{T1}}$ and $\mathrm{JAC}_{\mathrm{T2}}$ data are given along the top and right side of each plot. Colorscale is same as in Figure 2.4. (b) Modified Bland-Altman plot for H-2. The horizontal axis shows $\sqrt{\mathrm{JAC}_{\mathrm{T_1}} * \mathrm{JAC}_{\mathrm{T_2}} \circ \mathrm{T}_0}$ and the vertical axis shows $\mathrm{JAC}_{\mathrm{RATIO}}$.

(the lung volumes are given in Tables 2.2 and 2.3). If the EI to EE ratio changes in scan two from that in scan one, the change indicates an increased or decreased level of effort. Consequently, the Jacobian ratio between scan two and scan one should depict this effort difference as a corresponding increase or decrease in lung expansion. The figure shows that the mean Jacobian ratio is strongly correlated with the EE and EI volume ratios in scans one and two.

From Table 2.3, a global lung expansion factor can be computed by taking the ratio of the end inspiration to end expiration volumes for each of scan one and two. Then a normalization scale factor for the Jacobian of the second scan can be determined by taking the ratio of the lung expansion factor for scan one to the lung

expansion factor for scan two. Taking subject H-8 as an example, the global expansion factors are 1.25 and 1.39 for scans one and two, producing a $JAC_{T2} \circ T0$ multiplicative normalization factor of 0.9. This approach for global linear normalization is applied to all human subjects and results are summarized in Table 2.4.

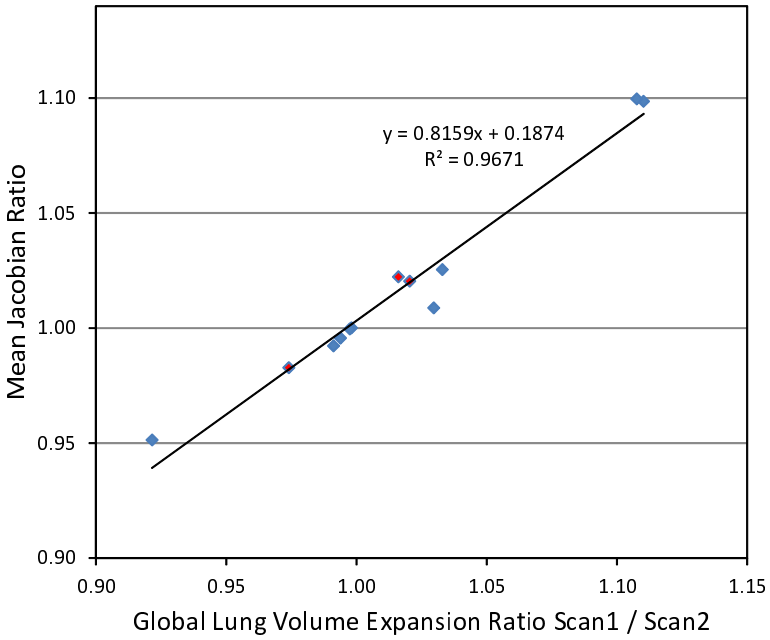

Figure 2.8. Figure shows the mean Jacobian ratio vs. the ratio of global lung volume expansion ratio for scan one to scan two for three animal subjects and nine human subjects. The animal subjects are marked with red diamonds and the human subjects are marked with blue diamonds.

H-8 is an example of a subject that has significant breathing effort differences between the two 4DCT scans. Figure 2.9 shows the Jacobian scatter plot and modified Bland-Altman plot of patient H-8 before and after the Jacobian in scan two is scaled by a constant global normalization factor. This global linear normalization brings the

center of mass of the scatter plot closer to unity, indicating more reproducible measurements. Figure 2.10 shows the results before and after normalization for subject H-4. In this case the global linear normalization produces a mean JAC_{RATIO} that is closer to one and a regression line slope that is closer to one, however the normalization shifts the mode of the Jacobian ratio distribution (red region in density plot) away from unity.

2.3.5 Jacobian Ratio Images

If the subject, image acquisition, and image analysis were perfectly reproducible, the Jacobian values computed from scan one and scan two would match exactly and the Jacobian ratio images would be equal to one everywhere. Figure 2.11 shows box plots of the Jacobian ratio values for the three animal subjects and nine human subjects before and after the global linear normalization. Table 2.4 summarizes and compares the statistical parameters before and after normalization, including the mean, standard deviation (Std), coefficient of variation (CV) of JAC_{RATIO}, the correlation coefficient between JAC_{T1} and $JAC_{T2} \circ T0$, and the slope of regression line.

2.4 Discussion

The results in Figure 2.2 show that the B-spline registration is effective at aligning the user-defined landmarks, with 90% of the landmark distances below 5 mm after registration for eight of the nine human cases. The remaining case, case H-12, was especially difficult for the manual analyst in that it was difficult to precisely locate landmarks and to determine the exact correspondences. Thus, it is likely that

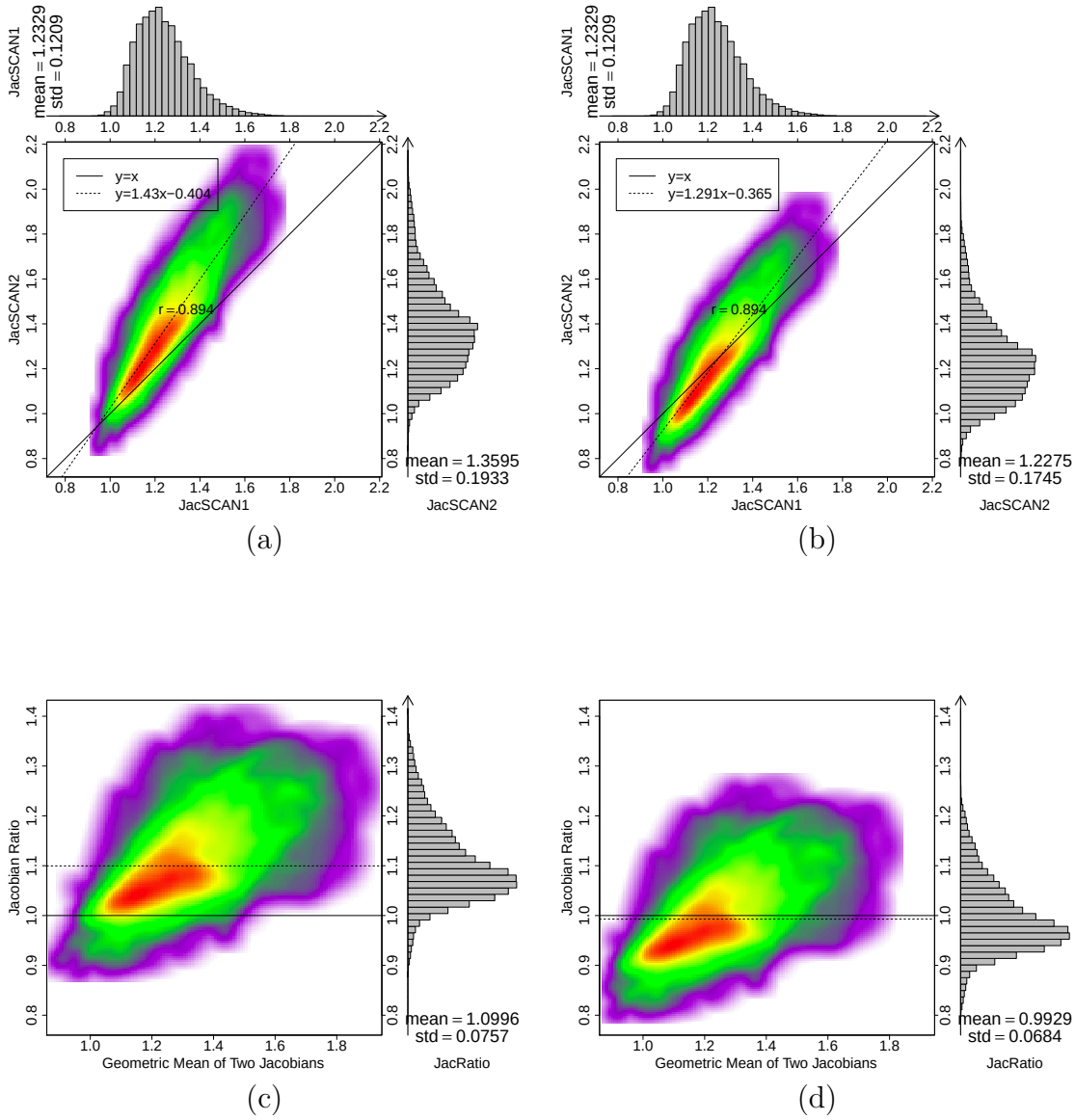

Figure 2.9. Jacobian scatter plot and modified Bland-Altman plot for human subject H-8 before and after global normalization. (a) Scatter plot before global normalization. (b) Scatter plot after global normalization. (c) Bland-Altman plot before global normalization. (d) Bland-Altman plot after global normalization.

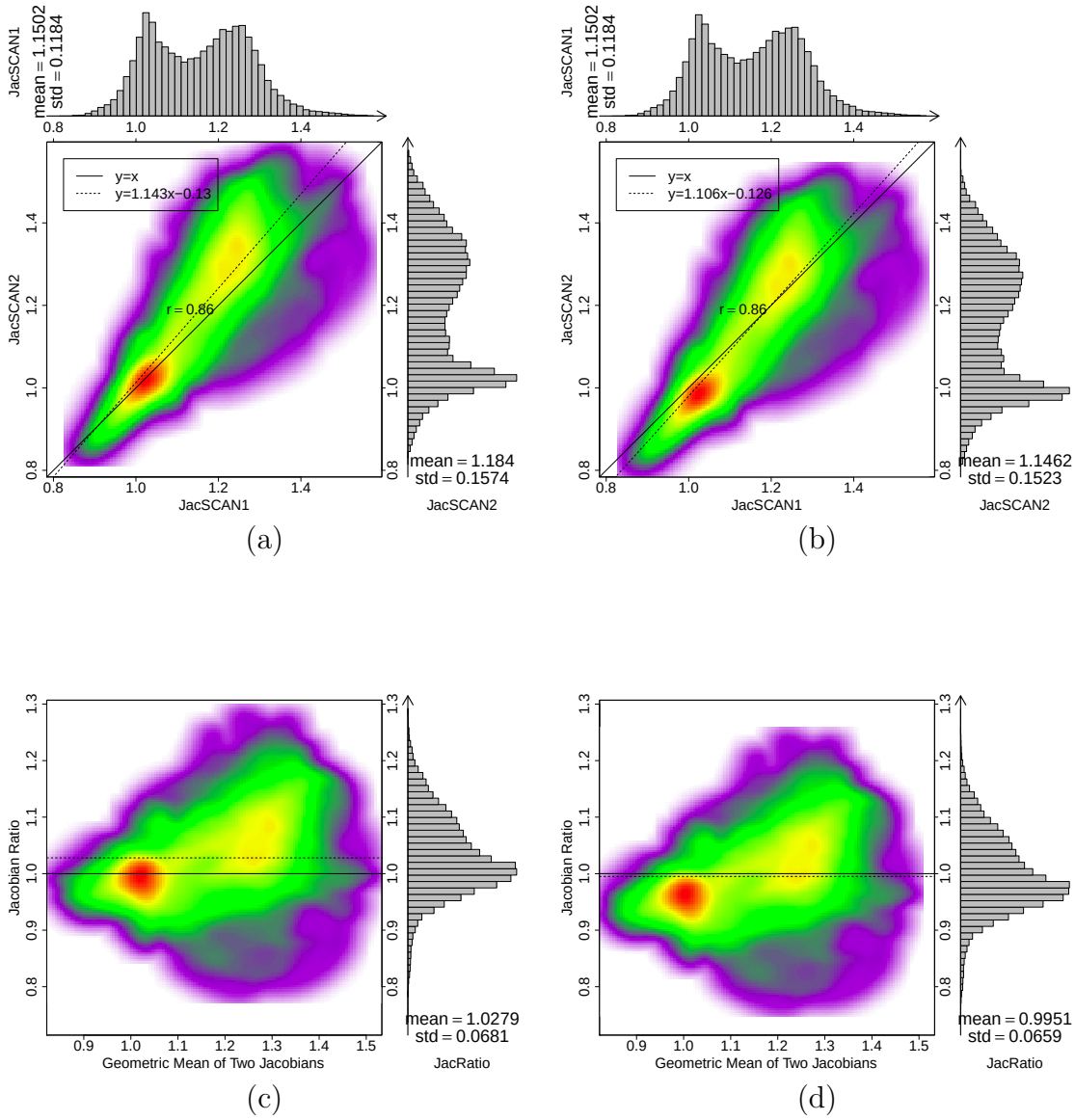

Figure 2.10. Jacobian scatter plot and modified Bland-Altman plot for human subject H-4 before and after global normalization. (a) Scatter plot before global normalization. (b) Scatter plot after global normalization. (c) Bland-Altman plot before global normalization. (d) Bland-Altman plot after global normalization.

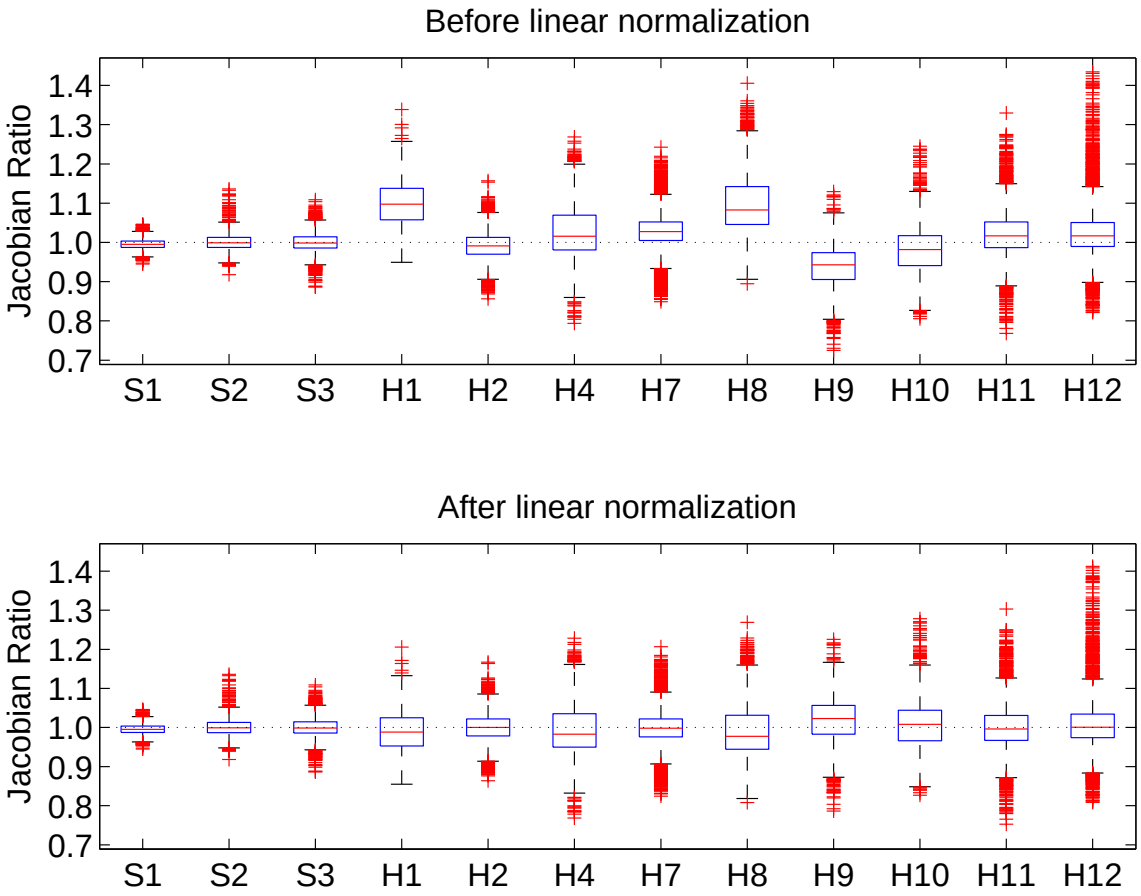

Figure 2.11. Box plots for Jacobian ratio images $\mathrm{JAC}_{\mathrm{RATIO}}$ for three animal subjects and nine human subjects, before and after global linear normalization on human subjects. First and third quartile are shown as the lower and upper extreme, and the whiskers indicate extending beyond the extremes by 1.5 times the range of lower to upper extremes. The outliers are marked with red plus signs. Number of data points has been downsampled by a factor of 1000 for visualization.

Table 2.4. Means, standard deviations, and coefficient of variation (CV) of the Jacobian ratio images, correlation coefficients and regression line slopes of Jacobian images JAC_{T1} and JAC_{T2} for three animal subjects and nine human subjects.

Subject	JacRatio		Norm. JacRatio		C.V.	Corr.	Regression Slope	
	Mean	Std.	Mean	Std.		Coef.	Before Norm.	After Norm.
S-1	0.996	0.0139	-	-	0.0140	0.922	0.944	-
S-2	1.000	0.0226	-	-	0.0226	0.843	0.789	-
S-3	1.000	0.0264	-	-	0.0264	0.887	0.980	-
H-1	1.099	0.0565	0.990	0.0509	0.0514	0.937	1.289	1.161
H-2	0.992	0.0359	1.001	0.0362	0.0362	0.811	0.894	0.902
H-4	1.025	0.0681	0.993	0.0659	0.0664	0.860	1.143	1.106
H-7	1.009	0.0515	0.980	0.0500	0.0511	0.570	0.528	0.513
H-8	1.100	0.0757	0.993	0.0683	0.0688	0.894	1.430	1.291
H-9	0.951	0.0527	1.032	0.0572	0.0554	0.772	0.522	0.566
H-10	0.983	0.0635	1.009	0.0652	0.0646	0.820	0.774	0.795
H-11	1.020	0.0666	1.000	0.0653	0.0653	0.755	0.824	0.808
H-12	1.022	0.0747	1.006	0.0735	0.0731	0.850	0.769	0.757

Columns four, five, and nine show the normalized results for the human subjects. After normalization, the mean and standard deviation of the Jacobian ratio images are scaled accordingly, while the CV stays the same.

some of the residual landmark positioning error after registration for case H-12 (and perhaps others) is due in part to motion artifacts and in part by human error during landmarking. Based on the data in Figure 2.2 and Table 2.3, the mean landmark positioning error is on the order of a few mm, which is similar in performance to earlier work [11, 93, 97, 98]. It is interesting to note that given the landmark results for case H-12 and the comparisons in Figure 2.2, H-12 is not the subject with the worst reproducibility, i.e. for case H-12, the large residual landmark positioning error does not lead to poor reproducibility in the Jacobian maps. This apparent contradiction lends further support to the hypothesis that case H-12 has unreliable manually-defined landmarks.

The pre-T1 graphs in Figure 2.2, the lung volumes in Tables 2.2 and 2.3,

and the median landmark distances before registration in Table 2.3 give some insight into the reproducibility of the subjects in terms of respiratory patterns and level of inspiration. The pre-T1 graphs in Figure 2.2 show the amount of landmark motion within the lung during inhalation, which varied greatly between human subjects. Table 2.3 shows considerable variation in the differences of tidal volumes and median landmark displacements for scans one and two, with no clear relationship between these two measurements.

Figures 2.3 and 2.4 show good reproducibility of the calculated Jacobian maps in the animal model. The Jacobian histograms are very similar in scan one and scan two and the linear regression of the voxel-by-voxel comparison between JAC_{T1} and JAC_{T2} has a slope close to unity. The modified Bland-Altman plot shows that the average Jacobian ratio is approximately equal to one for all three cases. This is not surprising given that the animals were anesthetized and mechanically ventilated during these studies, and were not moved between image acquisitions. As shown in Table 2.2, the EE and EI lung volumes, and thus the tidal volumes, were very reproducible in the animal experiments. From several different perspectives, the reproducibility results in these animal studies probably represent the very best reproducibility measurement that we can expect across repeat studies of this type in humans.

Figures 2.5 and 2.6 show examples of data from human subjects with good and poor reproducibility. Table 2.3 shows that subject H-2 is a case where the lung volumes and tidal volumes were very consistent between scan one and scan two,

while the data for case H-8 shows a considerable change in the EI volume, and thus a change in the overall tidal volume. Interestingly, case H-8 was one in which scan two was acquired one week after scan one, but prior to radiation therapy. It is possible that there were physiological changes during the time between scans, or perhaps the subject simply forgot some of the respiratory training and breathed differently during the second acquisition. If the latter explanation is true, this may have important implications for respiratory monitoring equipment and patient training procedures. Also note the increase of Jacobian is not uniformly distributed within the lung, but reveals highly organized regions of increased ventilation.

Figure 2.7, 2.10, and 2.9 shows the scan one vs. scan two comparison of the Jacobian data for subjects H-2, H-4 and H-8. Comparing the JAC_{T1} and JAC_{T2} histograms and the linear regression line slopes, case H-2 has the best reproducibility. From the Jacobian histograms of H-4, it is interesting to note that subject H-4 has a bimodal Jacobian distribution. The statistical parameters in Table 2.4 might be interpreted with the help of Table 2.3, which shows the EE, EI, and tidal volumes for the scan one and scan two acquisitions. Some of the cases with linear regressions slopes very different from unity, such as cases H-1, H-7, H-8, and H-9, are all cases where there was a big (200 cc or more) change in tidal volume between scan one and scan two. This increase (or decrease) in tidal volume would lead to an increased (or decreased) amount of lung expansion, thus directly affecting the Jacobian values. Therefore, in these cases the subjects' breathing patterns were not reproducible, which in turn caused the lung expansion maps to be not reproducible.

Static breath-hold imaging in place of 4DCT would reduce imaging artifacts induced by variability in breathing patterns, but has some important disadvantages. The most significant disadvantage is the inability of a free-breathing subject to reproducibly reach and hold full inspiration (TLC) in repeat studies, which will undermine the reproducibility of any lung expansion measures derived from breath-hold acquisition [102]. In addition, imaging data acquired with the subject apneic does not elucidate the relationship between tumor position and respiratory phase during tidal breathing, which is needed for gated treatment delivery.

The difficulty of precise breath control in clinical 4DCT creates a need for a compensation or normalization scheme that can be used to account for breathing effort variation in different studies. Since the mean Jacobian is strongly correlated with the lung volume ratios (see Figure 2.8), an obvious and straightforward normalization method is to apply a multiplicative factor to one of the two lung expansion maps. The multiplicative factor can be computed from the EI and EE lung volumes ratios in scans one and two. Since this approach scales the entire expansion map by single constant, this normalization is a global linear normalization. Figure 2.11 shows that the mean $\mathrm{JAC}_{\mathrm{RATIO}}$ is closer to unity after such a normalization. Comparing the scatter plot and modified Bland-Altman plot for H-8 before and after normalization (Figure 2.9), the slope of the regression line is closer to one and the average $\mathrm{JAC}_{\mathrm{RATIO}}$ is closer to one, showing the effectiveness of the effort normalization. However, the effectiveness of global linear normalization for subject H-4 is less clear. Though the regression line and the average of $\mathrm{JAC}_{\mathrm{RATIO}}$ are closer to one after normalization (see

Figure 2.10), the mode of the JAC_{RATIO} distribution is biased away from the desired value of one. From the data given in Table 2.4, six of nine subjects have regression line slopes closer to one after global linear normalization. Note that after normalization the mean and standard deviation of JAC_{RATIO} are also scaled by the normalization factor, while the CV and correlation coefficient are unchanged.

Ideally, a lung volume normalization scheme should account for the fact that the rates of lung expansion and contraction are not uniform apex to base and ventral to dorsal. Because of this, it seems unlikely that a single global normalization constant is the optimal approach to locally compensate for differences in inspiration level between scans.

The boxplot data in Figure 2.11 summarizes the distribution of the JAC_{RATIO} data for three animal subjects and nine human subjects. It is clear from the figure that there is less JAC_{RATIO} variation in the mechanically-ventilated animal subjects than in the spontaneously-breathing human subjects. There are outliers in the JAC_{RATIO} distribution in both the animal and human subjects; some of this might be attributable to the fact that small registration errors in the T0 transformation used to match the JAC_{T1} and JAC_{T2} data may incorrectly align a voxel experiencing high expansion (say normal tissue) with a voxel of low or near zero expansion (such as a blood vessel or airway wall). The resulting Jacobian ratio could be very high, producing an outlier. By reversing the high expansion and low expansion voxels and following a similar reasoning, very low ratio values could also be produced. One solution to this might be to use different methods to compare the Jacobian maps, such

as an approximate method that matches Jacobian values within a neighborhood of voxels.

Several statistical parameters of the JAC_{RATIO} distributions are given in Table 2.4 for all subjects. These parameters may be useful for estimating confidence intervals and performing statistical tests to detect changes in lung expansion between two scans, as might be expected during a longitudinal study tracking a disease process or an intervention such as radiation therapy. By combining the information in Table 2.4 with image analysis techniques that can identify clusters of voxels that exhibit a similar changes in Jacobian value, it may be possible to use the Jacobian map to quantitatively monitor lung function on a very regional level.

2.5 Summary

Local measures of lung function are difficult to obtain with sufficient spatial and temporal resolution. Lung expansion, a surrogate for lung function, can be assessed using two or more respiratory-gated CT image acquisitions. In this study we have examined the reproducibility of such measures using two 4D image acquisitions taken with a short time interval between acquisitions. The results show that good reproducibility can be obtained in anesthetized, mechanically ventilated animals, but variations in respiratory effort and breathing patterns reduce reproducibility in spontaneously-breathing humans. Global linear normalization can globally compensate breathing effort differences, but homogeneous scaling does not account for differences in regional lung expansion rates. Additional work is needed to develop effective compensation procedures or regional normalization schemes that can account

for human variation during respiration.

CHAPTER 3

REPRODUCIBILITY OF INTENSITY-BASED MEASURES OF LUNG VENTILATION

This chapter is based on the following paper:

1. K. Du, J. E. Bayouth, K. Ding, G. E. Christensen, K. Cao, and J. M. Reinhardt: Reproducibility of Intensity-based Measures of Lung Ventilation. Submitted to Medical Physics (in first revision), 2013

3.1 Introduction

Lung function depends on tissue material properties and respiratory system mechanics. Since many disease processes and injury conditions can alter lung function, it is useful to be able to reliably measure indices of lung function at the global and regional level. Regional pulmonary ventilation is the term used to characterize the volume of fresh air per unit time that enters or exits the lung at the acinar (gas exchange) level. Regional pulmonary ventilation can reflect physiological and pathological changes in the airways, parenchymal mechanics, respiratory muscles, body posture effects, and inhaled gas properties. While some characteristics of global lung function can be assessed using spirometry and pulmonary function testing, regional pulmonary ventilation is more difficult to measure.

Noninvasive imaging approaches have been developed to assess regional pulmonary ventilation, such as positron emission tomography (PET) [35, 36, 37], single photon emission computed tomography (SPECT) [103, 104, 105], hyperpolarized no-

ble gas MR imaging [39, 40, 41, 42, 43], and xenon-enhanced CT [44, 45, 46]. Recent advances in multi-detector-row CT (MDCT), 4DCT respiratory gating methods, and image registration algorithms now enable us to obtain a regional lung expansion map for the lung, which in turn can be used as an index of regional lung ventilation [11, 14].

Before the registration-based assessments of regional tissue expansion can be trusted to provide clinically-meaningful measures and be used to track pulmonary function change, for example, during radiation therapy (RT) course [15], it is necessary to understand the variabilities of the techniques and establish technique uncertainty. Several factors can influence these measurements, such as subject motion, respiratory rate, and breathing effort variations, image acquisition artifacts and noise, the image registration algorithm, associated regularization and similarity criteria, and image registration errors. In [87], Du et al. examined the reproducibility of lung expansion measures computed from the Jacobian of the registration displacement field aligning a CT image of the lungs at end inspiration to an image acquired at end expiration. Yamamoto et al. [86] investigated the reproducibility of lung ventilation using a transformation-based volume change metric and 4DCT imaging over two different time frames and reported moderate voxel-based correlation between two ventilation images (Spearman rank correlation 0.50±0.15).

In this chapter, we evaluate the reproducibility of three different techniques for computing regional pulmonary ventilation. All three techniques utilize the same 4DCT as the input data for computations, which have been acquired as repeat scans for a cohort of spontaneously-breathing human subjects and anesthetized and me-

chanically ventilated sheep. The first technique is based on computing the specific air volume change (SAC), which is computed directly from the intensity value (Hounsfield unit) of each voxel within the lung [14]. For the second technique we derive the relationship between the SAC and the local volume change of each voxel, again derived from the CT voxel intensity, which we call the intensity-based Jacobian (IJAC). Finally, we derive the local volume change from transformation field required to register the CT acquired at the end of inspiration with that at the end of expiration, which we call the transformation-based Jacobian (TJAC) [87]. Since SAC and the Jacobian represent different physical phenomena and have different units, they are difficult to compare directly. Therefore, we introduce the IJAC, which measures the same local volume change as the transformation-based Jacobian (TJAC). We propose using reproducibility as the metric to assess which of these approaches provides the most sensitive measure of ventilation change following medical intervention (e.g., radiation therapy), and to quantify the amount of change that can be attributed to the intervention and not from the inherent uncertainty produced by the technique. We also analyze the effects of variation in respiratory effort and the impact of CT noise on the different approaches for computing pulmonary ventilation.

As an extension of our previous work in [87], this chapter continues and expands the analysis on the reproducibility of registration-based estimates of lung ventilation in the following aspects: 1) developing IJAC to make an intensity-based ventilation estimate comparable with transformation-based ventilation estimate, and clarifying the relationship between IJAC and SAC; 2) deriving analytic models to

study the impact of noise from CT images on intensity-based ventilation maps; 3) introducing an additional comparison metric, the gamma index; 4) comparing the reproducibility of the intensity-based ventilation estimates with the transformation-based ventilation estimates presented in [87]; 5) using the same normalization scheme as in [87] on the intensity-based ventilation estimates and studying the reproducibility before and after normalization; and 6) investigating improvement in IJAC reproducibility with increasing levels of denoising on the CT images.

3.2 Background

One approach to estimate regional ventilation is to apply the principles of continuum mechanics on the displacement field produced by a deformable image registration. The Jacobian determinant, or simply the Jacobian, is the determinant of the deformation gradient tensor as shown in Equation 2.5 as presented in Chapter 2, where $\mathbf{h}(\mathbf{x})$ represents registration deformation field [11]. In this chapter, we will refer to the Jacobian calculated using Equation 2.5 as the *transformation-based Jacobian* (TJAC). The Jacobian measures the local volume change in a region, and can include contributions due to both tissue volume change and air volume change. Castillo et al. [14] demonstrated the equivalence of the Jacobian computed using Equation 2.5 and a geometrical approach based on computing the volume change of a 3D polygonal region [106]. Reinhardt et al. [11] compared registration-based estimates of regional lung function using the Jacobian with xenon-CT estimates of specific ventilation and reported average r^2 of 0.73. Ding et al. [15] used the Jacobian to quantitatively measure regional ventilation before and after a course of radiation therapy.

An alternative to the Jacobian-based approach for computing a ventilation map was described by Guerrero et al [13], who characterized regional ventilation in subjects utilizing the relationship between local air fraction and measured CT intensity values, following the approach suggested by Simon [12]. Assuming that a lung region consists only of air and tissue, the air fraction F can be calculated directly from the CT voxel values [107, 108]:

$$F = -\frac{\mathrm{HU}}{1000}, \tag{3.1}$$

where HU represents the mean CT value in the region of interest. Now suppose an image registration algorithm registers two images (called the *fixed* and *moving* images) acquired at different lung volumes. The change in fractional air content, or specific air volume change (SAC), within a region is then [12]:

$$\mathrm{SAC} = \frac{\Delta V}{V_f} = \frac{F_2 - F_1}{F_1(1 - F_2)} \tag{3.2}$$

where ΔV is local volume change in the region, and V_f is the volume of air in the region the fixed image. F_1 is the fraction of air in the region in the fixed image, and F_2 is that fraction in the corresponding region in the moving image. If we assume that local volume change is due only to the increase or decrease of air (flow in or flow out), and assume the intensity of air is -1000 HU and tissue is 0 HU, the specific air volume change (SAC) can be computed from the image intensity values and the image registration transformation $\mathbf{h}(\cdot)$:

$$\mathrm{SAC} = \frac{\Delta V}{V_f} = 1000\frac{I_m(\mathbf{h}(\mathbf{x})) - I_f(\mathbf{x})}{I_f(\mathbf{x})(I_m(\mathbf{h}(\mathbf{x})) + 1000)}, \tag{3.3}$$

where $I_f(\mathbf{x})$ is the CT intensity (HU) at location $\mathbf{x}$ in the fixed CT image and $I_m(\mathbf{h}(\mathbf{x}))$ is the CT intensity of corresponding voxel in the moving CT image [14]. In [14], Equation 3.3 was applied to all lung voxels with a CT intensity between -999 and -250 HU.

Castillo et al. [14] compared the TJAC (computed using Equation 2.5) and intensity-based specific air ventilation (computed using Equation 3.3) with ventilation from ^{99m}Tc-labeled aerosol SPECT/CT, and found higher correlation between intensity-based ventilation and SPECT/CT based ventilation than correlation between transformation-based Jacobian and SPECT/CT based ventilation. Yaremko et al. [7] proposed using the intensity-based ventilation map to identify regions of highly functional lung for avoidance in intensity modulated radiation therapy (IMRT) planning in non-small-cell lung cancer. Vinogradskiy et al. [91] used the intensity-based specific air volume change (Equation 3.3 in this chapter) calculated from weekly 4DCT data to study ventilation change throughout radiation therapy as a function of radiation dose. Recently Ding et al. [83] compared three registration-based ventilation measures, specific air volume change calculated from the Jacobian (SAJ), specific air volume change calculated by the corrected Jacobian (SACJ), and specific air volume change by intensity change (SAI), where SAI can be derived from SACJ by assuming that tissue volume is preserved during deformation. The SACJ was found better correlated with Xe-CT than the other two measures.

3.3 Material and methods

3.3.1 Method Overview

Figure 3.1 shows a block diagram of the entire process. Two 4DCT scans (denoted as scan one and scan two) are acquired for each subject with a short time interval between acquisitions. This so-called "coffee break" acquisition is intended to capture two separate 4DCT image sets of the lung depicting the same anatomy and physiological condition. For each 4DCT scan, two volumes are selected and reconstructed: an image near full inspiration (denoted as EI) and an image near end exhalation (denoted as EE). Three-dimensional B-spline deformable image registration is used to deform the EI image to the EE image, producing a registration deformation field. Following the process in [14], the EE and EI images involved in the registration are smoothed to reduce noise and then the intensity-based ventilation is computed from the displacement field and the aligned CT image pair. An additional spatial averaging of the resulting ventilation map is performed to generate the final ventilation map. This process is performed for both the scan one and scan two data, producing registration transformations T1 and T2 and final intensity-based ventilation images SAC_{T1} and SAC_{T2} or JAC_{T1} and JAC_{T2}.

Other than transformations T1 and T2 defined between the EI and EE respiratory phase points on 4DCT, one additional transformation, T0, mapping scan two EE to scan one EE, is used to convert the ventilation maps into a common coordinate system for comparison. T0 transformation is computed using the same image registration algorithm as that used for T1 and T2. The coordinate system of scan

one EE is used as the reference coordinate system for all comparisons. Because the intensity-based ventilation maps may have zero and missing values [14], the application of a voxel-by-voxel ratio or difference is not appropriate for comparison. In this chapter we use a gamma index metric to compare the two maps with tolerance for differences in ventilation value and location.

3.3.2 Image Data Sets

3.3.2.1 Animal Subjects

Appropriate animal ethics approval was obtained for these protocols from the University of Iowa Animal Care and Use Committee and the study adhered to NIH guidelines for animal experimentation. Data from three adult male sheep, with weights 44.0, 37.8, and 40.4 kg, was collected. The sheep were anesthetized using intravenous pentobarbital and pancuronium to ensure adequate sedation and to prevent spontaneous breathing. Animals were positive pressure ventilated during experiments using a custom built dual Harvard apparatus piston ventilator designed for computer control. Respiratory rate for animals ranged from 15 to 18 breaths per minute. Two 4DCT images were acquired for each animal with a short (less than 10 minutes) time interval in between scans. The animals were not moved between scans. Images were acquired in the prone position using the dynamic imaging protocol with a pitch of 0.1, slice collimation of 0.6 mm, rotation time of 0.5 sec, slice thickness of 0.75 mm, slice increment of 0.5 mm, 120 kV, and 400 mAs. The airway pressure signal was simultaneously recorded with the X-ray projections and images were reconstructed retrospectively using the B30f kernel to produce a full inspiration image (EI) and end

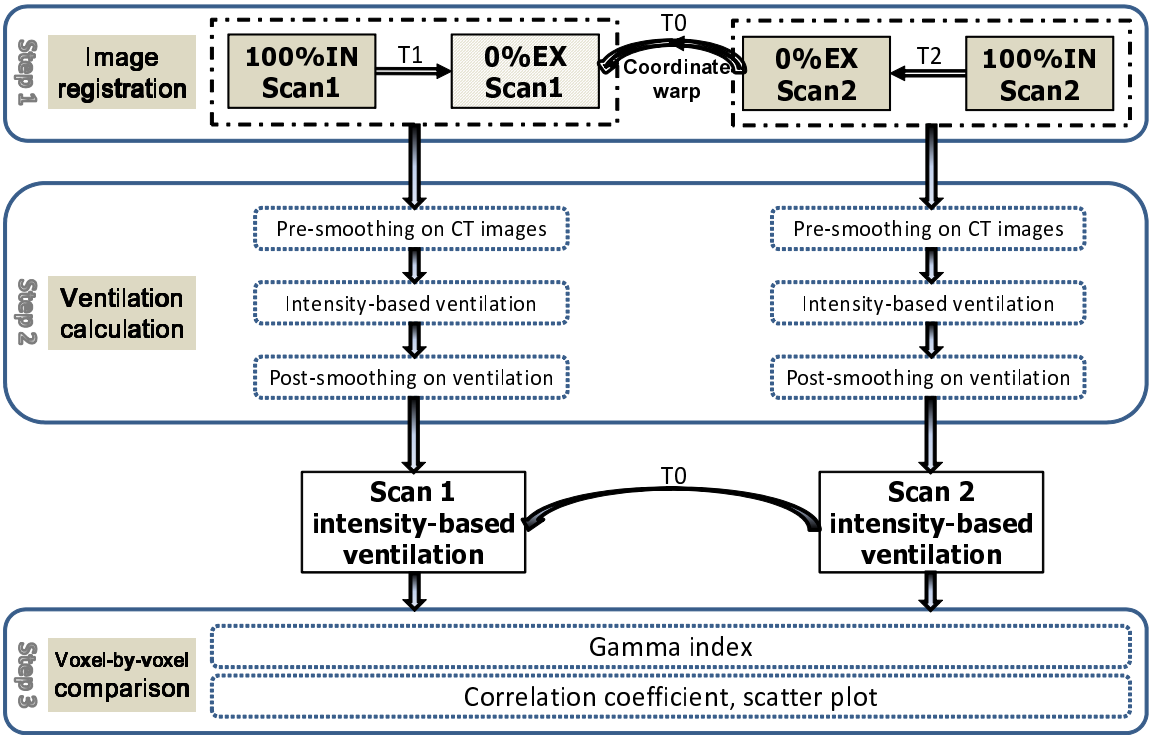

Figure 3.1. Block diagram shows the processing dataflow for reproducibility of intensity-based ventilation metrics. Two complete 4DCT scans are acquired with a short time interval in between acquisitions. The intensity-based ventilation maps for scan one and two are calculated from the original CT images EE, EI and the corresponding registration displacement fields. The ventilation maps for scan two are transformed to the space of scan one for reproducibility assessment.

Table 3.1. Summary of the image registrations performed to calculate intensity-based ventilation.

Trans. Name	Image Transformed	Transformation Is Used To
T0	scan two EE $\rightarrow$ scan one EE	Transform the scan two ventilation map into the scan one EE coordinate, producing $JAC_{T2} \circ T0$
T1	scan one EI $\rightarrow$ scan one EE	Get scan one ventilation JAC_{T1}
T2	scan two EI $\rightarrow$ scan two EE	Get scan two ventilation JAC_{T2}

Refer to Figure 3.1 for names of the images and the transformations.

exhalation image (EE). These are the same data sets previously analyzed in [87].

3.3.2.2 Human Subjects

All data from human subjects was gathered under a protocol approved by the University of Iowa Institutional Review Board. The human data consists of 4DCT data from ten human subjects about to undergo radiation therapy for lung cancer. While thirteen human subjects enrolled in the study, data were not analyzed for three (two withdrew prior to data acquisition and one experienced substantial coughing during the 4DCT scan making the images unusable). The subjects included five males and five females, with ages ranging from 31 to 78 years, with an average age of 59±17 (mean ± standard deviation) years. These subjects, with the exception of H-15, are the nine subjects evaluated in [87].

Prior to imaging, each subject was trained using a biofeedback system (RESP @ RATE, Intercure Ltd., Lod Israel) to identify and support maintaining their nominal breathing rate. Musical cues were used to pace respiration during imaging, using a technique developed at our institution previously shown to have high success [94].

Two 4DCT scans were acquired for each subject, with a short time between scans (see Table 2.3 in Chapter 2). The subjects left the scanner table between scans. Images were acquired in the supine position using the dynamic imaging protocol with a pitch of 0.1, slice collimation of 0.6 mm, rotation time of 0.5 sec, slice thickness of 2 mm, slice increment of 0.5 mm, 120 kV, and 700 mAs. The pressure signal was simultaneously recorded with the X-ray projections and images were reconstructed retrospectively with the B30f kernel to produce a full inspiration image (EI) and end

exhalation image (EE).

3.3.3 Data processing

3.3.3.1 Pre-processing

After image acquisition and reconstruction, all images were examined for evidence of severe breathing artifacts or other acquisition problems. Such artifacts may disrupt the image registration process and lead to poor registration results and erroneous lung expansion measurements. For the ten human cases and three animal cases considered here, no significant image artifacts or other problems were detected.

Prior to image registration, the images of the animal subjects were resampled to size 288 $\times$ 288 $\times$ 352 with voxel size 1 mm $\times$ 1 mm $\times$ 1 mm. Images of the human subjects were resampled to the same voxel size but with image size 304 $\times$ 304 $\times$ 320. The Pulmonary Workstation 2.0 software (VIDA Diagnostics, Inc., Iowa City, IA) was used to identify the lung regions in the CT images. Blood vessels and the bronchial tree were included in the lung segmentation. The binary whole lung mask obtained from the segmented lung was used to limit the spatial domain of the image registration and subsequent transformation-based lung function analysis. For the intensity-based ventilation analysis, only voxels in the range [-999, -250] were used to calculate ventilation estimates, as in [14]. The lung volume was calculated by counting the number of voxels in the lung region and multiplying by the voxel volume.

3.3.3.2 Deformable Image Registration

For each subject, the EI image was registered to the EE image using tissue volume preserving nonrigid registration algorithm developed by our group [109, 97, 98, 87]. The algorithm uses a cubic B-spline transformation model and multiresolution optimization procedure to minimize the sum of squared tissue difference (SSTVD) [63], subject to a Laplacian regularization constraint. Subvoxel accuracy of the registration algorithm compared to manually identified landmarks has been previously reported for transformations T0, T1, and T2, for the same set of subjects in this chapter except subject H-15 [87]. All ventilation images in this study were subsequently derived from this registration algorithm with the same registration parameters.

3.3.3.3 Intensity-based Measures of Ventilation

With the CT image intensities and spatial correspondence between the registration pair EE and EI, SAC can be computed via Equation 3.3, measuring specific air volume change. In addition, the Jacobian of the registration displacement field (Equation 2.5) measures the local volume change in a region. Both SAC and the Jacobian are widely used as ventilation estimates, but they represent different physical phenomena. SAC measures the fraction of air volume change, while the Jacobian measures the relative regional volume change [83]. In addition, the two estimates have different quantities, for example, a 5% change in SAC and a 5% change in the Jacobian represent different quantities of physiological volume change. In this section we will show that an intensity-based Jacobian, which measures the same local volume

change as the transformation-based Jacobian, can be calculated from the intensity change in registered CT image pair. The intensity-based Jacobian enables a direct comparison between the intensity-based and transformation-based methods.

SAC is defined by Castillo et al. [14] as

$$\text{SAC} = \frac{f_2 - f_1}{f_1(1 - f_2)}, \tag{3.4}$$

where f_1 and f_2 are the air fractions in a region in two different inflation conditions. We can write

$$f_1 = \frac{V_{\text{air},1}}{V_1} \qquad f_2 = \frac{V_{\text{air},2}}{V_2},$$

where $V_{\text{air},1}$ and $V_{\text{air},2}$ are the air volumes in conditions 1 and 2 and V_1 and V_2 are the volumes of the region in conditions 1 and 2.

From Hoffman's work [110], we also know that if we assume the lung is composed of only air and tissue, then

$$f_1 = -\frac{\text{HU}_1}{1000} \qquad f_2 = -\frac{\text{HU}_2}{1000}, \tag{3.5}$$

where HU_1 and HU_2 are the mean CT values in the region in conditions 1 and 2.

Note that

$$\text{SAC} + 1 = \frac{\frac{f_2}{1-f_2}}{\frac{f_1}{1-f_1}} = \frac{\frac{V_{\text{air},2}}{V_{\text{tissue},2}}}{\frac{V_{\text{air},1}}{V_{\text{tissue},1}}}.$$

If we assume that there is no tissue volume change between conditions 1 and 2, then $V_{\text{tissue},1} = V_{\text{tissue},2}$. In that case, we can write

$$\text{SAC} + 1 = \frac{V_{\text{air},2}}{V_{\text{air},1}}.$$

If we define the volume ratio, VR, as

$$\mathrm{VR} = \frac{V_2}{V_1},$$

it is straightforward to show that

$$\mathrm{SAC} + 1 = \frac{f_2}{f_1}\,\mathrm{VR},$$

or

$$\mathrm{VR} = \frac{f_1}{f_2}(\mathrm{SAC} + 1). \tag{3.6}$$

From Equation 3.4 we have

$$f_2 = \frac{f_1(\mathrm{SAC} + 1)}{1 + f_1\mathrm{SAC}},$$

which, if substituted into Equation 3.6 and combined with $\frac{V_{\mathrm{air},1}}{V_1} = \frac{-\mathrm{HU}_1}{1000}$, produces

$$\mathrm{VR} = -\frac{\mathrm{HU}_1}{1000}\mathrm{SAC} + 1, \tag{3.7}$$

where HU_1 is the CT intensity at a voxel of interest in the fixed image. Compared to (3.6), the form in (3.7) is easier to compute.

Substituting (3.4) into (3.6) yields

$$\mathrm{VR} = \frac{1 - f_2}{1 - f_1}, \tag{3.8}$$

which can be written using (3.5) as

$$\mathrm{IJAC} \;=\; \mathrm{VR} = \frac{1000 + \mathrm{HU}_1}{1000 + \mathrm{HU}_2}. \tag{3.9}$$

Thus, VR, which measures the same the volume ratio as the transformation-based Jacobian, can be calculated directly from the Hounsfield unit change within the region.

We will refer to the volume ratio calculated using Equation 3.9 as the *intensity-based Jacobian* (IJAC). An alternate derivation of equations 3.6 and 3.9 based on the definitions of SAC and IJAC is given in appendix C.1.

An advantage of using IJAC (Equation 3.9) rather than SAC is that a direct comparison between IJAC and TJAC (Equation 2.5) is possible. Thus, with Equation 3.9 we can directly compare IJAC vs. TJAC reproducibility and compare to previous work using the transformation-based Jacobian (such as [11] and [87]). Comparisons to SAC-based work (such as [14, 13, 47]) are also possible using Equation 3.6 or 3.7.

For the intensity-based ventilation analysis in each scan, lung voxels from the CT images of scan one EE and scan two EE were delineated by an intensity-based segmentation algorithm, with HU values in the range [-999,-250] representing pulmonary parenchyma [14, 13, 47]. The spatial transformation established from the image registration linked the fixed image (EE) and moving image (EI). The warping function $\mathbf{h}(\mathbf{x})$ interpolates the moving image and maps the set of moving voxels to the corresponding location in the fixed image. The resulting intensity-based Jacobian maps in the coordinate system of EE, representing fractional change in air content during lung expansion.

Following the approaches from [14, 13, 47], each CT input image was smoothed by local averaging with kernel size $3 \times 3 \times 3$, to suppress noise in the original CT images and reduce the effects of image registration error, we then performed an additional $9 \times 9 \times 9$ local averaging on the preliminary IJAC results to generate

the final ventilation maps. In contrast to TJAC, which is directly computed from the displacement field from image registration, the calculation of IJAC also involves the intensity information of the registered CT images at EE and EI. Consequently, the increased noise in the intensity-based ventilation maps and poorer reproducibility may come from two sources: noise in original CT images and image registration error. To test how different levels of filtering affect reproducibility, we processed the data for all human subjects with different amounts of low-passing filtering applied to the CT images prior to registration. We tested the change of IJAC reproducibility for CT images without smoothing and with different scales of smoothing using local average kernels $3 \times 3 \times 3$, $7 \times 7 \times 7$, $11 \times 11 \times 11$, and $15 \times 15 \times 15$ voxels. Results for effects of filtering on reproducibility are presented in Section 3.4.3.

Because of the use of the thresholds [-999,-250], not every voxel in the lung region is assigned a ventilation value. Therefore, when we warp JAC_{T2} back to the coordinate of scan one EE, nearest neighborhood interpolation was used to warp voxels outside of the threshold range, instead of the usual linear interpolation.

3.3.3.4 Analytical Analysis of Noise

As shown in Equations 3.3 and 3.9, the intensity-based SAC and intensity-based Jacobian are computed from the CT values of the EE and EI images and the registration transformation. Therefore the calculated ventilation measures are vulnerable to CT image noise and registration errors. In [14], noise filtering was used to reduce these effects. The error in the intensity-based SAC and intensity-based Jacobian ventilation measurements caused by the perturbation in CT HU measurement

can be computed analytically from Equation 3.3 using the propagation of error theory [111]. Details of the derivation of the coefficient of variation for the intensity-based SAC and the Jacobian are described in Appendices D.1 and D.2.

Equation 3.10 shows the impact of CT noise standard deviation σ_{CT} on the coefficient of variation (CV) of SAC measurements,

$$\frac{\sigma_{\mathrm{SAC}}}{\mu_{\mathrm{SAC}}} = \sigma_{\mathrm{CT}} \frac{\sqrt{{I_f}^2(I_f+1000)^2 + {I_m}^2(I_m+1000)^2}}{I_f(I_m-I_f)(I_m+1000)}, \tag{3.10}$$

where μ_{SAC} is the mean of SAC, and I_f and I_m are the CT intensity values at a voxel of interest in the EE and EI image.

Similarly, from Equation 3.9, we can perform a similar noise analysis for the intensity-based Jacobian, which yields:

$$\frac{\sigma_{\mathrm{IJAC}}}{\mu_{\mathrm{IJAC}}} = \sigma_{\mathrm{CT}} \frac{\sqrt{(I_m+1000)^2 + (I_m-I_f)^2}}{(I_f+1000)(I_m+1000)}, \tag{3.11}$$

where μ_{IJAC} is the mean of IJAC.

The curves in Figure 3.2 plot the error propagation from CT noise to CV of intensity-based ventilation measurements for several fixed EI HU values. The vertical axis is $\frac{\sigma_{\mathrm{x}}}{\mu_{\mathrm{x}}\sigma_{\mathrm{CT}}}$ where x represents either SAC or intensity-based Jacobian. For example, for an EE-EI pair with EE $= -600$ HU and EI $= -975$ HU, Figure 3.2 shows $\frac{\sigma_{\mathrm{SAC}}}{\mu_{\mathrm{SAC}}} = 0.043\,\sigma_{\mathrm{CT}}$ and $\frac{\sigma_{\mathrm{JAC}}}{\mu_{\mathrm{JAC}}} = 0.038\,\sigma_{\mathrm{CT}}$. If we assume $\sigma_{\mathrm{CT}} = 10$ HU [112], this produces a coefficient of variation in the SAC of 43% and a coefficient of variation in the IJAC of 38%, indicating the intensity-based ventilation measurements are noisy. Even with local averaging to reduce noise in the CT images, the impact of CT noise on the final intensity-based ventilation may be large and should not be neglected. Additionally,

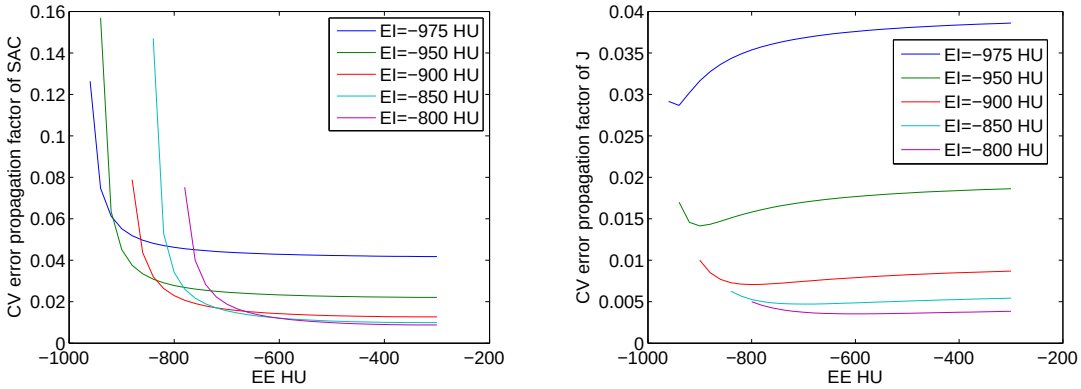

Figure 3.2. Error propagation to coefficient of variation for intensity-based SAC and IJAC. Vertical axis shows $\frac{\sigma_x}{\mu_x \sigma_{CT}}$, where x represents either SAC or intensity-based Jacobian. EE represents the mean CT value in a region of interest at end expiration, while EI represents the mean CT value in that same region at end inspiration. (a) SAC. (b) IJAC.

any registration error will further increase variability of ventilation estimates.

3.3.3.5 Reproducibility Analysis

After calculating the intensity-based ventilation maps from two separate 4DCT data sets, a metric is needed to compare these two ventilation maps regionally and quantitatively. In our previous work [87], we introduced the Jacobian ratio map, the colored 2D kernel density scatter plot, and the modified Bland-Altman plot to show the voxel-by-voxel relationship of ventilation in two scans, and calculated statistical parameters such as the mean and standard deviation of Jacobian ratio map, the correlation coefficient between two Jacobian maps, and the slope of linear regression line. However, in this chapter since the SAC map calculated from Equation 3.3 and IJAC map calculated from Equation 3.9 may not be defined at all lung voxels, we propose to use a modified gamma index to allow for approximate matching.

The gamma index was developed in quantitative dose evaluation for RT dose delivery [113]. In addition to considering the ventilation difference, the gamma index adds a term to tolerate possible spacial misalignment, which may result from subject motion, image acquisition problems, and image registration errors. The gamma index is defined as:

$$\begin{aligned}\gamma(\overrightarrow{r_2},\overrightarrow{r_1}) =& \min_{\overrightarrow{r_2}}\{\Gamma(\overrightarrow{r_2},\overrightarrow{r_1})\} \\ =& \min_{\overrightarrow{r_2}}\{\sqrt{(\frac{\overrightarrow{r_2}-\overrightarrow{r_1}}{\Delta d_0})^2+(\frac{S_2(\overrightarrow{r_2})-S_1(\overrightarrow{r_1})}{\Delta S_0})^2}\}\end{aligned} \tag{3.12}$$

where $\overrightarrow{r_1}$ and $\overrightarrow{r_2}$ are the voxel positions of $\mathrm{JAC_{T1}}$ and $\mathrm{JAC_{T2}} \circ \mathrm{T0}$ points respectively. $S_1(\overrightarrow{r_1})$ and $S_2(\overrightarrow{r_2})$ are IJAC values in two scans. Δd_0 is the criteria for spatial offset tolerance and ΔS_0 is the IJAC difference criteria. For any given location in $\mathrm{JAC_{T1}}$ there are as many Γ as there are evaluated points in the search space in $\mathrm{JAC_{T2}} \circ \mathrm{T0}$. The minimum value of Γ is the final γ value.

Since breathing effort, and thus ventilation, may vary subject to subject, we have modified Equation 3.12 so that ventilation values are compared on a percentage difference basis, depending upon a tolerance Δp_0,

$$\gamma(\overrightarrow{r_2},\overrightarrow{r_1}) = \min_{\overrightarrow{r_2}}\{\sqrt{(\frac{\overrightarrow{r_2}-\overrightarrow{r_1}}{\Delta d_0})^2+(\frac{S_2(\overrightarrow{r_2})-S_1(\overrightarrow{r_1})}{S_1(\overrightarrow{r_1})\times\Delta p_0})^2}\} \tag{3.13}$$

In this chapter we use $\Delta d_0 = 4$ mm and $\Delta p_0 = 0.1$ (i.e., 10 percent tolerance) as default parameters. The gamma index tries to balance between differences in specific ventilation and the distance between matching voxels. The pass threshold of the γ test is $\gamma = 1$. A voxel with $\gamma \leq 1$ passes the test, implying that there is a matching voxel in the other ventilation map with less than 10% ventilation difference within a

distance of 4 mm. The pass region percent rate is computed by counting all passed voxels divided by total number of pulmonary parenchyma voxels.

3.3.3.6 Respiratory Effort Compensation

As described in [87], even with training and audio guidance, for some subjects the level of breathing effort varied between the two pairs of scans gathered to assess reproducibility. In [87] the authors used differences in lung volume to normalize for breathing effort differences. As shown in Table 2.3, some subjects had a significantly higher or lower breathing efforts in scan two than scan one. In this case, the gamma metric above would probably draw a low pass percentage because it becomes harder to find a similar ventilation value in the certain search space. The normalized gamma is introduced to normalize the $\mathrm{JAC}_{\mathrm{T2}} \circ \mathrm{T0}$ to the scale of $\mathrm{JAC}_{\mathrm{T1}}$. As described in [87], since the average Jacobian should reflect the global volume change in the lung, the EE and EI lung volumes can be used as a global linear normalization factor to adjust for lung volume differences between scans one and two.

By definition, the Jacobian is the ratio of EI volume and EE volume in a specified region. Therefore for corresponding locations in scan one and scan two, we have the relation:

$$\frac{\mathrm{JAC}_1}{\mathrm{JAC}_2} \sim \frac{(\frac{\text{EI volume}}{\text{EE volume}})_{\text{scan1}}}{(\frac{\text{EI volume}}{\text{EE volume}})_{\text{scan2}}} \tag{3.14}$$

where JAC_1 and JAC_2 are Jacobian values at corresponding locations in $\mathrm{JAC}_{\mathrm{T1}}$ and $\mathrm{JAC}_{\mathrm{T2}} \circ \mathrm{T0}$.

Then, the normalized gamma can be computed by Equation 3.16 as:

$$\hat{\gamma}(\overrightarrow{r_2}, \overrightarrow{r_1}) = \min_{\overrightarrow{r_2}}\{\sqrt{(\frac{\overrightarrow{r_2} - \overrightarrow{r_1}}{\Delta d_0})^2 + (\frac{\hat{S_2}(\overrightarrow{r_2}) - S_1(\overrightarrow{r_1})}{S_1(\overrightarrow{r_1}) \times \Delta p_0})^2}\} \tag{3.15}$$

where

$$\hat{\mathrm{S}_2} = \mathrm{S}_2 \times \frac{(\frac{\text{EI volume}}{\text{EE volume}})_{\text{scan1}}}{(\frac{\text{EI volume}}{\text{EE volume}})_{\text{scan2}}}. \tag{3.16}$$

3.4 Results

3.4.1 Reproducibility in Animal

The animal subjects used in this chapter are the same as in Chapter 2. Refer to Table 2.2 in Chapter 2 for a listing the lung volumes and the tidal volumes in two scans measured for the three animal subjects in this study.

Figure 3.3 shows IJAC and TJAC color maps of the scan one ventilation estimate, the scan two ventilation estimate, the ratio map, and the gamma map for animal S-1. Non-pulmonary voxels outside the range [-999, -250] HU were not processed. As illustrated in Figure 3.1, the ventilation map from scan two is transformed through the T0 transformation to be converted into the coordinate system of scan one. The T0 transformation allows the two ventilation images to be directly compared in the same coordinate framework, and allows us to compute the voxel-by-voxel gamma comparison.

Figure 3.4 (a) shows 2D kernel density estimates for the voxel-by-voxel scatter plot of the scan one and scan two IJAC data for one animal subject. The scatter plot is displayed with a color overlay that shows the density of joint cumulative distribution of the $\mathrm{JAC_{T1}}$ and $\mathrm{JAC_{T2}}$ data. Marginal histograms of the $\mathrm{JAC_{T1}}$ and $\mathrm{JAC_{T2}}$ data are plotted along the top and right side of the figures. Pearson's correlation coefficient

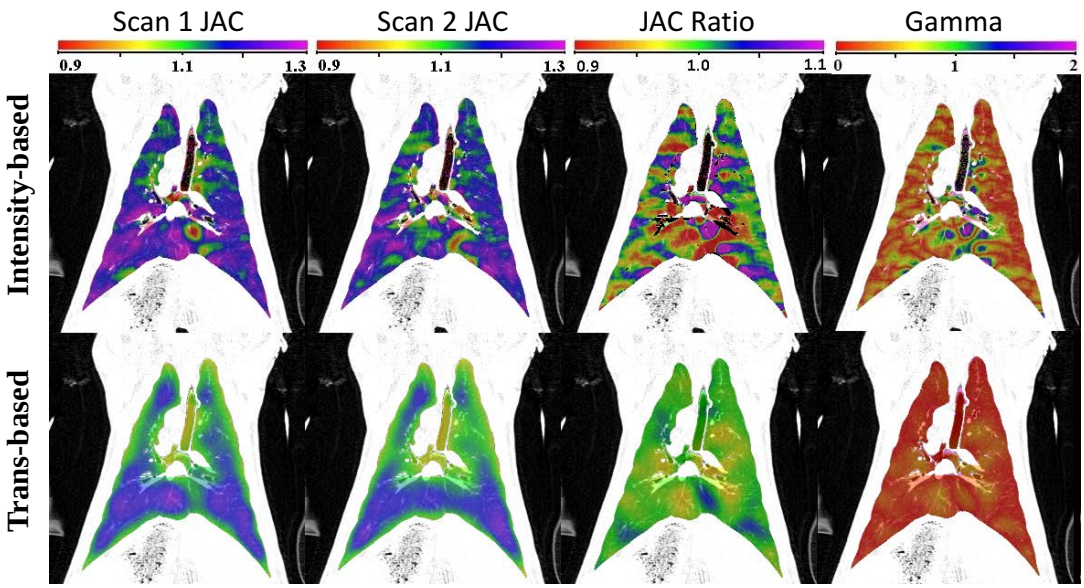

Figure 3.3. IJAC (top) and TJAC (bottom) color maps of (left to right) scan one Jacobian, scan two Jacobian, Jacobian ratio, and gamma map for animal subject S-1.

was computed. Averaged across all animal subjects, the correlation coefficient is 0.367. Figure 3.4 (b) is the Bland-Altman plot which shows the ratio of the two measurements versus the geometrical mean of two measurements. The solid line is the reference line that equals to one, representing perfect agreement in the two measurements. The dashed line is the average ratio in IJAC measurements. The scatter plot and Bland-Altman plot of TJAC for the same subject S-1 are shown in Figure 3.4 (c) and (d), adapted from [87]. The axis of the scatter plots for IJAC and TJAC was set with the same scale for easier comparison. The statistical parameters for animal subjects are summarized in Table 3.2.

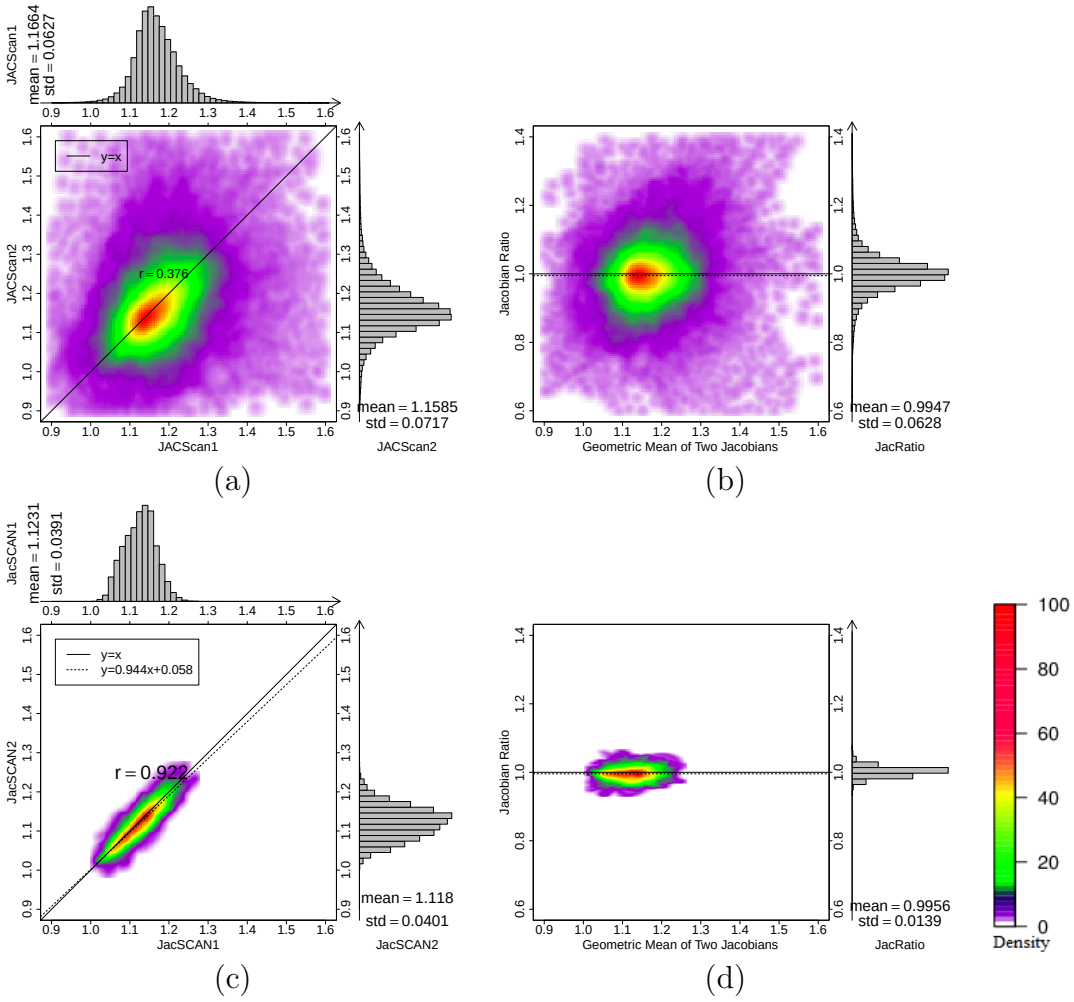

Figure 3.4. Reproducibility results for animal S-1. (a) IJAC density scatter plot and marginal histograms. (b) IJAC modified Bland-Altman plot. (c) TJAC density scatter plot and marginal histograms. (d) TJAC modified Bland-Altman plot.

3.4.2 Reproducibility in Human

Similar to the animal subjects, the human subjects used in this chapter are the same as in Chapter 2. Refer to Table 2.3 in Chapter 2 for a listing of the lung volumes, tidal volumes in two scans measured for the ten human subjects in this study. Breathing effort variation is more apparent in the free-breathing humans compared to mechanically ventilated animals. The time intervals between two scans are also listed. Note that subject H-8 received the second scan 7 days after the first scan, which is substantially longer than the time difference for the other subjects.

Figures 3.5 and 3.6 show the coronal view of IJAC and TJAC for scan one ventilation, scan two ventilation, the ratio map and the gamma comparison map for human subjects H-2 and H-8. As with the animal subjects, the scan two ventilation image has been transformed into the coordinate system of scan one using the T0 transformation. Subjects H-2 and H-8 were selected to illustrate cases with good and poor reproducibility when comparing the scan one to scan two results, as in [87].

Similar to Figure 3.4, Figure 3.7 and 3.8 shows the 2D kernel density estimates for the voxel-by-voxel scatter plot and Bland-Altman plot of the scan one and scan two for the two human subjects H-2, H-8. Pearson's correlation coefficient was computed, with an average correlation of 0.478 in all ten human subjects. For comparison purposes, we use identical scales in all of the plots for a given subject. All figures for the transformation-based ventilation in this chapter were reproduced from [87].

Figure 3.9 shows one example subject to illustrate the differences between the inconsistent ventilation map ($\gamma > 1$) for the IJAC and TJAC methods. Both maps

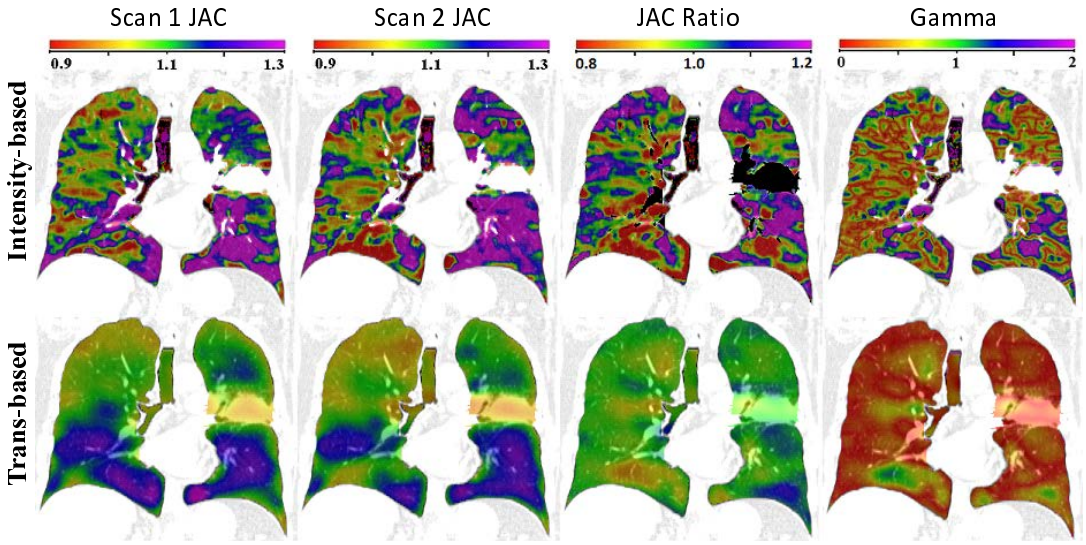

Figure 3.5. IJAC (top) and TJAC (bottom) color maps of (left to right) scan one Jacobian, scan two Jacobian, Jacobian ratio, and gamma map for human subject H-2.

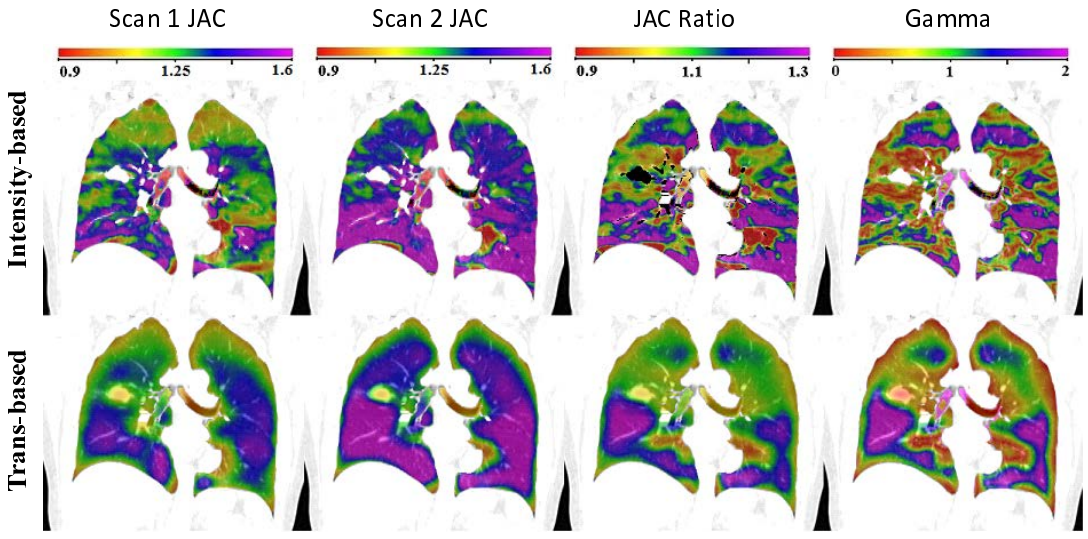

Figure 3.6. IJAC (top) and TJAC (bottom) color maps of (left to right) scan one Jacobian, scan two Jacobian, Jacobian ratio, and gamma map for human subject H-8.

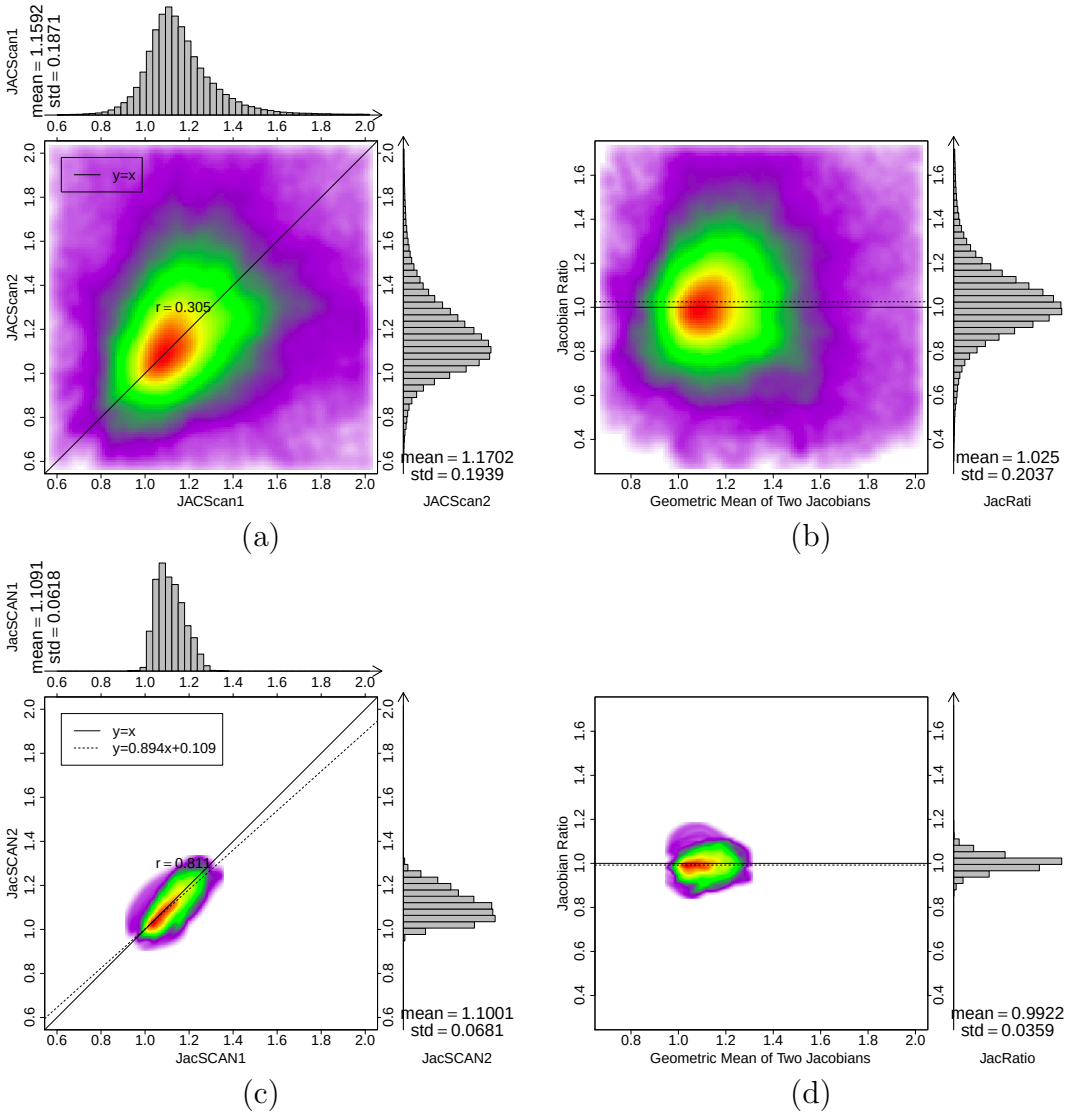

Figure 3.7. Reproducibility results for human subject H-2. (a) IJAC density scatter plot and marginal histograms. (b) IJAC modified Bland-Altman plot. (c) TJAC density scatter plot and marginal histograms. (d) TJAC modified Bland-Altman plot.

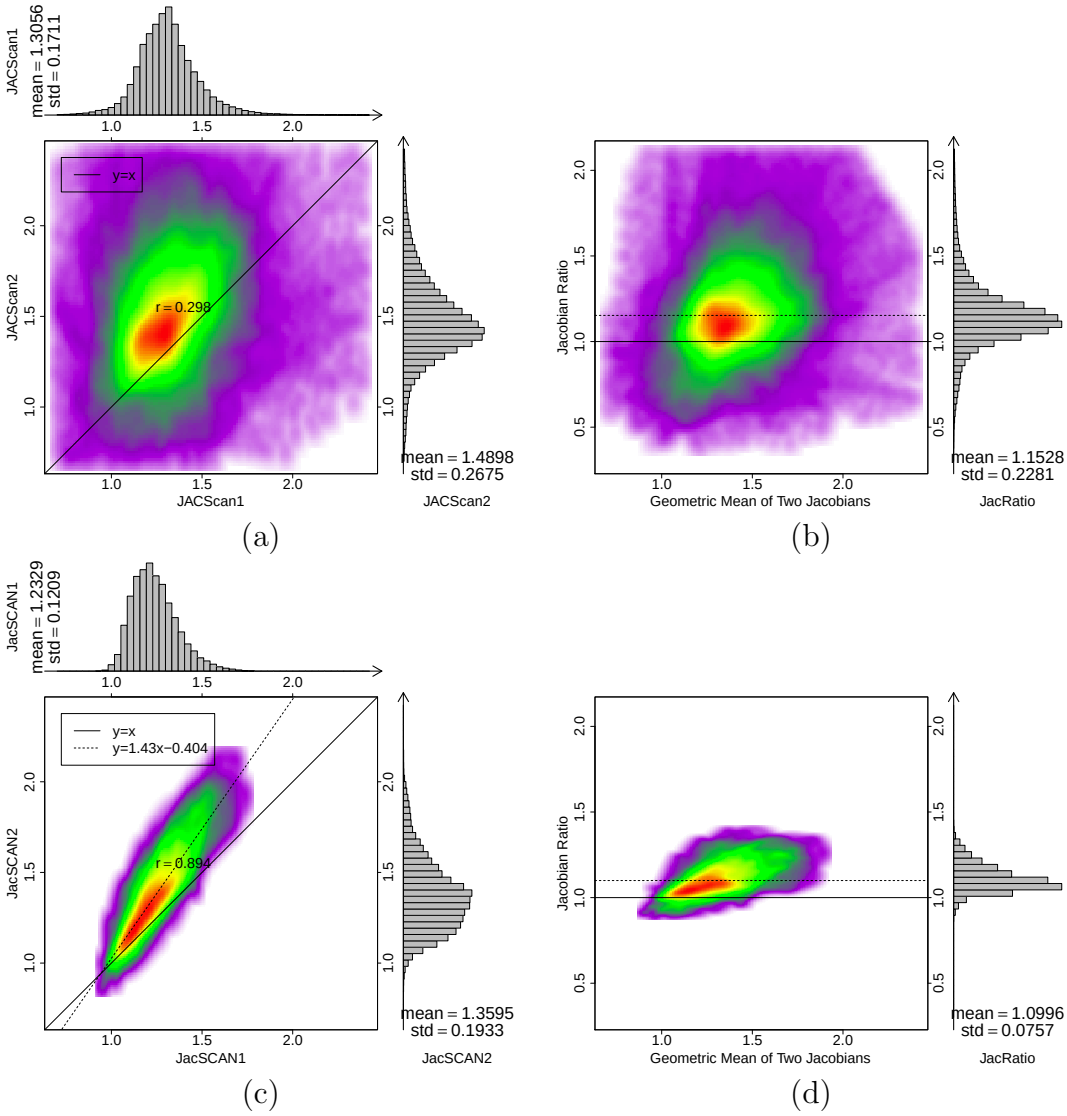

Figure 3.8. Reproducibility results for human subject H-8. (a) IJAC density scatter plot and marginal histograms. (b) IJAC modified Bland-Altman plot. (c) TJAC density scatter plot and marginal histograms. (d) TJAC modified Bland-Altman plot.

are calculated after respiratory effort correction and use the same color scale. Regions that passed the gamma test ($\gamma \leq 1$) were not overlaid with color. Figure 3.9 shows the TJAC inconsistent ventilation regions are more focal and fewer in number than the IJAC inconsistent ventilation regions. Similar results were observed for the other nine human data sets. In several cases, TJAC defects were limited spatially to the lower lobes of the lung, while in all cases we observed IJAC inconsistent ventilation regions throughout the lung. In other words, TJAC reported changes in ventilation between scanning sessions that were physiologically clustered, primarily in the lower lobes where ventilation is greatest. Alternatively, IJAC reported changes in ventilation that were small in volume and distributed randomly in all lobes of the lung.

If the subject, image acquisition, image registration and ventilation analysis were perfectly reproducible, the ventilation values computed from scan one and scan two would match exactly at each voxel, the gamma maps would be equal to zero, the correlation coefficients would be equal to one, and the standard deviation of the ratio map would be equal to zero. Table 3.2 lists the statistics for intensity-based Jacobian, and transformation-based Jacobian. It summarizes statistical parameters including Pearson's correlation coefficients, gamma pass rate, gamma pass rate after effort normalization, and standard deviation of the ratio map. Compared to the statistics table in [87], Table 3.2 adds the gamma pass rates for the transformation-based Jacobian. Due to the thresholding of pulmonary parenchyma voxels, the ventilation map may have "holes", therefore the standard deviation is calculated only for those voxels where JAC_{T1} and JAC_{T2} both have ventilation values. The reproducibility of

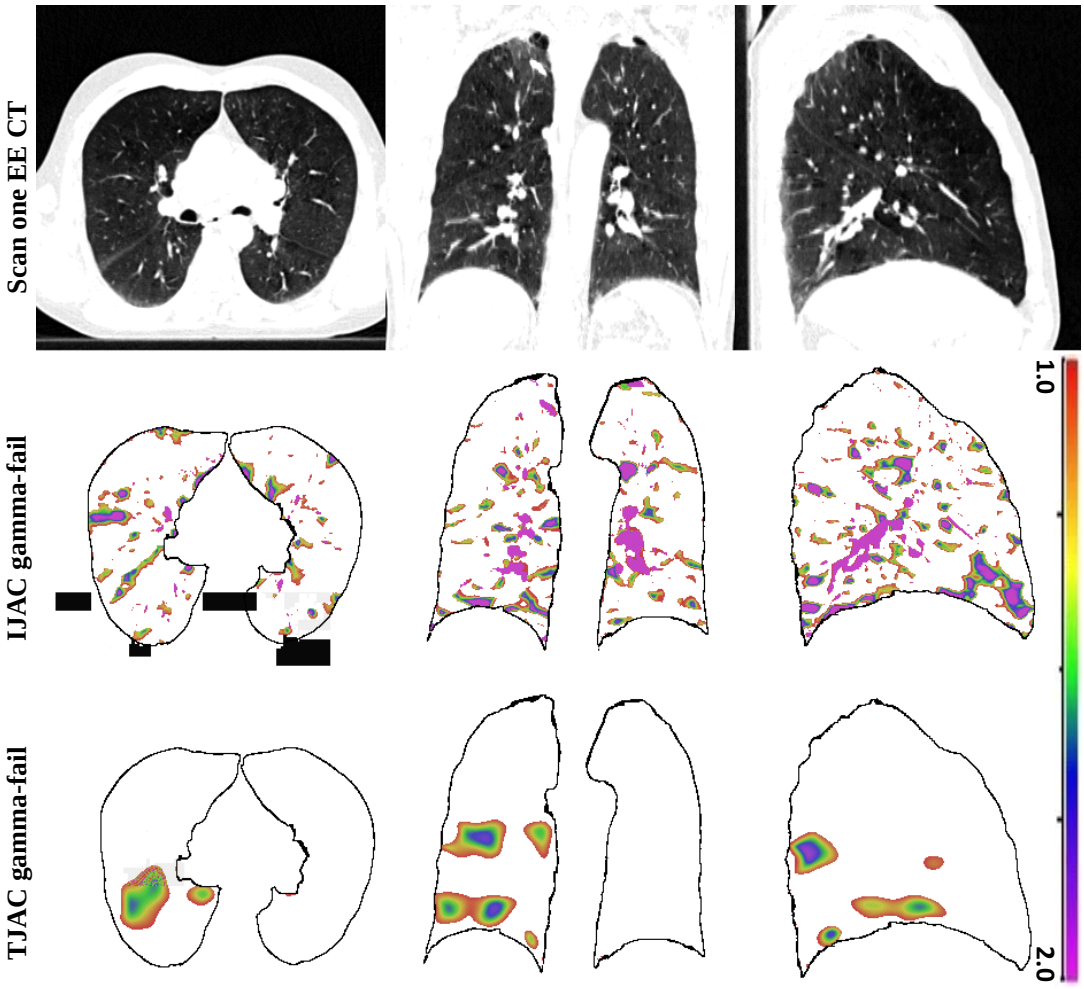

Figure 3.9. Colored panel shows the differences between the scattered distribution of inconsistent ventilation estimate in IJAC and the clustering of those inconsistencies in TJAC for subject H-7. The gamma maps were calculated after respiratory effort normalization. Color scales are shown on the right.

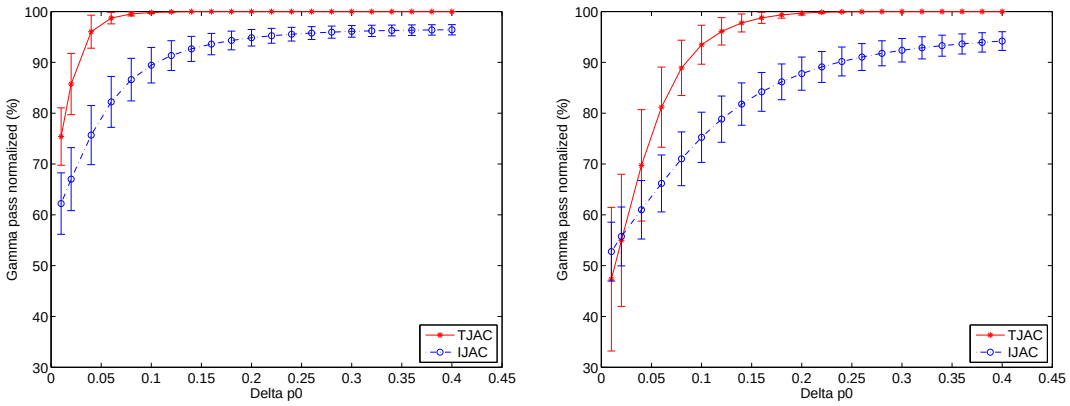

Figure 3.10. The gamma pass percent changes with different Δp_0 in Equation 3.13 for the intensity-based Jacobian, IJAC, and, the transformation-based Jacobian, TJAC. (a) Average of 3 sheep data sets with normalization; (b) Average of 10 human data sets with normalization.

the transformation-based Jacobian is described more completely in [87].

In Equation 3.13, Δp_0 is the value tolerance criterion and Δd_0 is the distance tolerance criterion in the gamma metric. Both relaxed Δp_0 and relaxed Δd_0 will increase the possibility for one voxel to find a similar ventilation value in the other map within a given neighborhood. Figure 3.10 shows the gamma pass percent for different Δp_0 for TJAC and IJAC, with $\Delta d_0 = 4$ mm.

3.4.3 Effects of Low-pass Filtering

. To test how different levels of filtering affect reproducibility, we processed the data for all human subjects with different amounts of low-passing filtering applied to the CT images prior to registration. Figures 3.11 show the effects of different levels of low-pass filtering on reproducibility for subject H-8. The top row shows the sagittal view of $\mathrm{JAC}_{\mathrm{T1}}$ and the bottom row shows the smoothed color density scatter plots.

Table 3.2. Summary of reproducibility statistics for three animal subjects and ten human subjects, for the intensity-based Jacobian, and the transformation-based Jacobian.

Subject	Intensity-based JAC				Transformation-based JAC			
	Corr. Coef.	Pass (%)	Pass Norm. (%)	JacRatio Std	Corr. Coef.	Pass (%)	Pass Norm. (%)	JacRatio Std
S-1	0.369	93.18	93.05	0.0628	0.922	100	100	0.0139
S-2	0.338	88.74	88.78	0.0737	0.843	99.63	99.60	0.0226
S-3	0.350	86.37	86.17	0.0628	0.887	99.84	99.84	0.0264
H-1	0.473	53.24	85.37	0.1206	0.937	69.74	99.09	0.0565
H-2	0.327	74.04	73.78	0.2037	0.811	99.05	99.10	0.0359
H-4	0.688	76.78	78.95	0.1363	0.860	85.28	90.48	0.0681
H-7	0.247	74.13	76.30	0.1869	0.570	92.80	94.55	0.0515
H-8	0.347	56.34	78.11	0.2281	0.894	67.80	90.99	0.0757
H-9	0.260	62.84	68.38	0.1832	0.772	79.10	93.41	0.0527
H-10	0.469	71.21	71.93	0.1319	0.820	88.53	90.59	0.0635
H-11	0.399	72.04	71.94	0.1564	0.755	88.29	89.56	0.0666
H-12	0.483	72.98	72.25	0.1675	0.850	87.82	88.11	0.0747
H-15	0.536	76.95	77.19	0.1083	0.849	97.47	97.46	0.0399

The "Corr. Coef." column shows correlation coefficients of two ventilation images, the "Pass" column shows the percentage of pass voxels in the gamma map, the "Pass Norm." column shows the pass rate in normalized gamma map, and "JacRatio Std" column shows standard deviation of the Jacobian ratio map.

Ordered left to right, the smoothing kernel sizes for filtering on the original CT images are $7 \times 7 \times 7$, $11 \times 11 \times 11$, and $15 \times 15 \times 15$ voxels.

Figure 3.12 shows change of average gamma pass percent and average correlation coefficient for all human subjects with different levels of low-pass filtering on original CT images. The horizontal axis shows the neighborhood radius in local averaging. The solid line in blue shows the gamma pass percent for IJAC, and the gamma pass percent for TJAC is also drawn in blue dashed line for comparison. The green dotted line shows the correlation coefficient for IJAC, and the green dashed line on the top shows the correlation coefficient for TJAC.

3.5 Discussion

In this study we examined the reproducibility of the intensity-based measure of ventilation using two separate 4DCT image sets within a short interval between acquisitions. We compared these results to those from a transformation-based measure of ventilation. Mechanically-ventilated sheep and human subjects prior to receiving radiation therapy were studied. Since neither the ratio nor difference is appropriate for reproducibility evaluation of intensity-based ventilation, we introduced the gamma indices which consider both ventilation differences and distance to agreement. A normalization strategy was used to compensate for different breathing efforts in the two 4DCT acquisitions. In both intensity-based and transformation-based ventilation, we found the reproducibility obtained in anesthetized, mechanically ventilated animals is slightly better than for the spontaneously-breathing humans. All statistical parameters, including correlation coefficients, gamma pass percentage, and standard

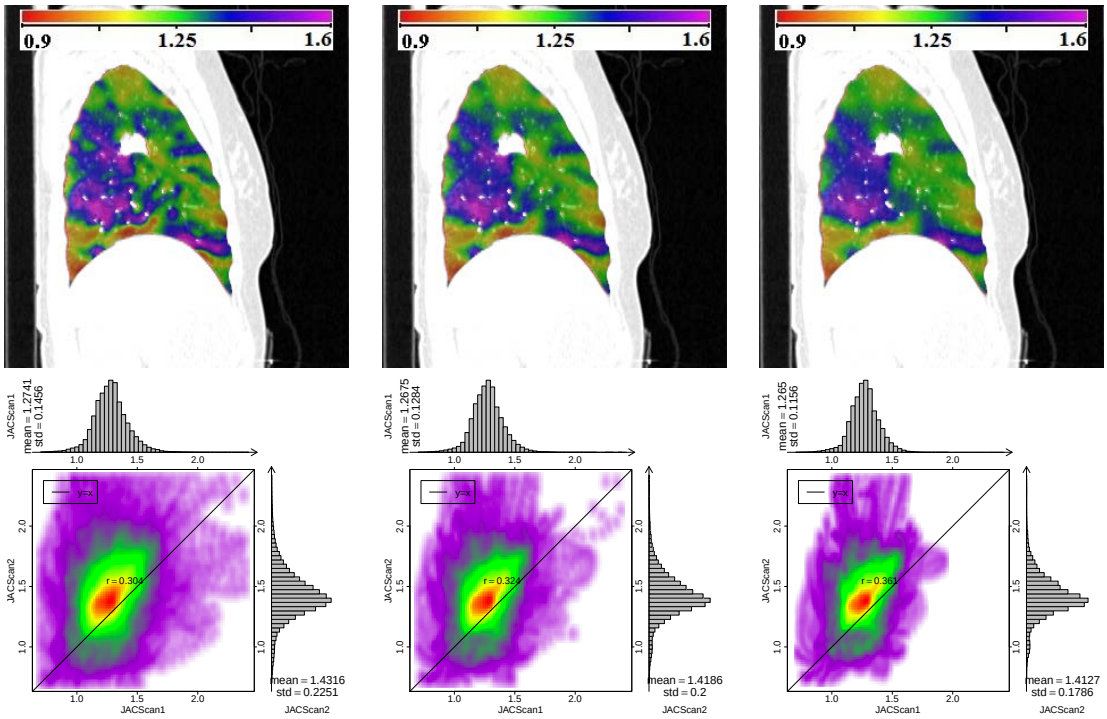

H-9 ($7 \times 7 \times 7$) H-9 ($11 \times 11 \times 11$) H-9 ($15 \times 15 \times 15$)

Figure 3.11. Effects of increased low-pass filtering on reproducibility for subject H-8. The top row shows the sagittal view of JAC_{T1} and the bottom row shows the smoothed color density scatter plots. Ordered left to right, the local average kernel sizes for filtering on the original CT images are $7 \times 7 \times 7$, $11 \times 11 \times 11$, and $15 \times 15 \times 15$ voxels. Histograms and summary statistics are given along the top and right side of each plot. Colorscale is same as in Figure 3.4.

deviation of ratio map, indicate the reproducibility of intensity-based ventilation is worse than that of transformation-based ventilation. The reproducibility of the human IJAC maps showed as correlation coefficients 0.45±0.14, gamma pass rate 70±8 without normalization and 75±5 with normalization. The reproducibility of the human TJAC maps showed as correlation coefficients 0.81±0.10, gamma pass rate 86±11 without normalization and 93±4 with normalization. To study the impact of noise from original CT on the final intensity-based ventilation map, we developed analyt-

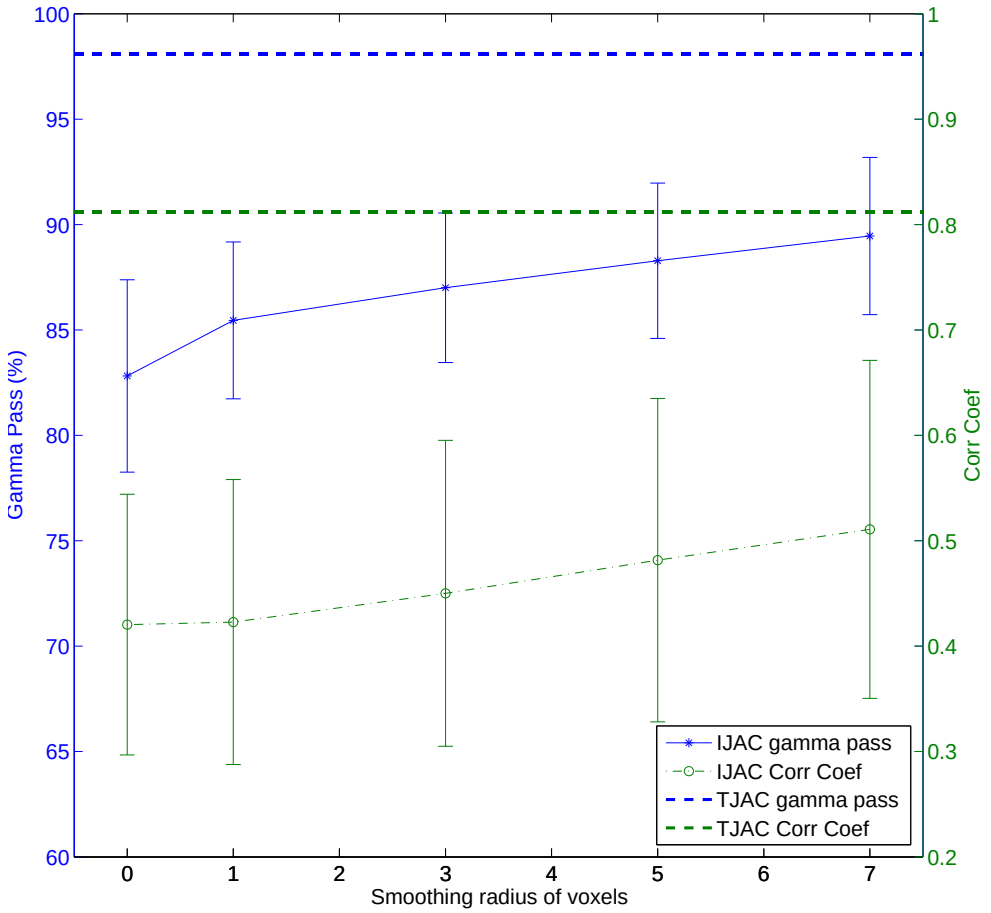

Figure 3.12. Change of mean gamma pass percent and mean correlation coefficient for ten human subjects with low-pass filtering on original CT images with different smoothing kernel sizes. The horizontal axis shows the neighborhood radius for filtering, where smooth radius 0 means no filtering, radius 3 means kernel size $7 \times 7 \times 7$, etc. The solid line in blue shows the gamma pass percent for IJAC, and the gamma pass percent for TJAC is also drawn as the blue dashed line for comparison. The green dotted line shows the correlation coefficient for IJAC, and the green dashed line on the top shows the correlation coefficient for TJAC.

ical models and investigated reproducibility improvement with increased filtering on the CT images. We found that the low-pass filtering in intensity-based ventilation calculation can help remove extreme ventilation values, however the increase of reproducibility is limited, and the spatial resolution of the resulting ventilation map is reduced.

Figures 3.3 shows the reproducibility of the calculated intensity-based Jacobian in the animal model. Though the patterns appear similar, there are still considerable regional differences between JAC_{T1} and $JAC_{T2} \circ T0$. The original-repeat scan voxel-by-voxel correlation coefficients for IJAC range from 0.369 to 0.350 for these animals. Figure 3.4 compares the reproducibility of IJAC and TJAC. We can see the scatter plot of IJAC is more dispersed than that of TJAC. While the scatter distribution of TJAC converges well to the regression line, the linearity of IJAC almost disappear. Since these subjects are anesthetized and mechanically-ventilated animals, they likely represent the best possible case in terms of ventilation map reproducibility.

Figures 3.5 and 3.6 show examples of data from human subjects with good and poor reproducibility based on the statistical parameters in Table 3.2. The lung volumes in Table 2.3 shows that subject H-2 has more consistent lung volumes and tidal volumes than subject H-8. If H-8 has poor reproducibility because of variations in lung volumes and tidal volumes, it may reveal that ventilation regions are not consistently distributed under different pressures. Figure 3.7 and 3.8 shows the IJAC vs. TJAC comparison of scatter plots for subject H-2 and H-8. Subject H-8 had a greater expansion in scan two than in scan one, and it is easy to see that this

respiratory effort difference is clearly reflected in mass center of scatter points over the reference line $y = x$ in both IJAC and TJAC. These scatter plots and histograms clearly show the reproducibility of IJAC is worse than that of TJAC. With the same data, processing, and registration algorithm, the poor reproducibility performance of intensity-based ventilation may be due to the high noise sensitivity of the calculation itself.

Table 3.2 lists statistical parameters for evaluating reproducibility. H-4 had an inter-scan interval of 20 hours and H-8 had an inter-scan interval of 7 days, which is much longer than that for any of the other subjects. However, we do not see any noticeable difference in reproducibility for these two subjects compared to the others. The global linear normalization using lung volumes [87] can offset the effects of different respiratory efforts in the two 4DCT scans and scale the ventilation values of scan two to the same range of scan one. Higher gamma pass rate is found after normalization as shown in Table 3.2. The correlation coefficient between two Jacobian maps and the standard deviation of Jacobian ratio map for IJAC are several times worse than those for TJAC. For all subjects the gamma pass percentage of IJAC is lower than that of TJAC, even after breathing effort normalization. Even though it is known that lung expansion and contraction are not uniform apex to base and ventral to dorsal [87], the subject-specific normalization used to compensate for varying effort between studies in Equation 3.16 is a useful normalization scheme in this situation to compare ventilation maps across scans and calculate gamma indices across subjects. More sophisticated approaches for normalizing for differences in tidal volume may

provide even better results, and this is an area of active research.

Recently Yamamoto et al. [86] also investigated the reproducibility of ventilation, using two cohorts of patients imaged over two different inter-scan intervals. A transformation-based metric (TJAC -1) was used to represent volume change. Moderate voxel-based correlation was reported between two ventilation images (Spearman rank correlation 0.50±0.15). However, we reported correlation coefficients 0.81±0.10 for the human TJAC ventilation estimate. We speculate that reproducibility can be influenced by many factors, such as image acquisition parameters, patient motion control, variations in respiratory rates and pattern, image registration, and ventilation metrics. They found respiratory variation during 4DCT scans would deteriorate the reproducibility, which is consistent with our observation.

Figure 3.9 shows that regions of inconsistent ventilation are more numerous and spatially distributed for the intensity-based Jacobian when compared to the transformation-based Jacobian. In addition, the data in Table 3.2 and Figure 3.10 show that the total number of voxels with $\gamma > 1$ is less for the transformation-based approach compared to the intensity-based approach. This may be due to the increased noise sensitivity of the intensity-based method compared to the transformation-based approach. To track changes in ventilation in a longitudinal study, it is important for the measurement methods to be reproducible and as robust to noise as possible. While we observed similar results to those as shown in Figure 3.9 for all human subjects, a more complete and quantitative evaluation of the spatial distribution of the inconsistent ventilation regions needs to be performed before drawing any final

conclusions.

Compared to transformation-based ventilation, which is directly calculated from the deformation gradient tensor, the intensity-based ventilation approach is derived from both the deformation and intensities of involved CT images. Castillo et al. [14] showed visual and quantitative differences between TJAC and intensity-based SAC. They also concluded that the intensity-based method showed better spatial correction with the clinical standard of nuclear medicine exams. Mathematically, both ventilation approaches make use of deformable image registration. After the displacement field is established, the transformation-based Jacobian is directly calculated, while the intensity-based method uses the original CT images for intensity information, which may introduce additional noise. Therefore, the TJAC is influenced by image registration error, however intensity-based method is influenced by both registration error and CT intensity noise. The analytical error analysis of the SAC and IJAC measurements that shows the impact of CT noise on the measurements may be large and should not be neglected. As shown in Table 3.2, for all subjects the gamma pass rate of the TJAC maps is much higher than that of the IJAC maps.

The Equation 3.7 provides a way to link the SAC and Jacobian, which have different definitions and quantities to show tissue expansion as described in Section 3.2. The conversion from SAC to IJAC puts the intensity-based ventilation into the same units as TJAC and make it easier for direct comparison. Since the intensity-based ventilation metrics can be converted from one to another, the reproducibility results

of the SAC and IJAC in this chapter are representative of all ventilation metrics using the intensity-based strategy.

Due to the overlay of pulmonary parenchyma mask [-999,-250] to the ventilation computation, not all lung locations are allocated a ventilation value. Combined with this non-linearity and existence of zero values, these restrictions limit the application of ratio or difference metric for direct validation of regional ventilation. We introduce the gamma index to address the problem of mismatch by considering neighborhood voxels in a certain distance. From Figure 3.10 we can see for both sheep and human subjects, the gamma pass percentage of IJAC is always lower than that of TJAC for different criterion Δp_0. Take the human subjects in Figure 3.10 (b) for example, to achieve as good pass percentage as TJAC at $\Delta p_0 = 0.1$, the criterion Δp_0 for IJAC has to be relaxed to as high as 0.3, indicating the worse reproducibility of IJAC. When Δp_0 changes from zero to infinitely large, the gap between IJAC and TJAC gamma pass percentage first increases and then decreases. The Δp_0 that corresponds with the maximum gap may represent the fluctuation percentage of intensity-based ventilation caused by CT HU noise. Another noteworthy phenomenon can be found in Figure 3.10 (a) and (b) that when Δp_0 is extremely small, e.g. less than 0.02, the gamma pass percentage of IJAC is higher than that of TJAC. This might be explained that in the case of when Δp_0 is small, in fact the fluctuation in IJAC map helps the gamma index algorithm find similar ventilation values in the neighborhood in the other map, if we imagine scan one and two ventilation maps as two distributions of values with slightly biased centers.

Figure 3.11 show JAC_{T1} ventilation map and scatter plots after different levels of local averaging on original CT images involved in IJAC computation. Compared to Figure 3.6, the IJAC map appears more smooth with heavier smoothing. However, the pattern of scatter plots does not change much except noise is suppressed partly with increased smoothness. As shown in Figure 3.12, the gamma pass percentage and correlation coefficient of IJAC did increase gradually with smoothing, but still much lower than the parameters of TJAC even with extremely heavy smoothness like kernel size $15 \times 15 \times 15$. When increasing the smoothing radius from 1 to 7 voxels, the pass rate and correlation coefficient of intensity-based ventilation measurements increased modestly, i.e. only 25% of the difference between them and the transformation-based results. Moreover, increased filtering, may cause that small, but important, variations in regional ventilation are lost by the filtering operation.

3.6 Summary

In this chapter we examined the reproducibility of two intensity-based ventilation metrics as a estimate of lung function and compared them with a transformation-based measure of ventilation. The transformation-based ventilation maps show better reproducibility than the intensity-based maps, especially in human subjects, when comparing the correlation coefficients and the gamma index. Reproducibility was also found to depend on changes in respiratory effort; all techniques were better when normalization for changes in tidal volume were applied to images from mechanically ventilated sheep compared to spontaneously-breathing human subjects. Nevertheless, intensity-based techniques applied to mechanically ventilated sheep were less repro-

ducible than the transformation-based applied to spontaneously-breathing humans, suggesting the method used to determine ventilation maps is important. We have developed an analytical model of how CT image noise affects the intensity-based ventilation. Pre-filtering of the CT images may help improve the reproducibility of the intensity-based ventilation measurements, but even with filtering the reproducibility of the intensity-based ventilation measurements are not as good as that of transformation-based ventilation measurements. When increasing the smoothing radius from 1 to 7 voxels, the pass rate and correlation coefficient of intensity-based ventilation measurements increased modestly, i.e. only 25% of the difference between them and the transformation-based results. The pass rate of gamma index, which is specially designed for validation of intensity-based ventilation, and other statistical parameters show transformation-based Jacobian is more reproducible than intensity-based Jacobian. The superior reproducibility of the transformation-based technique appears to allow smaller changes in ventilation to be measured; a 10% change in ventilation was observed between measures of ventilation derived from repeat scans $<$ 10% of the voxels, compared to $\sim$ 30% of the voxels when intensity-based techniques are used.

CHAPTER 4

RESPIRATORY EFFORT CORRECTION STRATEGIES TO IMPROVE THE REPRODUCIBILITY OF LUNG EXPANSION MEASUREMENT

This chapter is based on the following paper:

1. K. Du, J. M. Reinhardt, G. E. Christensen, K. Ding, and J. E. Bayouth: Respiratory Effort Correction Strategies to Improve the Reproducibility of Lung Expansion Measurement. In submission to Medical Physics, 2013

4.1 Introduction

Regional pulmonary function, which measures the local lung volume change, can provide valuable physiological and pathological information about lung. One method to estimate regional pulmonary function has been developed using four dimensional computed tomography (4DCT) and image registration. Since 4DCT has become a routine examination for lung cancer radiation therapy (RT) treatment planning, generating high resolution ventilation map adds no extra radiation dose to the patient. With image registration between CT images reconstructed at specific phases of the breathing cycle, the deformation field can be used to assess the regional pulmonary function. Several groups have developed this approach from different aspects. Reinhardt et al. [11] directly calculated the determinant of the deformation gradient tensor and used the Jacobian metric to analyze regional ventilation. Simon [12] and Guerrero et al. [13] proposed density-based ventilation calculation with the deformation field and its relationship with air fraction change. Castillo et al. [14]

demonstrated analytic and geometric Jacobian are mathematically equivalent, and both Jacobian-based and density-based ventilation are highly correlated with clinically acquired SPECT ventilation. Longitudinal radiation-induced pulmonary function change throughout RT was investigated by several groups. Ding et al. [15] compared regional ventilation before and after RT. Yaremko et al. [7] and Yamamoto et al. [89] identified high ventilated lung regions as avoidance structures in intensity modulated radiation therapy (IMRT) planning. Zhong et al. [90] presented a 4DCT-based regional compliance method for evaluation of radiation-induced lung damage. Vinogradskiy et al. [91] used ventilation maps calculated from weekly 4DCT data to study ventilation change throughout radiation therapy.

The variability in pulmonary function measurement must be accounted for when being used to identify underlying radiation-induced changes. Several groups have investigated the reproducibility of pulmonary function measurement. In our previous work, we investigated the reproducibility of transformation-based [87] (correlation coefficient 0.81±0.10) and intensity-based [88] (correlation coefficient 0.45±0.14) measures of lung tissue expansion in two repeat prior-RT 4DCT acquisitions, and found the reproducibility of 4DCT ventilation imaging would be deteriorated by respiratory effort variation. Similarly, Yamamoto et al. [86] investigated the reproducibility of lung ventilation over two different time frames and reported moderate voxel-based correlation between two ventilation images (Spearman rank correlation 0.50±0.15). However, cross-scan respiratory effort variations were not compensated in previous reproducibility studies.

Uncertainty in pulmonary function measurement can be caused by many factors including subject's irregular breathing patterns and change of tidal volume in spontaneous respiration, the imaging protocol, and choice of the ventilation metric [86, 87, 88]. Since the local lung expansion is dependent on the transformation from the EE (end of expiration) to the EI (end of inspiration) image, it will be affected by the lung volumes at which these two images are acquired. Therefore the respiratory effort (e.g., amplitude, frequency, switching between abdominal and thoracic breathing, etc.) may play a critical role in reproducibility assessment. In our previous study [87, 88], all subjects are coached and trained to ensure steady, reproducible breathing patterns during the 4DCT, and audible respiratory timing cues are used to help guide the subject during image acquisition [94]. However, even with the training and instrumentation, variations in breathing rate and tidal volume are likely to occur which may reduce the reproducibility of the pulmonary function measurements.

The effectiveness of pulmonary function measures increases as the uncertainty in the measurement is reduced. In this study we analyze a pair of 4DCT images obtained prior to RT, which should ideally yield identical pulmonary function maps. Variations in this measure will have an impact when being used as either input information into the radiation therapy treatment planning process, or for longitudinal study of pulmonary function (e.g., following RT). Respiratory effort difference may reduce reproducibility and therefore must be compensated for to be used in the two applications. First, normalization schemes on respiratory effort will help establish the post-intervention assessment of radiation-induced pulmonary function change.

Second, another potential use of the 4DCT-based ventilation is RT treatment plan optimization [7, 89] using ventilation avoidance maps, to avoid regions that have higher ventilation capacity or are more sensitive to radiation dose [114]. To be included into the RT planning system as a functional avoidance map, the ventilation map also needs to be normalized to correct for the difference in respiratory effort.

Several methods have been proposed to normalize the respiratory effort difference. Guerrero et al. [47, 7, 14, 91] converted ventilation images to percentile images as part of their normalization process to reduce the sensitivity to the maximum ventilation value on a particular image. However, the percentile image merely computes the rank of values rather than normalize the breathing effort difference. Vinogradskiy et al. [91] used another normalizing method proposed by Seppenwoolde et al. [115]. They defined a normalization factor calculated from well-ventilated low-dose regions and applied it to the entire image. Similarly, Zhang et al. [116] corrected SPECT scans for effort differences with a global scaling factor derived from a region of interest in the uninvolved lobe. They are both global normalization using one scaling factor applied to the entire image. The global normalization approach is based on the assumption and/or approximation that the lung expansion rate is spatially uniform. If the assumption is not true, the global normalization method will arbitrarily overnormalize or undernormalize regional ventilation values.

One of the advantages of 4DCT data for this purpose is that it consists series of CT images resolved into different phases of the breathing cycle [117, 118]. The 4D nature of the data implies that breathing effort difference can be corrected by

choosing phase images with equivalent/similar lung volume or tidal volume, rather than merely registering EE and EI. In this chapter we propose two strategies to select phase images, the equivalent tidal volume (ETV) method and the equivalent lung volume (ELV) method. These two approaches differ from other normalization methods in that they select independent respiratory phases to compute pulmonary function, rather than modify the computed ventilation values directly. In this study we quantify impact of global normalization on 4DCT from subjects and compare and determine which method (if any) best improves the reproducibility of pulmonary function measurement.

4.2 Material and methods

4.2.1 Patients selection

All the patients for this study were chosen from a protocol that was approved by the University of Iowa Institutional Review Board. Under the protocol, the patients underwent two 4DCT scans before radiation therapy for lung cancer. All scans were acquired in supine position on a Siemens Biograph 40-slice CT scanner operating in helical mode, using a pitch of 0.1, 120 kVp, 700 mAs, 1.2 mm beam collimator, 2 mm slice thickness, 0.5 mm slice increment, with a 500 msec tube rotation speed using 180 degrees to reconstruct an image producing a temporal resolution of 250 msec [119]. Anzai AZ-773V system with a strain gauge belt as the pressure sensor was used to acquire the surrogate signal of respiratory motion. To maintain a constant breathing rate, prior to imaging, patients were trained by a biofeedback system (RESP@RATE, Intercure Ltd., Lod Israel). Audible respiratory timing cues

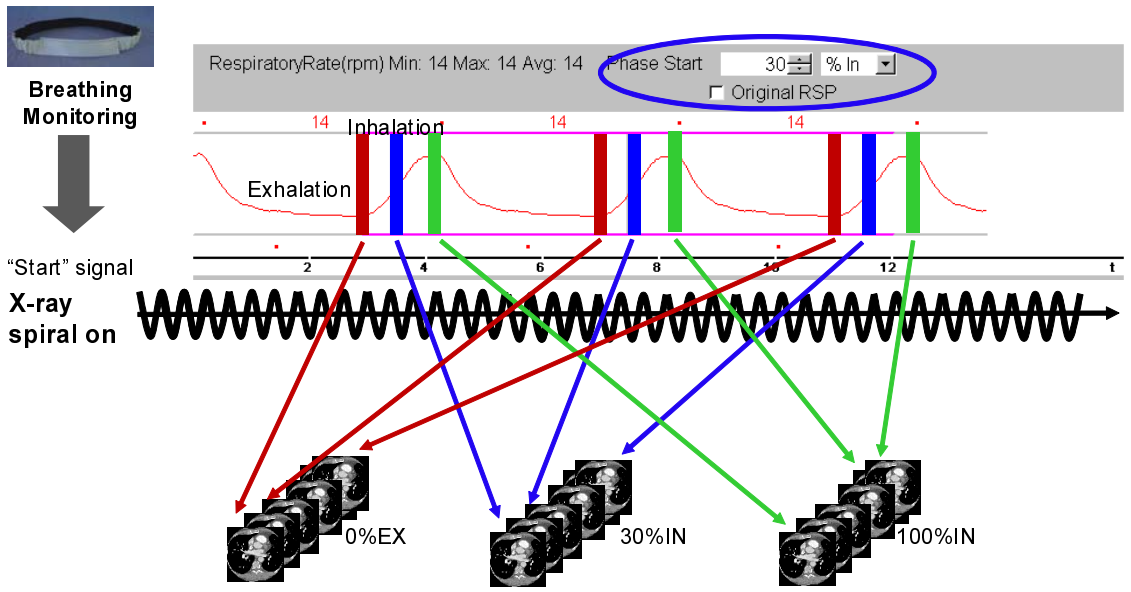

Figure 4.1. Retrospective reconstruction of 3D volumes based on respiratory phase and breathing amplitude.

were used to pace respiration during imaging [94]. Two prior-RT 4DCT scans were acquired for each subject, with a short time between scans and the same imaging parameters [87]. The subjects left the scanner table between scans.

As shown in Figure 4.1, after continuous spiral acquisition, the 4DCT scanner used retrospective respiratory gating to reconstruct 3D CT volumes at any user specified phase. Using the breathing monitoring curve as the reference, exact retrospective 3D volumes can be reconstructed from the 4D data based on respiratory phase and breathing amplitude. For each scan ten 3D CT images were produced, one at the end-expiration (EE, also denoted as 0%EX or 0%IN), four during inhalation in increments of 20% inspiration (20%IN, 40%IN, 60%IN, 80%IN), one at the end-inspiration (EI, also denoted as 100%IN), and four during exhalation in increments of 20% expiration (80%EX, 60%EX, 40%EX, 20%EX) in the scanner nomenclature [96]. Additional

phases could be reconstructed at different amplitudes if needed. The audio-coaching on patient respiration and the advantage of helical mode to allow manual selection of projection data could reduce and minimize the common artifacts in 4DCT [96]. Before image registration, all images were examined for evidence of severe breathing artifacts or other problems which may be caused during acquisition and reconstruction. 24 patients that needs correction for respiratory effort difference were chosen in this study.

4.2.2 Calculation of ventilation maps

The process of calculating ventilation maps with 4DCT and image registration was described in detail in our previous work [87]. First, prior to image registration all images were resampled to proper size and resolution. The Pulmonary Workstation 2.0 software (VIDA Diagnostics, Inc., Iowa City, IA) helped delineating the lung voxels in CT images. All of the lung segmentations were examined and manually modified if necessary. The lung segmentation was used to limit the spatial domain of image registration, subsequent ventilation calculation, and statistics analysis. The lung volume was calculated by multiplying the number of voxels with the volume of each voxel. Table 4.1 in Section 4.3.2 lists the lung volume of all inspiratory phases for three example subjects.

Two separate 4DCT scans (denoted as scan one and two) were acquired prior to RT with a short time interval for each subject. Ventilation maps were computed independently in the two scans and then compared in the same coordinate to determine the reproducibility of lung ventilation measurements. For each scan, ten CT volumes

were reconstructed including five inspiration phases and five expiration phases. Two volumes during inspiration can be selected to be registered by deformable image registration to produce a ventilation map. For ETV and ELV effort correction strategies, in addition to registration between the peak exhalation EE and the peak inhalation EI in each scan [87], intermediate breathing phases during inspiration were picked and registered, according to either equivalent tidal volume or equivalent lung volume to offset the breath effort difference in two scans.

A tissue volume preserving nonrigid algorithm was used for image registration [97, 109, 87]. In a multi-resolution optimization framework, the algorithm registers 3D CT images by minimizing the sum of squared tissue volume difference (SSTVD) [63] and a weighted laplacian regularization constraint in a cubic B-spline transformation model. The SSTVD similarity term was specially designed for lung image registration to compensate for the expected change in CT intensity due to inspired or expired air during respiration [63]. Subvoxel accuracy of the image registration algorithm has been reported in previous work of Du et al. [109, 120, 87], Cao et al. [97, 98] and Murphy et al. [93].

A displacement field that links corresponding lung voxels in two images is produced after image registration. The Jacobian determinant of the displacement field characterizes the local lung volume change and is used as the ventilation metric in this study. The Jacobian is given by Equation 2.5 as presented in Chapter 2, where $(h_1(\mathbf{x}), h_2(\mathbf{x}), h_3(\mathbf{x}))$ represents vectors in three dimensions of the deformation field at location $\mathbf{x}$. Encoded by colors, the Jacobian map will show regional ventila-

tion throughout the lung. In the Lagrangian reference frame, Jacobian greater than one represents local tissue expansion, Jacobian less than one represents local tissue contraction, and Jacobian equals to one means no expansion or contraction.

If we use T1 and T2 to denote the registration transformations in scan one and two, the two scans would produce Jacobian maps JAC_{T1} and JAC_{T2}. The computed Jacobian map was always defined at EE, or defined at the breathing phase with smaller lung volume in ELV. Since scan one and two are independent 4DCT acquisitions, we need to put the two Jacobian maps under one coordinate system for comparison. The target image of the image registration in scan one was used as the reference coordinate system. Therefore one additional registration needs to be made from scan two target image to scan one target image, resulting in transformation T0. When analyzing the reproducibility without effort correction or with ETV, 0%IN (EE) is used as the coordinate. However, in ELV analysis, the target image in scan one could be an intermediate phase. For instance, if we use 20%IN and 80%IN in scan one, and 40%IN and 100%IN in scan two, then the registration between scan two 40%IN and scan one 20%IN will be performed to build transformation T0. With the transformation T0, JAC_{T2} is transformed to the same coordinate of JAC_{T1}, called $JAC_{T2} \circ T0$. The Jacobian ratio map JAC_{RATIO}, defined in the same coordinate system as JAC_{T1}, is a voxel-by-voxel ratio map of JAC_{T1} and $JAC_{T2} \circ T0$ and can be used to assess reproducibility.

4.2.3 Respiratory effort correction strategies

When comparing measures of ventilation acquired from different studies, measured values may differ due to changes in respiratory effort. This section describes the most commonly used normalization strategy (global normalization) and two novel strategies proposed in this study.

4.2.3.1 Global normalization

By definition, the Jacobian reflects the ratio of volumes before and after deformation in a specified region. Since the average Jacobian is strongly correlated with the global volume change in the lung [87], the lung volumes can be used to calculate a global linear normalization factor to compensate for lung volume differences between scans one and two.

Suppose I_a and I_b denote the fixed and moving image respectively in image registration. Jacobian map J_1 is calculated from the displacement field between two images I_{1a} and I_{1b}, and Jacobian map J_2 is calculated from the displacement field between two images I_{2a} and I_{2b}. We use V_i to denote the lung volume of image I_i. Then the Jacobian map J_2 can be globally normalized to match with the global inflation level of J_1.

$$J_2^{\text{norm}} = J_2 \times \frac{\frac{V_{1b}}{V_{1a}}}{\frac{V_{2b}}{V_{2a}}} \tag{4.1}$$

where J_2^{norm} is J_2 after global normalization derived from the ratio of lung volumes in scan 1, normalized by the ratio of lung volumes in scan 2.

The global scaling normalization uses one factor applied to the entire image, commonly based on a ratio of ventilation or perfusion measures acquired from an

identical region in the two scans that is assumed to be uninvolved. The global scaling approach is based on the assumption and/or approximation that the lung expansion rate is spatially uniform. Alternatively, these would not be valid if the expansion rate in the apex is not proportional to expansion in the base for all intermediate tidal volumes between EE and EI.

4.2.3.2 ETV and ELV

The basic approach used in global normalization is to compute ventilation from images with known differences in respiratory effort and to scale those values. We propose careful selection of the input data, rather than performing post-processing corrections. This is accomplished by selecting CT images with similar lung volumes or tidal volumes, allowing calculation of the Jacobian under more similar conditions. This technique exploits one of the advantages of 4DCT images, which provides CT images with many different lung volumes. Other than EE and EI images, additional respiratory phases were selected to compute pulmonary function and evaluate reproducibility. This strategy was applied to repeat 4DCT scans of the 24 subjects as described below.

Figure 4.2 shows the schematic of two respiratory effort correction strategies. The red line is the baseline scan, while the orange line is the followup scan. Scan one is used as the baseline scan. Figure 4.2 (a) is the ETV method that uses a pair of images selected from the followup 4DCT scan that produces a tidal volume equivalent to that of the baseline scan. Figure 4.2 (b) is the ELV method that uses a pair of 3D CT images selected from the followup scan that maximizes the volume

difference between images and has corresponding images at the same lung volumes in the baseline 4DCT scan. We will compare these methods against one another, with global normalization, and before correction to determine which (if any) better improves reproducibility of pulmonary function measurement.

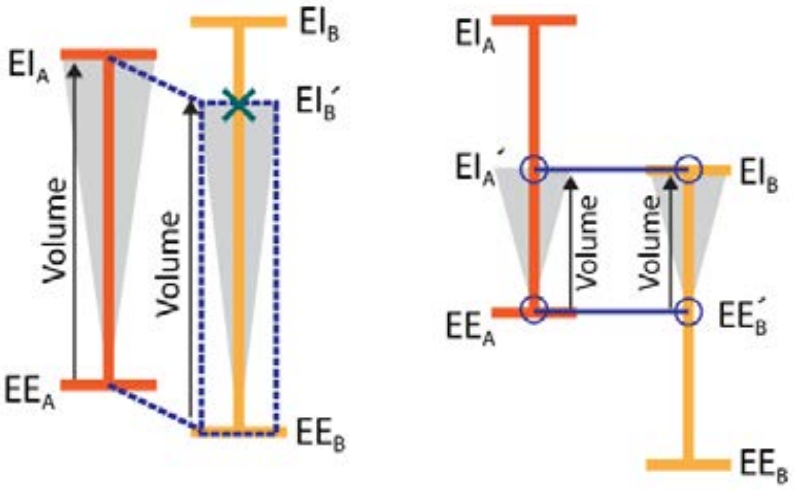

(a) (b)

Figure 4.2. Schematic of respiratory effort correction strategies. The red line is the baseline, while the orange line is the followup scan. (a) ETV and (b) ELV.

To further test the effectiveness of the ETV method, an experiment is designed by testing pairs of images with other possible tidal volumes in the followup scan and then comparing them with the end-to-end ventilation map from the base line scan. Figure 4.3 illustrates the experiment design. Suppose scan one has a smaller tidal volume (less respiratory effort) than scan two, with the ETV method we will attempt to find an intermediate inspiratory phase from scan two that produces equivalent or best matching tidal volume to that of scan one. Suppose scan two 60%IN has the

best matching tidal volume to that of scan one 100%IN. In this example, other than 60%IN, we will also test using 20%IN, 40%IN, 80%IN and using 100%IN (means no correction) from scan two to study how the reproducibility parameters change with different scales of tidal volume disagreement across scans. In this experiment, the scan with less effort is chosen as the baseline scan, for subject H-9, scan two 100%IN is compared to all scan one phases.

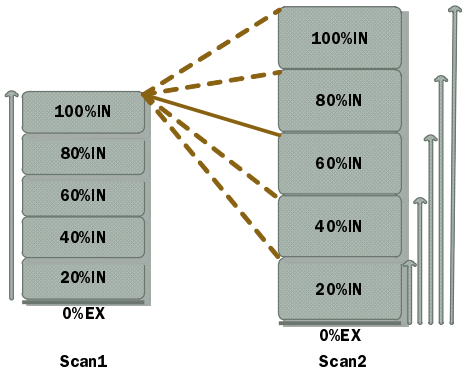

Figure 4.3. Diagram showing the experiment to test the effectiveness of ETV. Other than the best ETV pairs in scan one and two, pairs with different tidal volumes are assessed.

4.2.4 Characterizing heterogeneity of lung expansion

One 4DCT scan of subject H-8 was chosen to demonstrate the heterogeneity in lung expansion rate, as shown in Figure 4.5 and Figure 4.6. If the lung expansion rate is spatially uniform, the Jacobian map from 40%IN to 60%IN and the Jacobian map from 60%IN to 80%IN should be identical or be proportional to each other everywhere, and their histograms should have the same shape. The results for this

experiment are shown in (a) and (b) of Figure 4.5 and Figure 4.6.

Additional experiment is performed to determine heterogenous spatial pattern of ventilation rate on the lobar level. The same scan as in (a) and (b) of Figure 4.5 and Figure 4.6 was used to plot how the mean Jacobian (calculated from EE to each inspiratory phase) in each lobe changes with different tidal volumes (results shown in in (c) of Figure 4.5 and Figure 4.6). Referring to the right lower (RL) lobe, the relative expansion rate of the other four lobes were studied (result shown in in Figure 4.5 (d) and Figure 4.6 (d)). The hypothesis is if the lung expansion is spatially homogenous, the ventilation rate in RL should be proportional to the other lobes. Global normalization would be demonstrated to be inapplicable if the ventilation rate in one lobe is not proportional to the other lobes when tidal volume is greater than certain number. However, we can see with increasing lung expansion level, the other four lobes do not expand at the same rate as RL lobe, and even different expansion rates to each other.

If calculated from registered EE and EI images, the Jacobian means cumulated lung expansion in the entire inspiration process. However, regional tissue expansion rate varies both spatially and temporally. Introducing intermediate inspiration phases brings several additional time sampling of lung expansion pattern. With the hypothesis of homogeneous lung expansion rate, which is the theoretical basis of global normalization, the only difference for each time sampling of the lung expansion should be the magnitude, i.e. the Jacobian maps will become identical to each other after scaling by certain constant. Hence, the heterogeneity of lung expansion can be quan-

tified by comparing the global normalized Jacobian map from EE to each specific phase with the Jacobian maps from EE and EI.

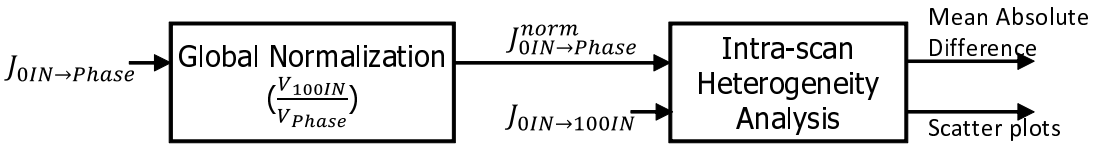

Figure 4.4. Flowchart of the intra-scan global normalization and intra-scan lung expansion heterogeneity analysis. The Jacobian map from EE to each specific phase (phase $\in$ {20%IN, 40%IN, 60%IN, 80%IN}) is globally normalized to the inflation level of full inspiration and then compared with the Jacobian map from EE to EI.

Figure 4.4 shows a flowchart of the intra-scan lung expansion heterogeneity analysis. Within a 4DCT scan, each Jacobian map from EE to a specific inspiration phase was scaled using global normalization to the same inflation level of Jacobian map from EE to EI, with a factor calculated from lung volumes. Since CT volumes were reconstructed using the retrospective respiratory gating technology from multiple breathing cycles according to the amplitude of respiratory trace (Figure 4.1), the term of 0%IN volume is equivalent to the term of 0%EX volume when indicating the beginning phase of inspiration. The equation 4.2 shows the process of the intra-scan global normalization that normalizes Jacobian maps from EE to an inspiration phase to the Jacobian of full inspiration:

$$J^{\text{norm}}_{\text{0IN}\rightarrow\text{Phase}} = J_{\text{0IN}\rightarrow\text{Phase}} \times \text{f}(\text{V}_{\text{Phase}}) = J_{\text{0IN}\rightarrow\text{Phase}} \times \frac{\frac{V_{\text{100IN}}}{V_{\text{0IN}}}}{\frac{V_{\text{Phase}}}{V_{\text{0IN}}}} = J_{\text{0IN}\rightarrow\text{Phase}} \times \frac{V_{\text{100IN}}}{V_{\text{Phase}}}, \quad (4.2)$$

where phase $\in$ {20%IN, 40%IN, 60%IN, 80%IN}, $\text{f}(\text{V}_{\text{Phase}})$ is the global normalization

factor, and $V_{0\text{IN}}$, V_{Phase}, and $V_{100\text{IN}}$ are lung volumes. The mean absolute difference is calculated for all lung voxels between the Jacobian map from EE to EI and the global normalized Jacobian map from EE to each specific phase by equation 4.3:

$$\text{Mean Absolute Difference} = \frac{\sum_{n=1}^{N} |J_{0\text{IN}\to 100}(n) - J^{\text{norm}}_{0\text{IN}\to\text{Phase}}(n)|}{N}, \tag{4.3}$$

where $J^{\text{norm}}_{0\text{IN}\to\text{Phase}}$ is Jacobian map after intra-scan global normalization, n represents each lung voxel, and N is the total number of lung voxels.

Both scans from all subjects were processed for the heterogeneity analysis. To study whether the heterogeneity increases with longer interval, we also investigate the relationship between heterogeneity and the inverse of the scaling factor, which represents the fraction of full inspiration for a specific intermediate phase compared to EI.

4.2.5 Outcome metrics and statistical analysis

In this study four outcome metrics were used to evaluate the reproducibility: 1) mean of $\text{JAC}_{\text{RATIO}}$, which should be closer to one if reproducibility improves. 2) voxel-by-voxel coefficient of variation (CV) of $\text{JAC}_{\text{RATIO}}$, where smaller CV would suggest smaller regional difference between JAC_{T1} and $\text{JAC}_{\text{T2}} \circ \text{T0}$ and thus indicate improved reproducibility. Since global normalization simply scales the whole ventilation map with a factor, there is no change in CV after global normalization. 3) mean square error (MSE) of JAC_{T1} and $\text{JAC}_{\text{T2}} \circ \text{T0}$, where lower MSE indicates better reproducibility. 4) gamma pass rate. We have proposed in previous work [88, 120] a modified gamma index to compare two ventilation maps regionally and quantita-

tively. In addition to considering the ventilation difference, the gamma index adds a term to tolerate possible spacial misalignment. A voxel that passes gamma index evaluation implies that there is a matching voxel in the other ventilation map with less than the specified criterion for ventilation difference within a certain distance. The pass rate is computed by counting all passed voxels and then dividing by total number of pulmonary parenchyma voxels.

In all 24 subjects that were used in this study, ETV applies for 18 of them, and ELV applies for 21 of them. ELV is not suitable for some subjects that had significant shift of breathing baseline. For example, for subject H-7 the EE lung volume of scan two is almost as high as the EI lung volume of scan one (Figure 4.9). To the contrary, some subjects have intermediate phases applicable for ELV, but under ETV selection strategy no breathing phase is more optimal than the original EI phase before normalization. The four reproducibility outcome metrics were calculated and analyzed using subject-specific tidal volume difference across scans. All three effort correction strategies were applied and assessed for their improvement of reproducibility, compared to making no correction for respiratory effort differences between scans. Comparisons were performed between global and ETV, between global and ELV, and between ETV and ELV on entire cohort and the cohort that have tidal volume difference greater than 100 cc.

4.3 Results

4.3.1 Results: heterogeneity of lung expansion

Figure 4.5 and Figure 4.6 shows the heterogeneity in the spatiotemporal pattern of ventilation rate using scan two of subject H-8. Figure 4.5 (a) and Figure 4.6 (a) shows the coronal and sagittal colored panel of Jacobian in registration pairs 40%IN to 60%IN (lung volume from 3.63 L to 4.05 L) and 60%IN to 80%IN (lung volume from 4.05 L to 4.36 L). The regions that are highly ventilated during 60%IN to 80%IN do not simply scale proportionally during 40%IN to 60%IN, i.e, the pattern of ventilation changes. Their corresponding Jacobian histograms also present different patterns as seen in Figure 4(b), where far fewer voxels expand with a Jacobian value greater than 1.15 during the later stage of ventilation. (c) and (d) of Figure 4.5 and Figure 4.6 show the heterogenous tissue expansion rate for different lobes from EE to each respiratory phase. (c) of Figure 4.5 and Figure 4.6 shows the average Jacobian for the left upper (LU), left lower (LL), right upper (RU), right middle (RM), and right lower lobe (RL) along with the whole lung. As expected, greater ventilation is seen in the two lower lobes of the lung. (d) of Figure 4.5 and Figure 4.6 shows the ventilation in each lobe when normalized to the ventilation in the right lower lobe, consistent with conventional respiratory effort correction strategies. The lobar ventilation shows as high as 20% difference when the tidal volume is 0.8 L, and around 30% difference when the tidal volume is 1.2 L. These results demonstrates that the ventilation rate is not uniform throughout the lung, not even at the lobar level. The ventilation rate for the left lower lobe is similar to the right lower lobe, but the upper

and middle lobes show more heterogeneous air filling rates.

Figure 4.7 and Figure 4.8 show results of the intra-scan lung expansion heterogeneity analysis, which evaluates these differences at the voxel level. If ventilation is independent of spatiotemporal effects, ventilation patterns produced during the initial phases of inspiration could be scaled globally without deviation from the ventilation map determined at the end of inspiration. This intra-scan study approach allows the end of inspiration map to be used as ground truth. Figure 4.7 shows the original and the globally normalized Jacobian maps computed for this intra-scan experiment performed, for scan one and scan two of subject H-8. For this scan, all Jacobian maps were globally normalized to the inflation level of Jacobian from EE to EI. Since scan two had a greater respiratory effort than scan one for this subject, for comparison all the Jacobian maps of scan two were additionally globally normalized to the scale of Jacobian of full inspiration in scan one. We can see after global normalization there are still differences between the ventilation maps from different inflation levels. The global normalization did not consider the regional difference of the lung expansion rate. For example, when the Jacobian from EE to 20%IN in scan one was normalized to the full inspiration level of scan one, the magnitude of the ventilation changed but the distribution pattern did not change. For instance, some regions are going to expand with higher rates in next phases - they will be undernormalized by the global normalization, such as the dorsal lung; while some regions are going to expand with lower rates in next phases - they will be overnormalized by the global normalization, such as the ventral lung.

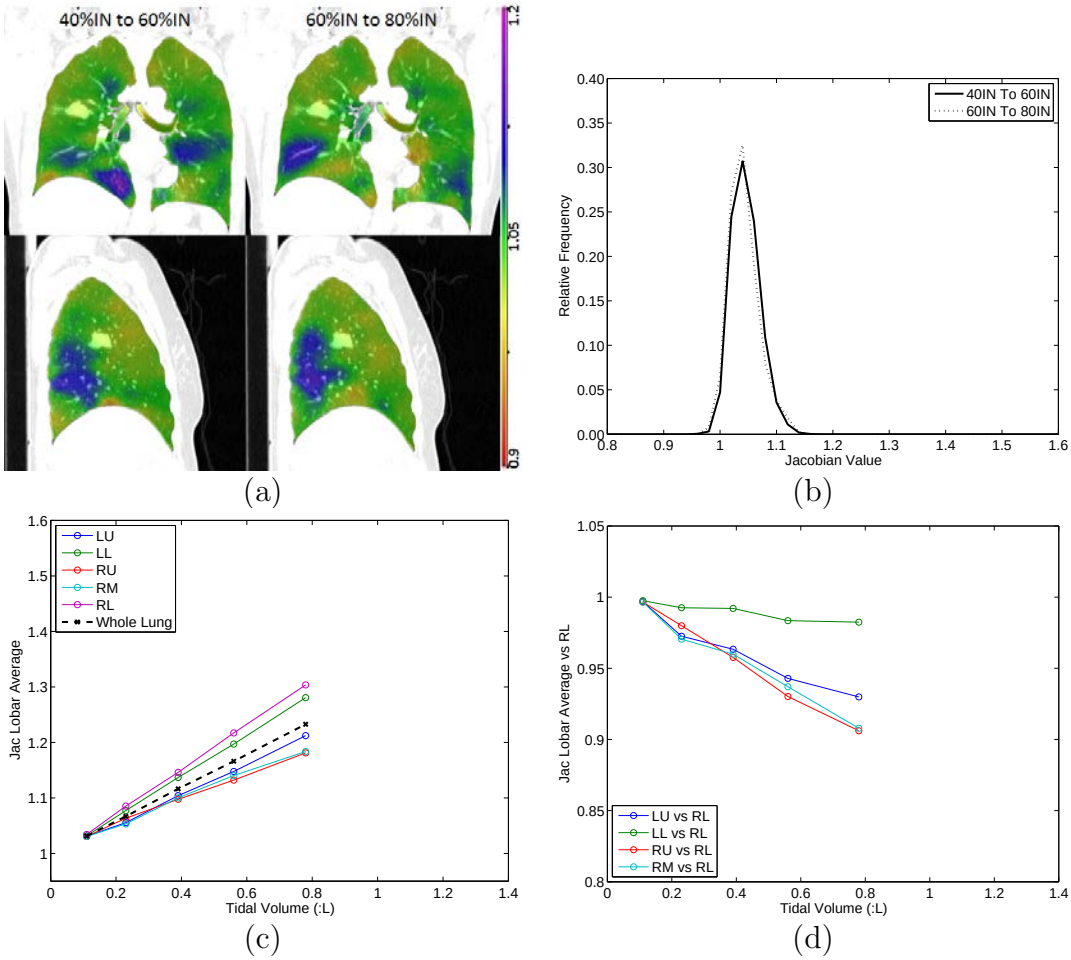

Figure 4.5. A Scan one of subject H-8 is used to show the heterogenous tissue expansion rate. (a) shows the coronal (top) and sagittal (bottom) view of Jacobian for registration pair 40%IN to 60%IN and 60%IN to 80%IN (left to right). The scale is both 0.9 to 1.2. (b) shows the corresponding histograms of the two Jacobian maps in (a). (c) shows the average tissue expansion from EE to each respiratory phase for each lobe and the whole lung. (d) shows the tissue expansion for lobes LU, LL, RU, RM, relative to lobe RL.

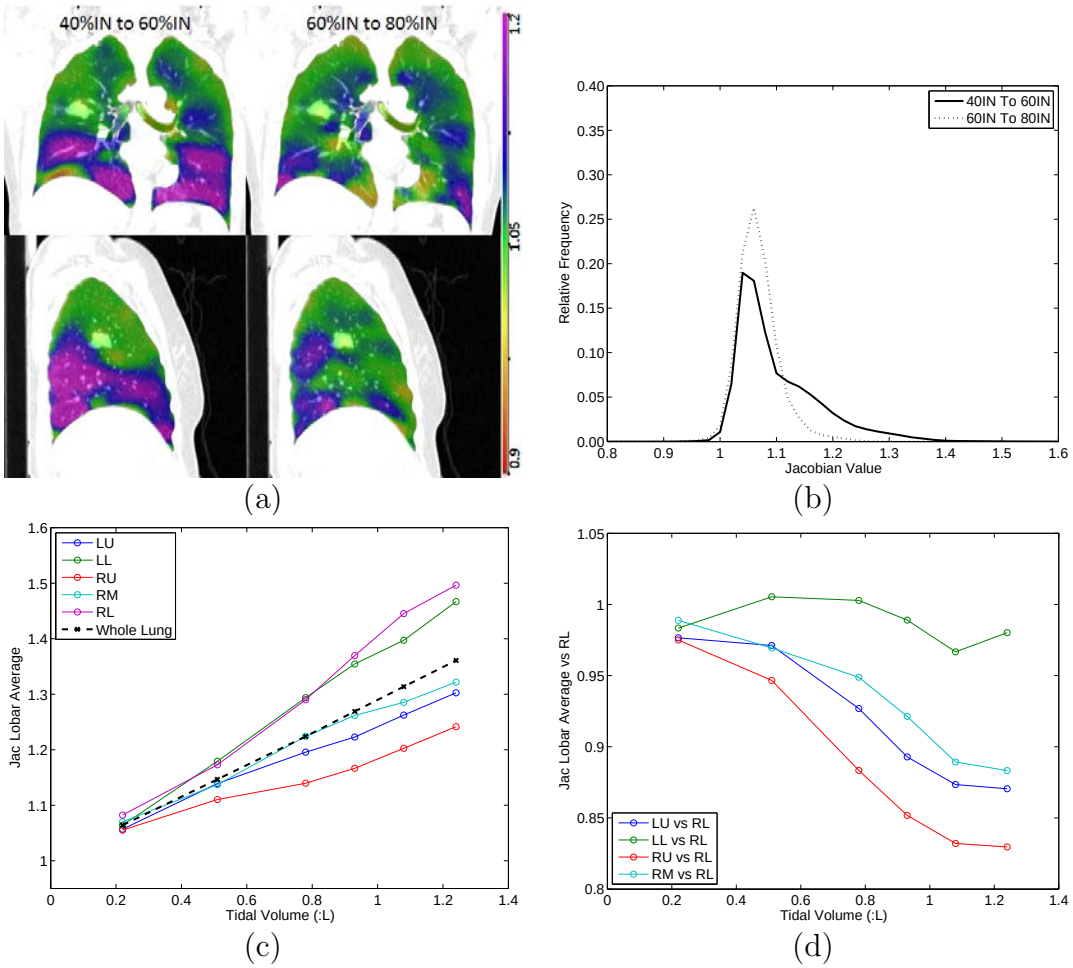

Figure 4.6. Scan two of subject H-8 is used to show the heterogenous tissue expansion rate. (a) shows the coronal (top) and sagittal (bottom) view of Jacobian for registration pair 40%IN to 60%IN and 60%IN to 80%IN (left to right). The scale is both 0.9 to 1.2. (b) shows the corresponding histograms of the two Jacobian maps in (a). (c) shows the average tissue expansion from EE to each respiratory phase for each lobe and the whole lung. (d) shows the tissue expansion for lobes LU, LL, RU, RM, relative to lobe RL.

Another observation worth mentioning is that the ventilation map of EE to 80%IN, compared to that of EE to 20%IN, is more similar to the ventilation map for full inspiration. It suggests the global normalization may be adequate when tidal volume difference is small. Figure 4.8 (a) and Figure 4.8 (b) show the scatter plots of how the ventilation difference and the associated global normalization error change with different fractions of full inspiration. The horizontal axis $\frac{V_{Phase}}{V_{100IN}}$ enables a normalized measure of fraction of full inspiration across different subjects. Figure 4.8 (a) shows the ventilation difference increases when the phase is further away from full inspiration ($R = 0.97$). In comparison, Figure 4.8 (b) shows quantitative heterogeneity results for scan one and scan one for all subjects, determined using equation 4.2. A linear correlation is found between global normalization error and the fraction of full inspiration (ratio of V_{Phase} and V_{100IN}, can be understood as a parameter for time interval). The vertical axis is the mean absolute difference in the globally normalized Jacobian maps. A linear relationship between lung expansion heterogeneity and the inflation level was observed with high correlation ($R = 0.79$). Figure 4.8 (b) shows the limitations of global normalization to address the complexity of respiratory effort normalization, which may require both a spatial and temporal component.

4.3.2 Results: phase selection in ETV and ELV

Figure 4.9 shows the lung volumes of two repeat scans for two sample subjects H-7 and H-8. The solid line represents scan one, and the dot line represents scan two. In Table 4.1 we list the lung volumes for three typical subjects H-7, H-8, and H-9. The unit of lung volume is in liters. Two extra phases 50%IN and 70%IN were

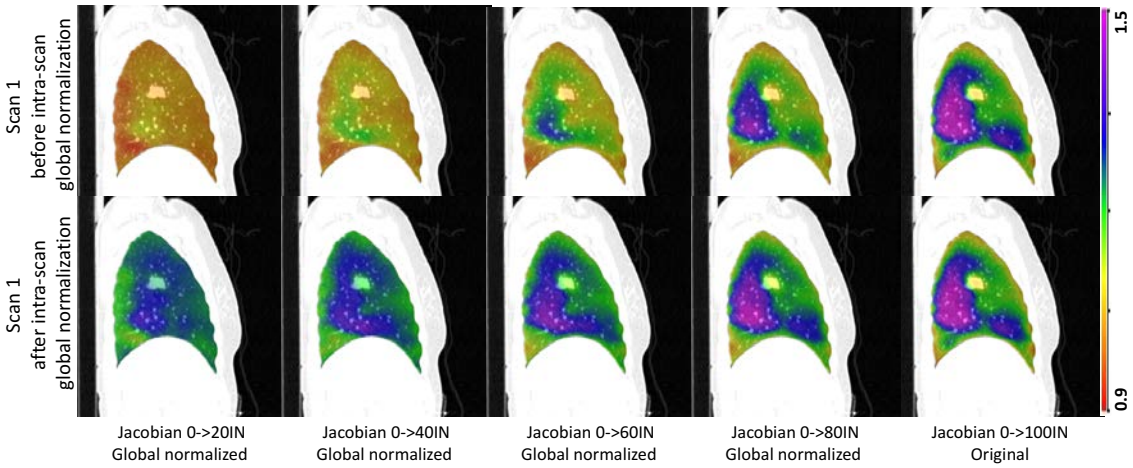

(a)

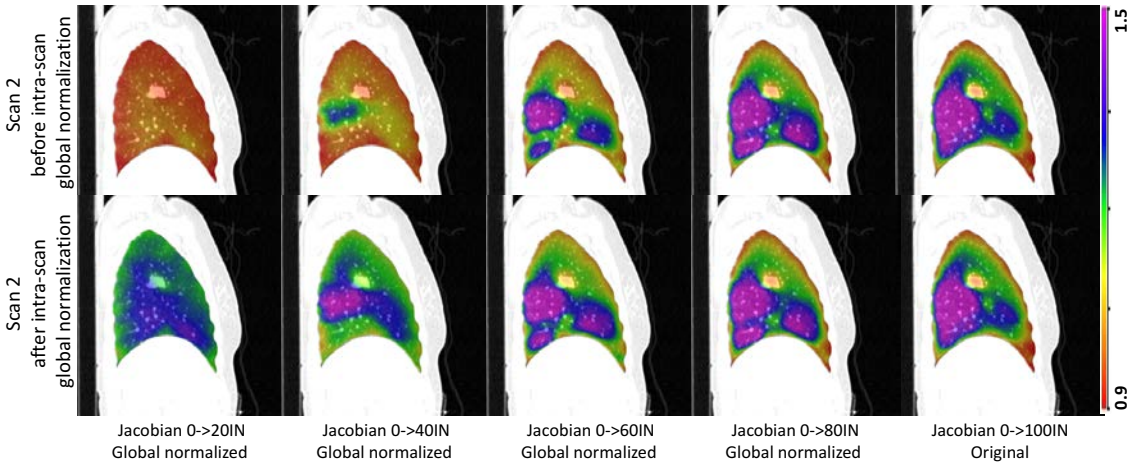

(b)

Figure 4.7. Jacobian maps for intra-scan lung expansion heterogeneity analysis after global normalization, for subject H-8. Since scan two had a greater respiratory effort than scan one for this subject, for comparison purpose all the Jacobian maps of scan two were further globally normalized to the scale of Jacobian of full inspiration in scan one. (a) Scan one, (b) scan two.

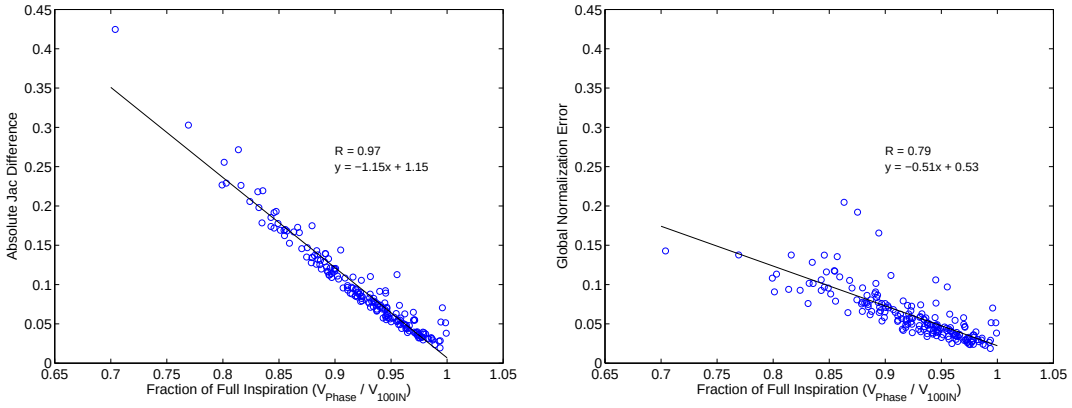

(a) (b)

Figure 4.8. Scatter plot of intra-scan lung expansion heterogeneity analysis after global normalization. (a) Absolute Jacobian difference before global normalization. (b) Global normalization error after global normalization.

reconstructed for scan two of subject H-8. The numbers in bold show the ETV effort correction, and the underlined numbers show the ELV effort correction. While we can perform both ETV and ELV correction for subjects H-8 and H-9, ELV cannot be applied on subject H-7 because the EE lung volume of scan two is almost as high as the EI lung volume of scan one. Similar significant shifting of the breathing baseline was found for another two subjects.

Figure 4.10 shows the change of mean and standard deviation of JAC_{RATIO} when different levels of breath effort in scan one and two are compared. This process is described in Figure 4.3 and Section 4.2.3.2. The horizontal axis is the difference of tidal volumes between EE to EI in the baseline scan and EE to intermediate phases in the followup scan. The vertical position of each solid spot represents the mean of JAC_{RATIO} maps. The whiskers and the numbers on top show the standard deviation of JAC_{RATIO}. As the tidal volume difference in two scans diminishes, the mean of

Table 4.1. Lung volumes in two repeat 4DCT scans for three example subjects.

	Scan	Vol.	0%IN	20%IN	40%IN	50%IN	60%IN	70%IN	80%IN	100%IN
H-7	1	Lung	5.26	5.39	5.53	-	5.60	-	5.64	5.72
		Tidal	0	0.13	0.27	-	0.34	-	0.38	**0.46**
	2	Lung	5.69	5.97	6.10	-	6.21	-	6.33	6.37
		Tidal	0	0.28	0.41	-	**0.52**	-	0.64	0.68
H-8	1	Lung	3.02	*3.13*	3.25	-	3.41	-	*3.57*	3.79
		Tidal	0	0.11	0.23	-	0.39	-	0.56	**0.78**
	2	Lung	*3.12*	3.34	*3.63*	3.90	4.05	4.20	4.36	4.35
		Tidal	0	0.22	0.51	**0.78**	0.93	1.08	1.24	1.23
H-9	1	Lung	3.65	*3.83*	3.98	-	4.13	-	*4.31*	4.50
		Tidal	0	0.18	0.33	-	**0.48**	-	0.66	0.85
	2	Lung	*3.81*	3.98	4.09	-	4.17	-	4.23	*4.33*
		Tidal	0	0.18	0.29	-	0.37	-	0.43	**0.52**

The lung volume in bold shows ETV, and the lung volume underlined shows ELV.

JAC_{RATIO} eventually gets closer to one (red dot line), and the standard deviation decreases indicating better reproducibility.

4.3.3 Results: all effort correction strategies

Figure 4.11 shows the sagittal view of colored JAC_{RATIO} maps before effort correction, after global normalization, after ETV, and after ELV for subject H-8. The color scale for the JAC_{RATIO} maps is the same 0.7 to 1.3. For this subject, ELV was found to have more reproducible regions than ETV and global normalization. Figure 4.12 shows the voxel-by-voxel scatter plots of JAC_{T1} and $JAC_{T2} \circ T0$ data, which were encoded with colored 2D kernel density estimates [87, 101], for one sample subject H-8 before and after the three effort corrections. Marginal histograms of JAC_{T1} and $JAC_{T2} \circ T0$ are plotted along the top and right side of the figures, ideally these histograms would be mirrored images of one another. By linear regression analysis, a best fit linear model (shown as the dash line) is calculated to represent the relationship between scan one and scan two ventilation. Line y=x is also plotted as the reference line; ideally the data would fall on the y=x regression line. The slope and y-intercept for each correction strategy is provided on the figure, showing the improved reproducibility of the different approaches.

Figure 4.13 (a) shows the histograms of JAC_{RATIO} of subject H-8 for before correction, after global normalization, after ETV correction, and after ELV correction. Since in the global normalization JAC_{RATIO} is simply scaled by a constant, its histogram shifts closer to one but the shape does not change. The ETV and ELV histograms become narrower and closer to one, indicating better agreement of the

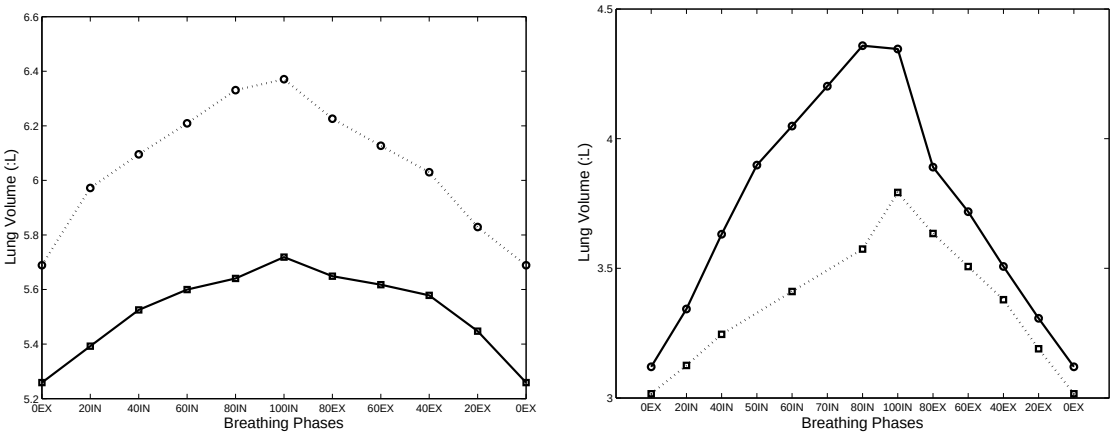

H-7 H-8

Figure 4.9. Lung volumes of 4DCT in two repeated scans for two sample subjects. Solid line is for scan one, and dot line is for scan two. Note the scale may be different for each subject.

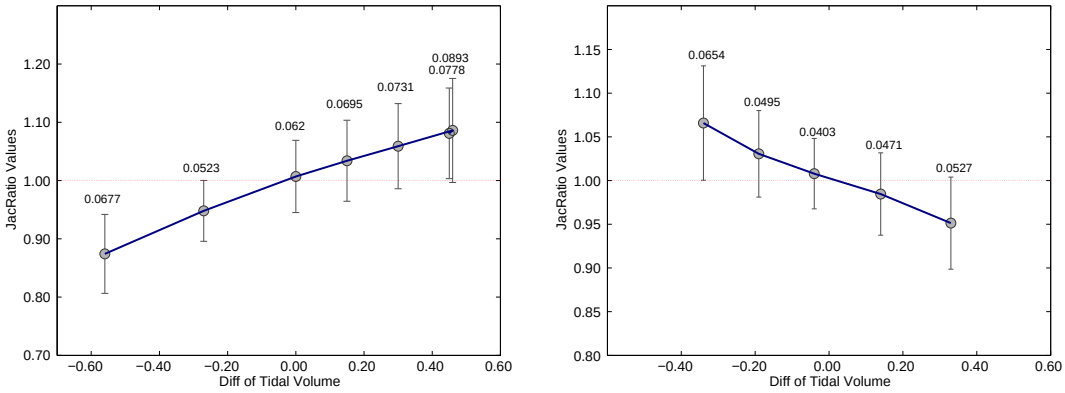

H-8 H-9

Figure 4.10. Change of mean and standard deviation of JAC_{RATIO} when the tidal volume in two scans eventually gets close. The fold line with solid spots show the change of mean of JAC_{RATIO}. The whiskers and the numbers on top show the standard deviation. Refer to Figure 4.3 for the experiment process.

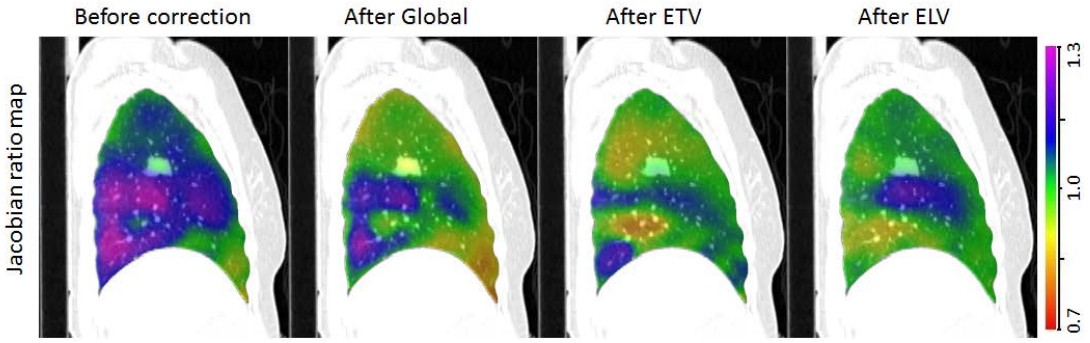

Figure 4.11. Sagittal view of JAC_{RATIO} before correction, after global normalization, after ETV, and after ELV effort correction for subject H-8. The color scale is shown on the right.

two ventilation maps. Figure 4.13 (b) shows the gamma pass rates with increasing gamma criterion for the same subject before correction, after global normalization, after ETV, and after ELV. We can see for this subject all three effort correction strategies improve reproducibility. Additionally, both ETV and ELV methods, especially ELV, result in better reproducibility than the global normalization when the ventilation difference criterion in gamma evaluation (delta p0) is below 10%.

Figure 4.14 shows the MSE and Gamma pass rate results for each effort correction strategy for all subjects. The results are provided as a function of the relationship between the tidal volume difference in two scans and the change of reproducibility after global normalization, after ETV and/or ELV for all subjects, with regard to MSE and gamma pass rate. The horizontal axis is tidal volume difference in liters. The improvement of reproducibility can be read from reduced MSE and increased gamma pass rate. It is observed that the improvement of reproducibility is particularly significant in case of greater tidal volume difference between scan one and two. We can also

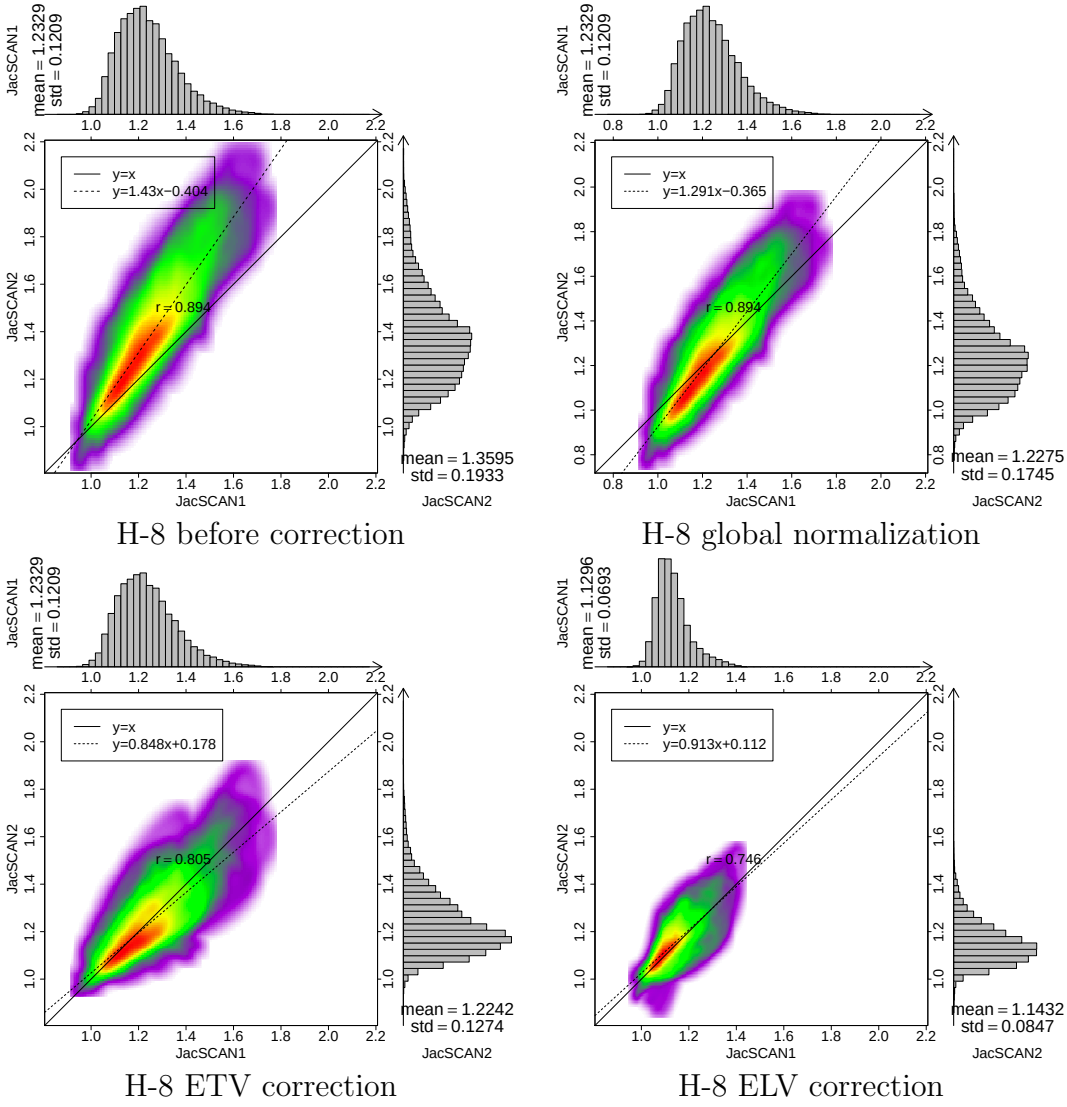

Figure 4.12. Colored density scatter plot and marginal histograms of two Jacobian maps for subjects H-8. Before effort correction, after global normalization, after ETV correction and after ELV correction, are shown respectively. Histograms and statistics are given along the top and right side of each plot.

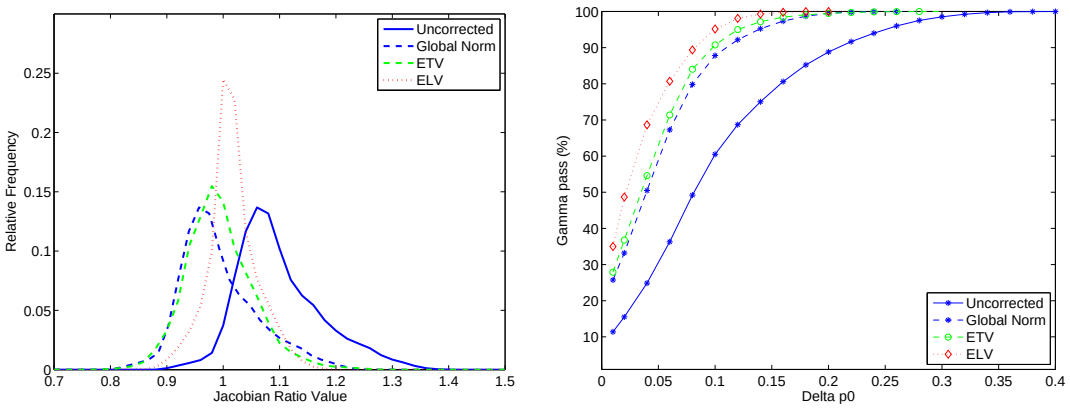

(a) (b)

Figure 4.13. Histograms of JAC_{RATIO} map and gamma pass rates for subject H-8 before effort correction, after global normalization, after ETV, and after ELV. The curves for before effort correction, after global normalization, after ETV, and after ELV are shown in solid blue, dashed blue, dashed green, and dotted red respectively. (a) Histograms of JAC_{RATIO} map. (b) gamma pass rates.

notice that if the tidal volume difference is small, the effect of global normalization is close to ETV and ELV, and for some subjects the normalization strategies may deteriorate the reproducibility. ELV gave better results as tidal volume difference increases. Figure 4.15 shows the linear correlation between tidal volume difference and the proportional tidal volume difference, which is tidal volume difference divided by the subject-specific average EE volume in two scans. The outlier subject shown in red had a super small lung with big tidal volume difference. The linear correlation indicates the tidal volume difference can be used to measure the effort difference across different subjects.

4.3.4 Results: Statistical analysis

Table 4.2 summarizes the mean, CV of JAC_{RATIO}, MSE, and gamma pass rate to evaluate reproducibility before effort correction, after global normalization, after

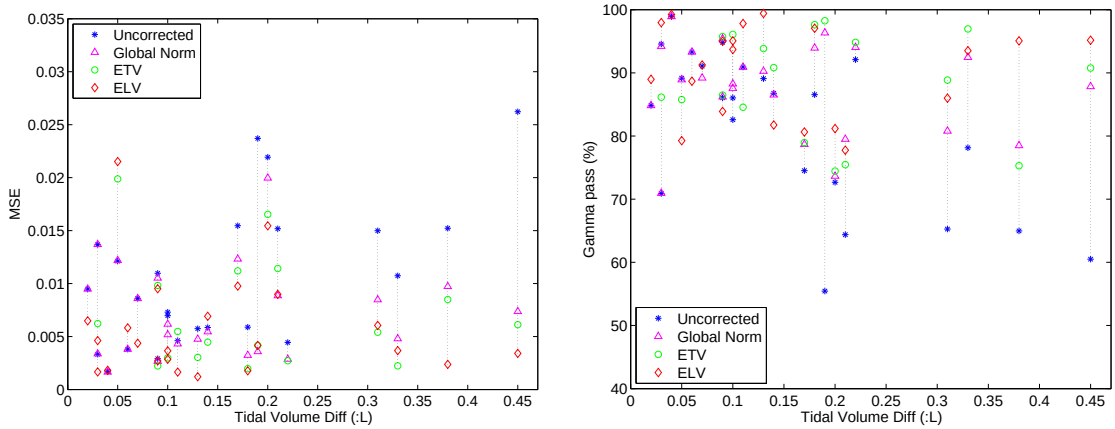

(a) (b)

Figure 4.14. Relationship between the tidal volume difference in two scans and the change of reproducibility after global normalization, after ETV and/or ELV, presented with reproducibility parameters as modified mean square error (MSE), and gamma pass rate between JAC_{T1} and $JAC_{T2} \circ T0$. The horizontal axis is tidal volume difference in liters. (a) MSE. (b) gamma pass rate.

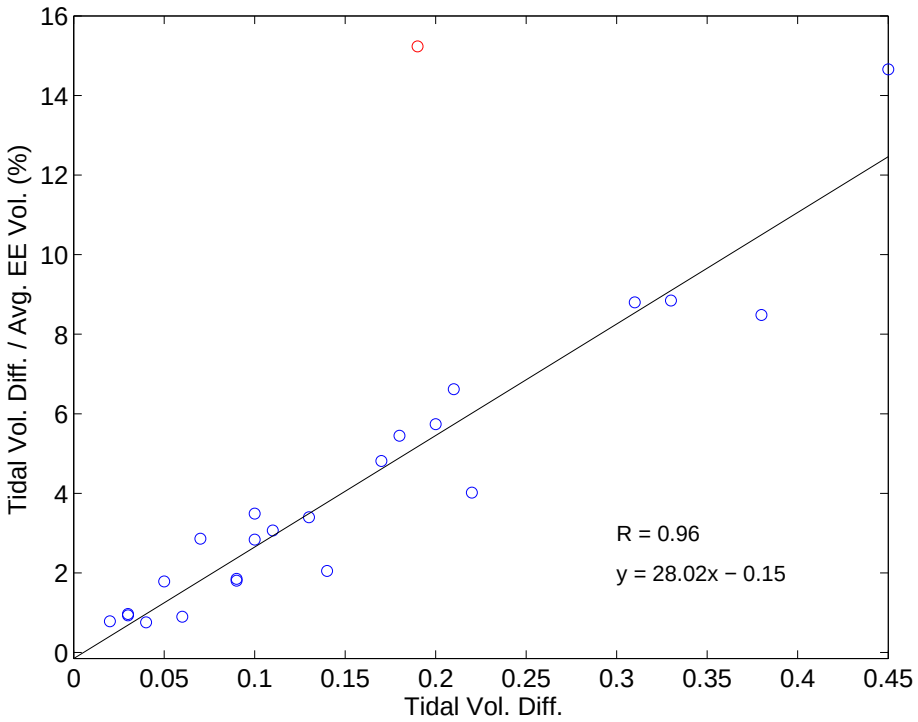

Figure 4.15. Relationship between tidal volume difference and the proportional tidal volume difference (tidal volume difference divided by the subject-specific average EE volume).

Table 4.2. Summary of mean and CV of JAC_{RATIO}, MSE, and gamma pass rate for reproducibility before effort correction, after global normalization, after ETV, and after ELV across all 24 human subjects.

Parameter	Before Correction	After Global	After ETV	After ELV
Mean	1.013 ± 0.037	1.002 ± 0.016	1.000 ± 0.014	1.002 ± 0.011
CV ($\times 10^{-2}$)	7.105 ± 2.076	7.105 ± 2.076	6.735 ± 2.528	6.099 ± 2.344
MSE ($\times 10^{-2}$)	1.045 ± 0.675	0.721 ± 0.437	0.691 ± 0.512	0.567 ± 0.486
Gamma	63.95 ± 15.76	70.94 ± 10.34	72.89 ± 11.62	76.05 ± 11.72

The reproducibility parameters are shown as cohort mean $\pm$ standard deviation)

ETV, and after ELV for all 24 human subjects (shown as mean $\pm$ standard deviation in the cohort). After effort correction, the mean of JAC_{RATIO} is closer to one, the CV of JAC_{RATIO} and MSE decrease, and the gamma pass rate increases, all indicating improved reproducibility. With regard to the gamma pass rate of all 24 subjects in this study, ELV and ETV gave better reproducibility than global normalization.

Table 4.3 is a summary of MSE and gamma pass rate for the subjects with tidal volume difference greater than 100 cc (shown as cohort mean $\pm$ standard deviation), for reproducibility before effort correction, after global normalization, and after ELV. The MSE improved by 36% for global normalization and 57% for ELV, and the gamma pass rate improved by 16% for global normalization and 33% for ELV. Similar comparisons can be made between global normalization and ETV, and between ETV and ELV. For cohort with tidal volume difference over 100 cc, the p-value with regard to the gamma pass rate is 0.005 between uncorrected and global normalization, 0.002 between uncorrected and ETV, 0.001 between uncorrected and ELV, 0.084 between ETV and global normalization, 0.003 between ELV and global normalization, and 0.156 between ETV and ELV. For all 24 subjects in this study, the p-value with regard

to the gamma pass rate is 0.009 between uncorrected and global normalization, 0.002 between uncorrected and ETV, 0.004 between uncorrected and ELV, 0.045 between ETV and global normalization, 0.036 between ELV and global normalization, and 0.341 between ETV and ELV.

Table 4.3. Summary of mean square error (MSE) and gamma pass rate for reproducibility before effort correction, after global normalization, and after ELV, for the subjects with tidal volume difference between scans greater than 100 cc.

	Mean square error (MSE, $\times 10^{-2}$)			Gamma pass rate		
	Before	After Global	After ELV	Before	After Global	After ELV
PFS-004	0.73	0.52	0.36	65.2	66.1	87.3
PFS-008	2.62	0.74	0.34	36.3	67.3	80.7
PFS-009	1.07	0.48	0.37	51.2	69.0	74.6
PFS-011	0.70	0.62	0.29	70.9	73.7	84.9
PFS-016	2.19	2.00	1.55	51.8	55.1	64.9
PFS-017	1.52	0.97	0.24	44.0	54.6	81.4
PFS-018	1.52	0.89	0.90	42.7	57.7	52.5
PFS-029	1.55	1.23	0.98	58.4	61.7	63.8
PFS-031	0.59	0.32	0.18	68.4	82.3	90.0
PFS-032	0.59	0.55	0.69	66.1	68.2	62.7
PFS-036	1.50	0.85	0.61	44.3	59.8	68.6
PFS-037	0.57	0.48	0.12	71.7	72.3	92.3
PFS-042	0.46	0.43	0.16	74.0	74.2	88.3
Mean	1.20	0.77	0.52	57.3	66.3	76.3
Std	0.68	0.45	0.41	12.9	8.3	12.7

The reproducibility parameters are shown as cohort mean $\pm$ standard deviation)

4.4 Discussion

Pulmonary function analysis across 4DCT scans will inevitably create the problem of different respiratory effort. In order to effectively and significantly quantify the longitudinal pulmonary function change due to radiation following RT [15, 7, 89, 91], the breath effort difference between scans before and after RT must be compensated for. Additionally, to optimize the radiation treatment plan using 4DCT-based

ventilation, normalization on ventilation maps should also be considered. In previous work, we have evaluated the reproducibility of ventilation estimates using two repeated prior-RT 4DCT scans [87, 88]. This chapter proposed two phase-selection-based normalization schemes (ETV and ELV), and compared them with the global normalization for the improvement of reproducibility in repeated 4DCT scans for 24 patients. Heterogeneity in lung ventilation rates demonstrates the limits of global normalization. Improvement in reproducibility was found to be correlated well with the respiratory effort difference. ELV was found to be significantly better than the other two normalization methods when differences in tidal volume were greater than 100 cc.

To our knowledge, this is the first study to investigate different normalization methods for 4DCT-based ventilation. In our previous work, we have shown the mean of $\mathrm{JAC}_{\mathrm{RATIO}}$ is strongly correlated with the volumes ratios in scans one and two [87], which hints a possible subject-specific global normalization using single scaling factor. Several other groups also suggested similar global normalization by scaling entire ventilation map with factors derived from ventilation values in a ROI or lobe that is uninvolved by radiation [115, 116, 91]. Although true when averaged over all voxels within the lung, in this chapter we have shown the ventilation rate of lung tissue is not uniform either spatially or temporally when studied at the voxel level. As shown in Figure 4.6, some regions that are highly ventilated during 40%IN to 60%IN become less ventilated during 60%IN to 80%IN, or vice versa. The Jacobian histograms also showed the heterogeneity of lung expansion rates. Using the right lower lobe as the

reference, the other four lobes, especially the upper and middle lobes, show various air filling rates. Hence, the global scaling normalization, which is true only with under the assumption of homogeneous lung expansion rate, may arbitrarily overnormalize or undernormalize regional tissue or lobes.

The intra-scan heterogeneity in lung expansion was studied using 48 4DCT scans from 24 subjects. Figure 4.7 clearly showed the undernormalized and overnormalized regions and explained the limits of global normalization. The similarity between the ventilation from EE to EI and the global normalized ventilation from EE to 80%IN also suggests that the weakness of global normalization may be disregarded when the effort difference is small. Additional study on the relationship between lung expansion heterogeneity and different inflation levels in Figure 4.8 (a) and (b) show that the ventilation difference and the associated global normalization error are is strongly correlated with the time interval, which further confirms that global normalization may be not applicable in case of great effort difference.

Figure 4.9 shows the lung volumes in two repeated 4DCT scans for two sample subjects. Even all subjects were coached and audible respiratory timing cues were used during imaging acquisition [94], discrepancy in lung volumes and breathing patterns still occurs in repeated scans for some subjects. Figure 4.9 implies that the 4D nature of data enables selection of phases with similar lung volume or tidal volume. Figure 4.11 shows colored ventilation maps in sagittal view for subject H-8 before and after effort correction. While the global normalization shows obvious ventilation variability in the dorsal lung, the reselection of phases in ETV and ELV

normalization methods produced JAC_{RATIO} maps that are closer to identity and more homogeneous. The most improvement in reproducibility was found in ELV correction for this subject.

Figure 4.12 shows scatter plots and histograms of JAC_{T1} and $JAC_{T2} \circ T0$ before correction, after global normalization, after ETV, and after ELV for the same subject H-8. We can notice that the mean of JAC_{T1} and $JAC_{T2} \circ T0$ are closer after every normalization method. In global normalization, a scaling factor was applied to the whole lung, resulting in a vertical shift of the scatter points without affecting the distribution pattern. After ETV and ELV the marginal histograms appear more similar. The dash line is the scatter regression line of JAC_{T1} and $JAC_{T2} \circ T0$, and the solid line is the reference line y=x. The regression line is closer to the reference line after normalization indicating compensated effort difference, and the better convergence of points on the regression line also reveals improved reproducible ventilation distribution in two scans. From Figure 4.13 (a), while the global normalization simply shifted the histogram along the horizontal axis, ETV and ELV normalization leaded to narrower histogram centered around one. The distribution of gamma pass rate in Figure 4.13 (b) further confirmed the improvement of reproducibility after the normalization methods where ELV gave the best results for this subject, followed by ETV, and then the global normalization.

The results of the experiment described in Figure 4.3 are shown in Figure 4.10 for subject H-8 and H-9 to show that the image selection in ETV is effective to improve reproducibility. As the tidal volume difference reduces gradually, the mean

of JAC_{RATIO} gets closer to one with reduced standard deviation. These results corroborate the rationality for picking phases with matching tidal volume to enhance reproducibility. Compared to the ELV method which sounds more related with the definition of lung expansion, ETV is also worth researching into. For example, the lung volume of scan two EE appears even greater than that of scan one EI for H-7 (refer to Figure 4.9 (a)), making ELV impossible. Compared to ELV which is based on the relationship between the definition of lung expansion and lung volume ratios, ETV is also meaningful because the reconstruction of the 0%IN phase is considered to be the most temporally stable, as 0%IN is typically the phase at which the lung spends relatively more time than the other phases during a typical respiration. Therefore, it sounds reasonable for ETV to pick phases starting with the EE phase for both baseline and followup scans.

The magnitude of effort difference varies for different subjects, and it is necessary to investigate the relationship between the degree of effort difference and the improvement of reproducibility after normalization. In Figure 4.14, more obvious improvement in reproducibility was observed for subjects with greater tidal volume difference. However, for some subjects with small tidal volume difference, e.g. less than 100 cc, the ETV and ELV may result in worse reproducibility. Arbitrary effort correction using ETV or ELV on the subjects with insignificant difference in lung volumes or tidal volumes may introduce more ventilation variation and thus deteriorate the reproducibility, because the number of phases from which ETV and ELV pick images are limited. In contrast, the global normalization uses a flexible float

value which suggests global normalization may be useful in situations of small effort difference. The drawbacks may be addressed by applying global normalization after ETV or ELV to account for the small residual tidal volume differences. With more subjects collected in the future study, it is essential to determine a cutoff tidal volume difference that below which we do not have to bother to do the normalization. The same tidal volume may represent different scales of effort for different subjects that may have various lung sizes. We have shown that the tidal volume difference is correlated with the subject-specific proportional tidal volume difference. Therefore it can be used a measure of the effort difference across different subjects.

All statistical parameters indicate the three effort correction methods improved reproducibility, especially when changes in respiratory effort are bigger than 100 cc, with great significance. From Table 4.2 we see for all subjects ELV gave better results than ETV and global normalization. For cohort with tidal volume difference over 100 cc, ELV is significantly better than global normalization ($p = 0.003$), while no significance was found between ETV and global normalization ($p = 0.084$) or between ETV and ELV ($p = 0.156$). Collecting more subjects in the future will help investigate more for these normalization methods.

Only inspiration phases were used in this study. Compared to inspiration which is driven by active respiratory muscles, the expiration depends upon elastic recoiling force of lung tissue, frictional resistance of small airways, and the cross-sectional areas of large airways [121]. The ventilation rate during expiration may be more heterogeneous than in inspiration. Over the upper half of the vital capacity,

the relationship between maximal expiratory flow and degree of inflation is effort-dependent [122]. The peak air flow rate is in the upper half of the vital capacity and more air is expired during the upper half of expiration [121, 122]. To avoid the complexity, currently we exclude the intermediate expiration phases and use only inspiration phases to correct for breath effort.

The phase-selection-based pulmonary function normalization strategies may be influenced by reconstruction of 3D CT images at different levels in 4DCT, accuracy of lung segmentation, and lung volume change due to radiation-induced tumor shrinkage etc. Investigation of more subjects will help analyze and compare these normalization methods. The heterogeneity in lung expansion shows that effective normalization schemes may require both a spatial and temporal component for respiratory effort correction. In the future ETV and ELV can be applied to the scans before and after RT, or images with better matching lung volumes can be simply reconstructed, to make the radiation-induced function change free of effort difference and enable more significant analysis [114]. Moreover, the pulmonary function metrics so far reflects lung ventilation only from one phase to another phase, and more robust parameters for pulmonary function are worth being investigated to fully utilize the 4D nature of data, which may tell more information about the lung tissue dynamics.

4.5 Summary

In this chapter we presented two normalization strategies (ETV and ELV) to correct for respiratory effort difference by selecting alternate respiratory phases from 4DCT, and compared them with global normalization. All normalization strate-

gies improved reproducibility when changes in respiratory effort were great, and the improvement of reproducibility is highly correlated with the changes in respiratory effort. ELV gave better results than global normalization as effort difference increase. Heterogeneity in lung expansion rates was quantified and analyzed, and the global normalization is demonstrated to be inadequate to correct the ventilation map with single scaling factor especially for subjects with great respiratory effort difference. Collecting more subjects in the future will help better understand the normalization strategies.

CHAPTER 5

DISCUSSION

In this thesis, we analyze the regional pulmonary function using 4DCT and image registration in the following topics: reproducibility of transformation-based ventilation measurement, reproducibility of intensity-based ventilation measurement, and normalization on the ventilation map for breath effort variation across scans.

Reproducibility of transformation-based ventilation

Lung function depends on lung expansion and contraction during the respiratory cycle. Respiratory-gated CT imaging and 3D image registration can be used to locally estimate lung tissue expansion and contraction (regional lung volume change) by computing the determinant of the Jacobian matrix of the image registration deformation field. In Chapter 2, we examine the reproducibility of transformation-based measures of lung tissue expansion in two repeat 4DCT acquisitions within a short time interval of mechanically ventilated sheep and free breathing humans. The animal subjects were anesthetized and mechanically ventilated, while the humans were awake and spontaneously breathing based on respiratory pacing audio cues. From each 4DCT data set, an image pair consisting of a volume reconstructed near end inspiration and a volume reconstructed near end exhalation was selected. The end inspiration and end exhalation images were registered using a tissue volume preserving deformable registration algorithm and the Jacobian of the registration deformation field was used to measure regional lung expansion. The Jacobian map from the baseline data set

was compared to the Jacobian map from the followup data by measuring the voxel-by-voxel Jacobian ratio. The reproducibility of the Jacobian values was found to be strongly dependent on the reproducibility of the subject's respiratory effort and breathing pattern. Our results also show that good reproducibility can be obtained in anesthetized, mechanically ventilated animals, but variations in respiratory effort and breathing patterns reduce reproducibility in spontaneously-breathing humans. The global linear normalization can globally compensate for breathing effort differences, but a homogeneous scaling does not account for differences in regional lung expansion rates.

Reproducibility of intensity-based ventilation

As an alternate method, CT imaging and image registration can be used to estimate the regional lung volume change by observing CT voxel density changes during inspiration or expiration. In Chapter 3, we examine the reproducibility of intensity-based measures of lung tissue expansion and contraction in same sheep and human subjects. The intensity-based measures are compared to the results of the transformation-based method. The CT density change in the registered image pair was used to compute intensity-based specific air volume change (SAC) and the intensity-based Jacobian (IJAC), while the transformation-based Jacobian (TJAC) was computed directly from the image registration deformation field. IJAC is introduced to make the intensity-based and transformation-based methods comparable since SAC and Jacobian may not measure the same physiological phenomenon and have different units. A gamma index metric was introduced to measure voxel-

by-voxel reproducibility considering both differences in ventilation and distance between matching voxels. We also tested how different CT pre-filtering levels affected intensity-based ventilation reproducibility. Higher reproducibility was found for anesthetized mechanically-ventilated animals than for the humans for both the intensity-based (IJAC) and transformation-based (TJAC) measures. The human IJAC maps had scan-to-scan correlation coefficients of 0.45±0.14, a gamma pass rate 70±8 without normalization and 75±5 with normalization. The human TJAC maps had correlation coefficients 0.81±0.10, a gamma pass rate 86±11 without normalization and 93±4 with normalization. To summarize, the gamma pass rate and correlation coefficient of the IJAC maps gradually increased with increased smoothing, but were still much lower than those of the TJAC maps. The transformation-based ventilation maps show better reproducibility than the intensity-based maps, especially in human subjects. Reproducibility was also found to depend on variations in respiratory effort; all techniques were better when applied to images from mechanically ventilated sheep compared to spontaneously-breathing human subjects. Nevertheless, intensity-based techniques applied to mechanically ventilated sheep were less reproducible than the transformation-based applied to spontaneously-breathing humans, suggesting the method used to determine ventilation maps is important. Pre-filtering of the CT images may help improve the reproducibility of the intensity-based ventilation estimates, but even with filtering the reproducibility of the intensity-based ventilation measurements are not as good as that of transformation-based ventilation measurements.

Respiratory Effort Correction

In Chapter 4, we present and compare normalization schemes that correct ventilation images for variations in respiratory effort and assess the reproducibility improvement after effort correction. Repeat 4DCT image data acquired within a short time interval from 24 patients prior to radiation therapy (RT) were used for this analysis. Intra-scan change of pulmonary function was studied to demonstrate the deficiency of global normalization. In addition to computing the ventilation maps from end expiration to end inspiration, we investigated the effort normalization strategies using other intermediated inspiration phases upon the principles of equivalent tidal volume (ETV) and equivalent lung volume (ELV). Additional analysis was performed to verify the effectiveness of ETV correction method. Scatter plots and the statistical parameters of the repeat ventilation maps and the Jacobian ratio map were generated for 4 conditions: no effort correction, global normalization, ETV, and ELV. The pattern of regional pulmonary ventilation changes as lung volume changes. All effort correction strategies improved reproducibility when changes in respiratory effort were greater than 150 cc ($p < 0.005$ for the gamma pass rate). Improvement of reproducibility was correlated with respiratory effort difference (R = 0.744 for ELV in cohort with tidal volume difference greater than 100 cc). For tidal volume difference between 20 and 130 cc's, global normalization improved reproducibility when compared to no effort correction (p = 0.026), and was statistically equivalent to ETV and ELV when tidal volume difference was small. For the cohort with tidal volume difference greater than 100 cc, the average gamma pass rate improves from 63.1 before

correction to 70.8 after global normalization, 72.9 after ETV, and 75.5 after ELV. ELV was found to be significantly better than global normalization ($p = 0.003$). To conclude, all normalization strategies improve the reproducibility of our pulmonary ventilation measures, and the improvement of reproducibility is highly correlated with the changes in respiratory effort. ELV gave better results than global normalization as effort difference increase. However, based on the spatial and temporal heterogeneity in the lung expansion rate, a single scaling factor (e.g., global normalization) appears to be inadequate to correct the ventilation map when changes in respiratory effort are large.

To our knowledge, this is the first effort to investigate the reproducibility of registration-based ventilation measurement with repeat 4DCT before RT. Mathew et al. [20] evaluated the reproducibility of 3-helium magnetic resonance imaging (MRI) ventilation measurements by comparing the ventilation defect volume (VDV), and reported reproducibility of VDV was higher at same-day rescan ($R^2 = 0.941$) compared to 7-day rescan ($R^2 = 0.576$) in 8 healthy volunteers and 16 COPD subjects. However, VDV reproducibility throws away most of the spatial correlations, and we have no sense for how the actual measurement values compare on a voxel-by-voxel level. Nyeng et al. [92] studied local lung volume change in two thoracic 4DCT scans in five patients, however, the two scans were different - one scan with respiration restricted by an abdominal compression plate and the other under free breathing. To determine the real underlying radiation-induced pulmonary function changes using 4DCT and image registration, intra-subject variability needs to be established with voxel-by-

voxel reproducibility study. In this thesis, we have investigated the reproducibility of transformation-based (correlation coefficient 0.81±0.10) and intensity-based (correlation coefficient 0.45±0.14) measures of lung tissue expansion in two repeat prior-RT 4DCT acquisitions. Similarly, Yamamoto et al. [86] investigated the reproducibility of lung ventilation over two different time frames but reported moderate voxel-based correlation between two ventilation images (Spearman rank correlation 0.50±0.15).

To our knowledge, this is also the first study to propose and summarize the normalization strategies for respiratory effort difference across scans. Limitations exist in previous normalization methods, such as the percentile images used by Guerrero et al. [47, 7, 14, 91], and the global normalization used by Zhang et al. [116], Seppenwoolde et al. [115], and Vinogradskiy et al. [91]. The global normalization approach is based on the assumption and/or approximation that the lung expansion rate is spatially uniform. If the assumption is not true, the global normalization method will arbitrarily overnormalize or undernormalize regional ventilation values. In this thesis, we have demonstrated the spatial and temporal heterogeneity in the lung expansion rate, and thus the limitations of global normalization. The two normalization strategies proposed in this thesis, ETV and ELV, differ from other normalization methods in that they select independent respiratory phases to compute pulmonary function, rather than modify the computed ventilation values directly. ELV and ETV were found to give better reproducibility than global normalization, especially for subjects with greater respiratory effort difference.

4DCT has several advantages over SPECT and MRI as a tool to measure

pulmonary function and radiation induced tissue toxicity. Quantifying overall uncertainty in 4DCT-based ventilation measurement can help include subject reproducibility when assessing pulmonary function change in longitudinal studies. The normalization study on respiratory variations will also have important applications when being used as either input information into the radiation therapy treatment planning process, or for longitudinal study of pulmonary function.

There are some limitations of our technique. First, variability in the cycle-to-cycle expansion of a spontaneously breathing lung may be one major factor that influence the overall reproducibility of ventilation measurements, while slight variations in imaging protocol, patient position, reconstruction, and image processing factors will also contribute to variability. However, we can not separate these factors, but instead are measuring the total effect of all factors combined. Second, global normalization appears sufficient for small variations in respiratory effort, but ETV and ELV perform better when it comes to subjects with large respiratory effort difference. The normalization problem may be better addressed by applying global normalization after ETV or ELV to account for the small residual tidal volume differences. Third, ventilation in this thesis is calculated between only a pair of 3D CT images. More sophisticated ventilation technologies may utilize the full 4DCT scan to better characterize the lung dynamics.

CHAPTER 6

MAJOR CONTRIBUTIONS

The major contributions of this thesis include:

- Developed and validated a process for establishing measurement reproducibility in 4DCT-based ventilation,
- Developed methods to assess reproducibility,
- Quantified reproducibility of transformation-based ventilation measurement,
- Quantified reproducibility of intensity-based ventilation measurement,
- Developed analytical models of how CT image noise affects the intensity-based ventilation,
- Investigated the heterogeneity in lung expansion pattern and the limits of global normalization,
- Developed and validated two normalization approaches taking advantage of the 4D nature of the data: ETV and ELV,
- Investigated the relationship between improvement of reproducibility and the changes in respiratory effort.

CHAPTER 7

FUTURE DIRECTIONS

In this chapter, we discuss some potential studies that will be interesting to explore in future research on 4DCT-based pulmonary function analysis. The work presented in this thesis can be extended and further explored with regard to both methodologies and applications.

7.1 4D Image Registration

Currently the 4DCT images are not fully utilized. 4DCT are reconstructed by sorting the CT data to corresponding phases from many respiratory cycles according to the respiratory signal that is simultaneously recorded either internally or externally [55]. It is important but also a great challenge to keep the calculated lung motion consistent over time when analyzing the ventilation and tissue motion dynamically in 4DCT. However, current approaches including the registration used in this thesis usually register each phase image to a pre-defined phase image independently. The similarity metric is defined without considering the temporal coherence in 4DCT. Therefore, the derived displacement field is calculated between only two time points and is subject to only the spatial correspondence of two 3D CT images.

A fully 4D image registration can register a set of 3D images simultaneously taking into consideration both spatial and temporal smoothness of transformations. It is of significance if we want to study the dynamic 4D properties of breathing motion without losing the temporal coherence. Recently 4D image registration has eventually

become a hot topic and many researchers have started investigating into it, such as Castillo et al. [78], Metz et al. [79], Vandemeulebroucke et al. [80], Wu et al. [81, 82]. Based on the 4D registration, Jacobian versus time and regional hysteresis motion of lung tissue can be analyzed.

Another significance of 4D image registration relates to the elimination of motion artifacts. Even with the fast developing 4DCT scanners, only a segment of human body can be scanned at each couch position. In the reconstruction process, when the CT segments from multiple breathing cycles are sorted with regard to the respiratory signal to assemble a full 4DCT scan, the CT segments may not be set to the correct volume due to unavoidable patient free breathing, thus causing motion artifacts including motion blur, vessel mismatch, slab misalignment, and irregular tumor shape [81]. 4D image registration may provide a good solution for the artifacts problem by ensuring spatial and temporal correspondence simultaneously.

7.2 Dynamic Measures of Pulmonary Function

In this thesis we use 3D approach to estimate regional pulmonary function in which only the EE and EI volumes were used. However, most other phases in the respiratory circle of 4DCT have not been analyzed. Reconstructed series of CT images in 4DCT can be fully utilized to encode the ventilation and motion information with high spatial resolution and moderate temporal resolution [55]. The complete temporal measurements of ventilation and trajectory motion may be used to develop new dynamic measures that may better estimate the lung function and may be more robust to the noise and image artifacts.

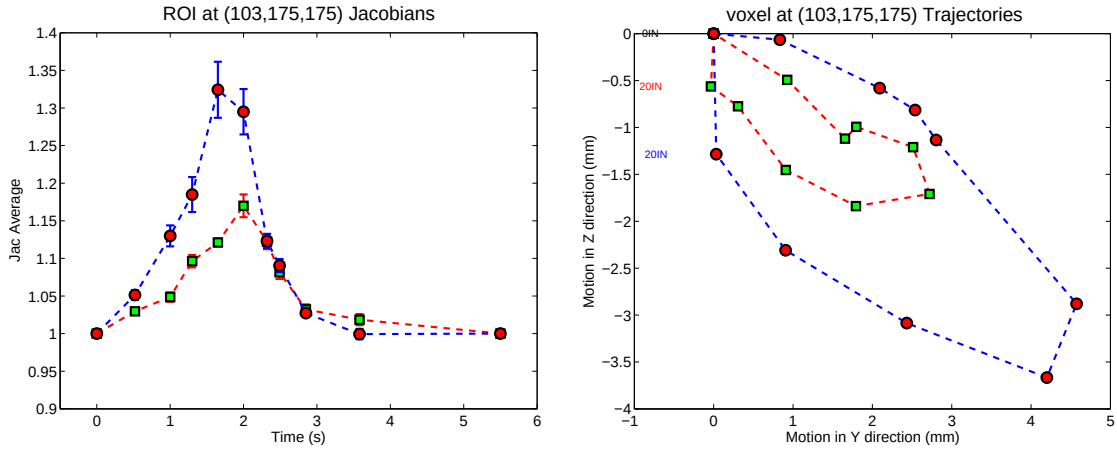

Figure 7.1. Non-linear nature of pulmonary biomechanics. Left figure represents Jacobian of a specified ROI versus time for each scan; right figure shows the spatial travel of the ROI for each respiratory phase (Scan 1 - blue circles, Scan 2 - red squares).

Figure 7.1 shows the averaged dynamic ventilation and averaged displacement trajectory for one ROI (size 11 mm $\times$ 11 mm $\times$ 11 mm, ventral lung) from repeated 4DCT scans. The dynamic Jacobian curves on the left plot describe regional lung volume change versus time in the respiratory circle, and the trajectory hysteresis on the right is useful to depict regional tissue motion with time. For this ROI, we can see obvious variations of lung expansion and contraction in two repeat scans. We can see the tissue achieves their maximum ventilation at 80%IN for scan1, which is not available from the 3D analysis. The hysteresis study can be used to evaluate 4D image registration algorithm described in Section 7.1. Additionally, the respiratory tissue motion is closely related to the regional pulmonary ventilation and thus knowledge of lung motion would be valuable as well [55]. Clinically, to avoid irradiating healthy tissue during RT and to allow more dose targeted to the diseased region, accurate

motion information is also important [123, 55].

The nonlinear nature of dynamic Jacobian inspires us to extract new parameters that are more physiologically meaningful and more tolerant to the variations in breath effort, which is a crucial issue to consider for pulmonary function comparison across 4DCT scans. Linear or nonlinear curve-fitting models are worth being investigated to extract parameters that can better describe the lung dynamics. Evaluation on the new models on subjects with great respiratory effort variation can be compared to the results presented in this thesis.

CHAPTER 8

CONCLUSION

Reproducibility of 4DCT-based ventilation measurements was presented, and normalization strategies to compensate for respiratory effort variations were investigated. The findings are novel and can help quantify statistically significant changes in pulmonary function following RT.

Respiratory-gated 4DCT imaging and image registration can be used to estimate the regional pulmonary function by a transformation-based ventilation metric which is computed directly from the deformation field, or an intensity-based metric which is based on CT density change in the registered image pair. In this thesis, we have evaluated the reproducibility of regional pulmonary function measures using two repeat 4D image acquisitions taken within a short time interval for both transformation-based (Chapter 2) and intensity-based (Chapter 3) metrics. The transformation-based ventilation maps show better reproducibility than the intensity-based maps, especially in human subjects. Reproducibility is found to depend on changes in respiratory effort. Analytical model of intensity-based ventilation quantifies the big impact of CT image noise. The effect of pre-filtering of the CT images is found to be limited.

We have proposed and compared the normalization schemes that correct ventilation images for variations in respiratory effort, and assessed the reproducibility improvement after effort correction (Chapter 4). All normalization strategies im-

prove the reproducibility of pulmonary ventilation measures, and the improvement of reproducibility is highly correlated with the changes in respiratory effort. ELV gave better results than global normalization as effort difference increase. Spatial and temporal heterogeneity in the lung expansion rate demonstrates the deficiency of global normalization.

APPENDIX A

SUPPLEMENTAL REPRODUCIBILITY RESULTS

A.1 Reproducibility of transformation-based method

In this section, we will provide some supplemental results for Chapter 2, the reproducibility study on transformation-based ventilation measurements.

Figure A.1 shows a 3D view of landmarks distribution in subject H-2 at scan1 100%IN. We could see the landmarks also form a uniform distribution in the superior-inferior direction. Figure A.2 shows landmark distances before and after image registration in each of the three pairs for the same subject. The first two columns are for registration between scan2 0%EX and scan1 0%EX (T0), the middle two columns for registration between scan1 100%IN to scan1 0%EX (T1), and the last two columns for registration between scan2 100%IN to scan2 0%EX (T2).

In addition to the results for subjects H-2, H-4, and H-8 that are presented in Chapter 2, Figure A.3 and Figure A.4 show the Jacobian scatter plots and Bland-Altman plots for more human subjects: H-1, H-7, H-9, H-10, H-11, H-12.

Guerrero et al. [47, 7, 14, 91] proposed converting ventilation images to percentile images to reduce the sensitivity to the maximum ventilation value on a particular image. The Jacobian percentile map is calculated based on the cumulative distribution function (CDF) of the Jaocbian values distribution. The CDF of Jacobian describes the probability that a ventilation value J will be found at a value less than or equal to J. In this study, we also investigated the scatter plot of Jacobian CDF, the results of which for 9 subjects are shown in Figure A.5 and Figure A.6.

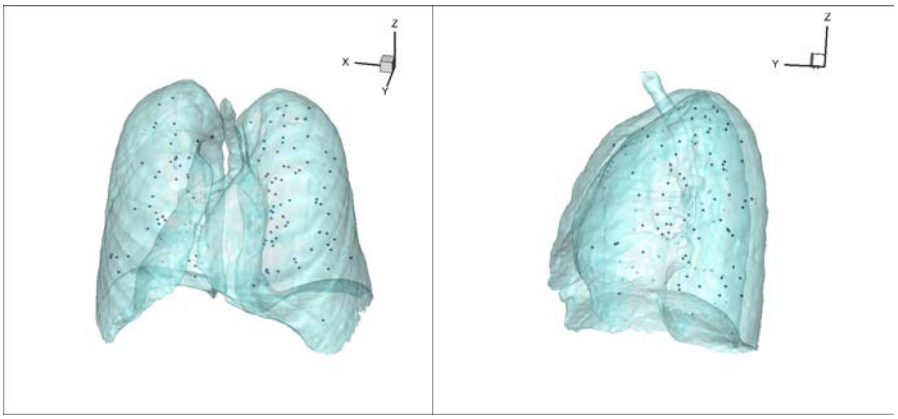

(a) (b)

Figure A.1. 3D views of the landmarks for subject H-2. The dark blue spheres indicate the defined landmarks. (a) anterior-posterior and (b) right-left.

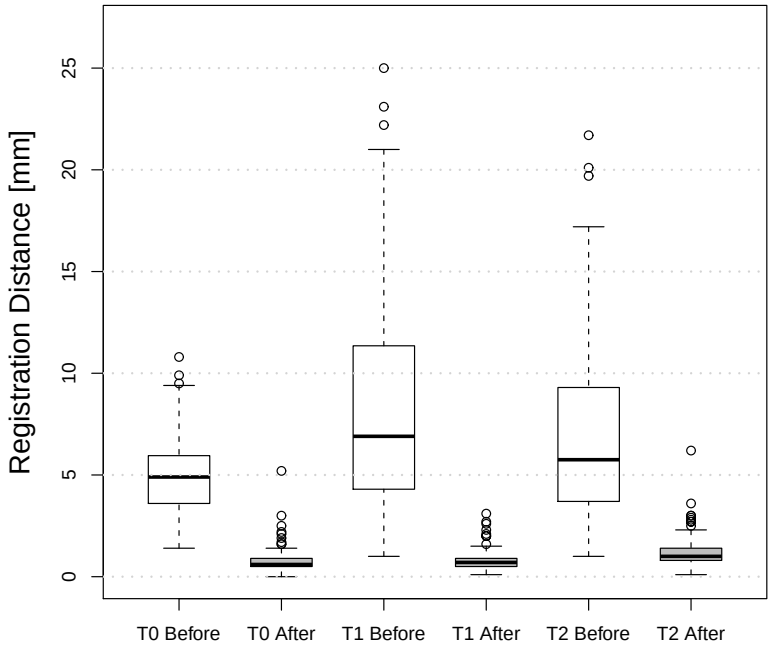

Figure A.2. Box plot for landmark distances before and after registration for subject H-2 for the three registration pairs T0, T1, and T2. White box represents the landmark distance before image registration, and gray box represents the landmark distance after image registration.

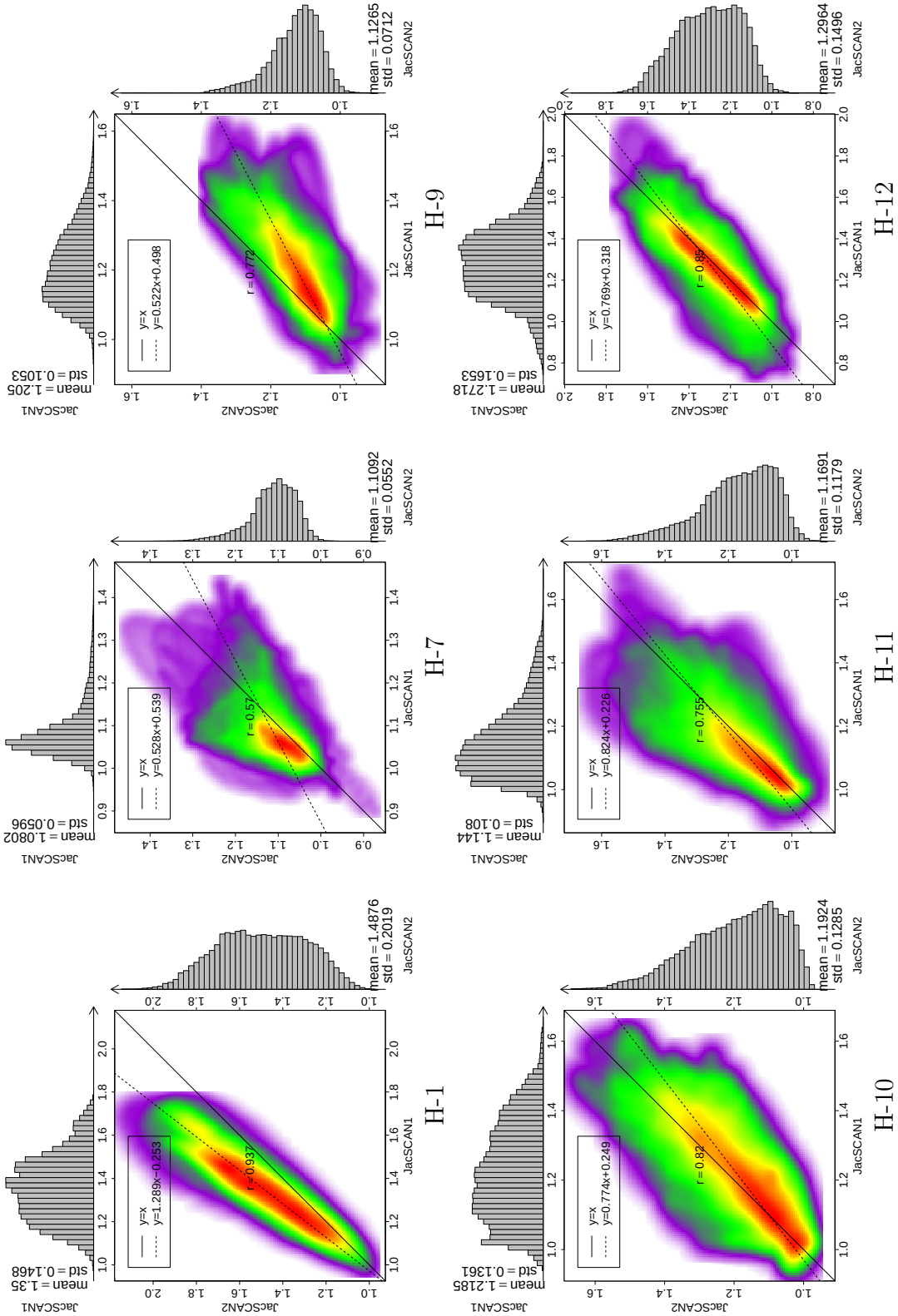

Figure A.3. Jacobian scatter plots for more human subjects: H-1, H-7, H-9, H-10, H-11, H-12.

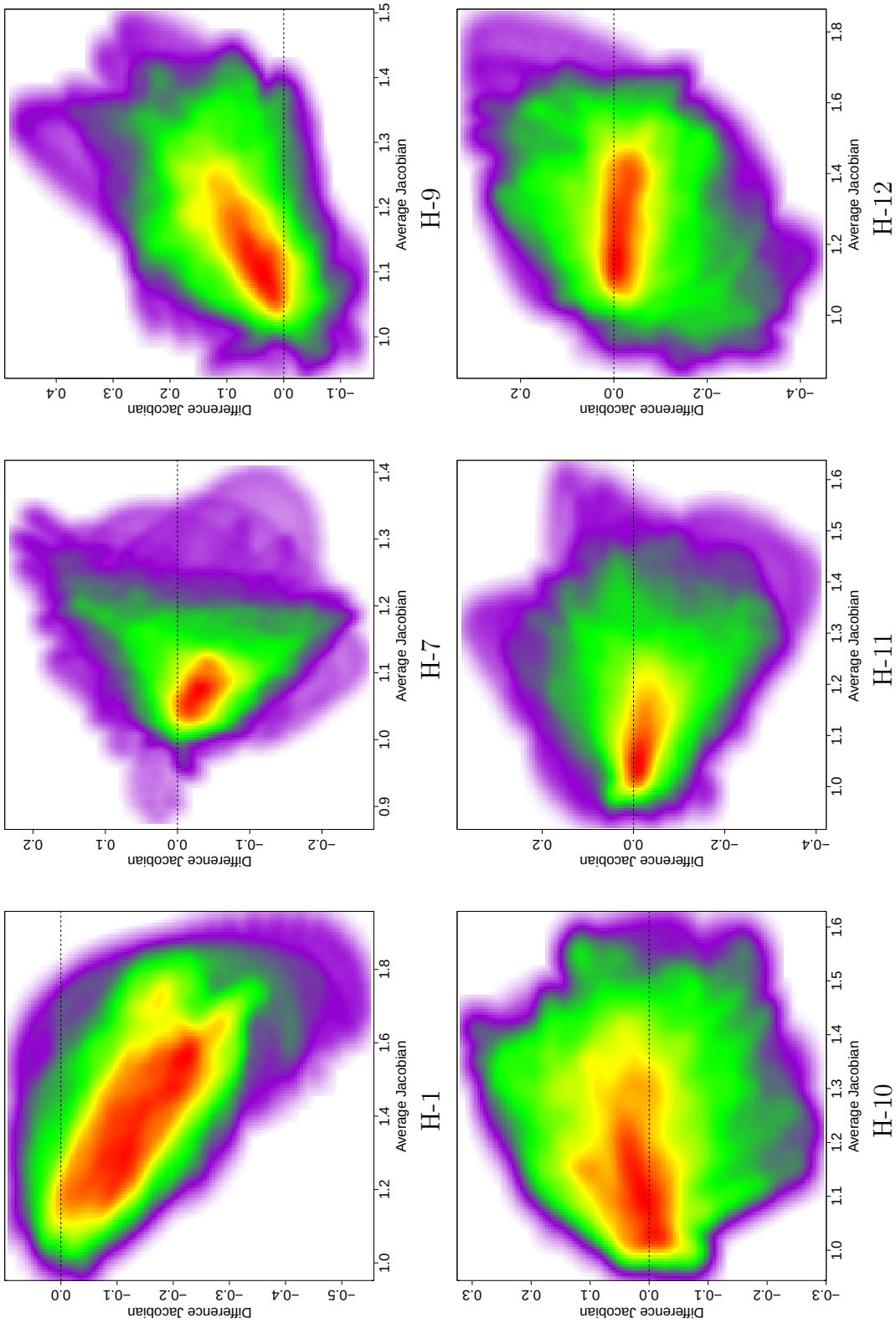

Figure A.4. Bland-Altman plots for more human subjects: H-1, H-7, H-9, H-10, H-11, H-12.

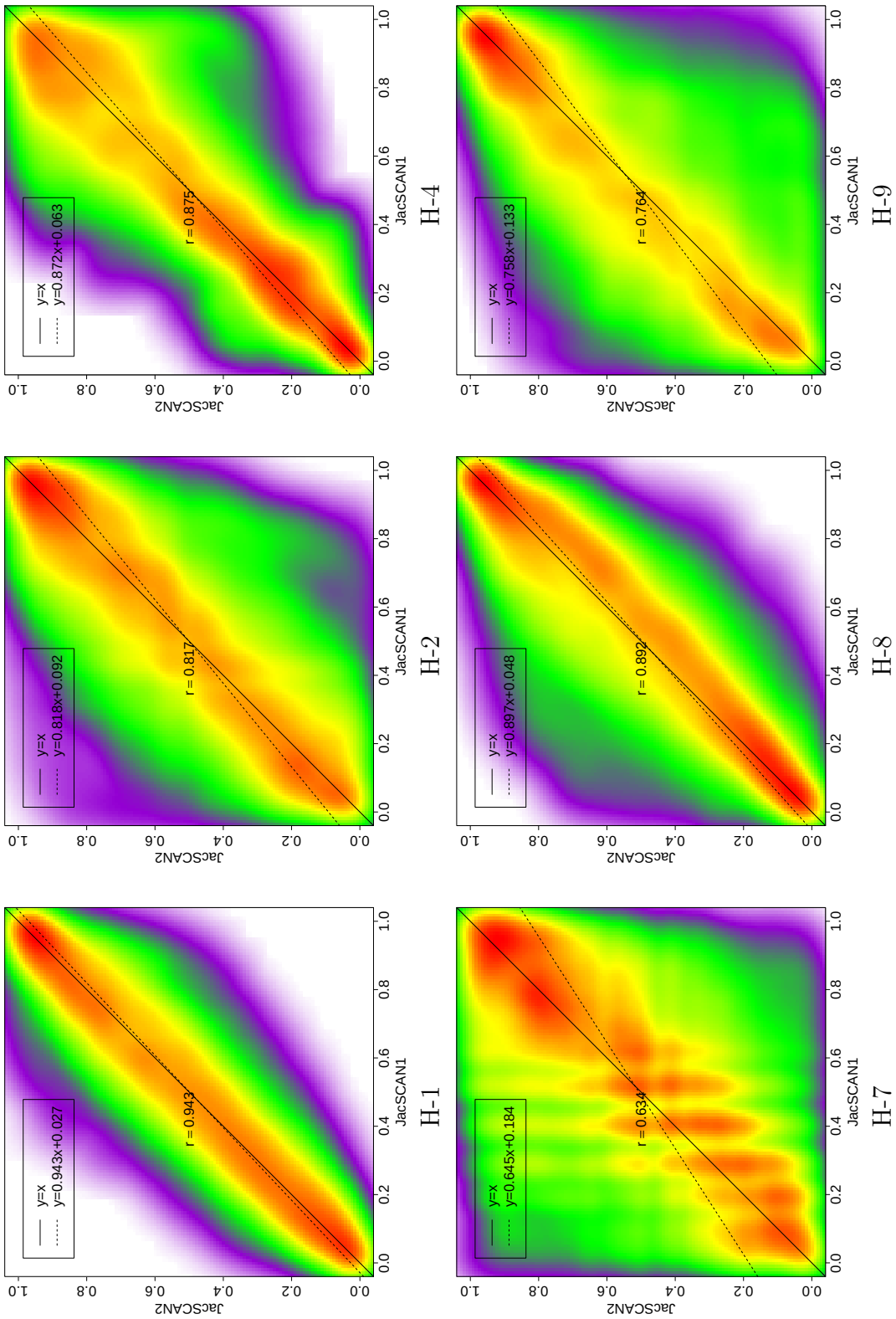

Figure A.5. Scatter plots of percentile Jacobian for human subjects: H-1, H-2, H-4, H-7, H-8, H-9.

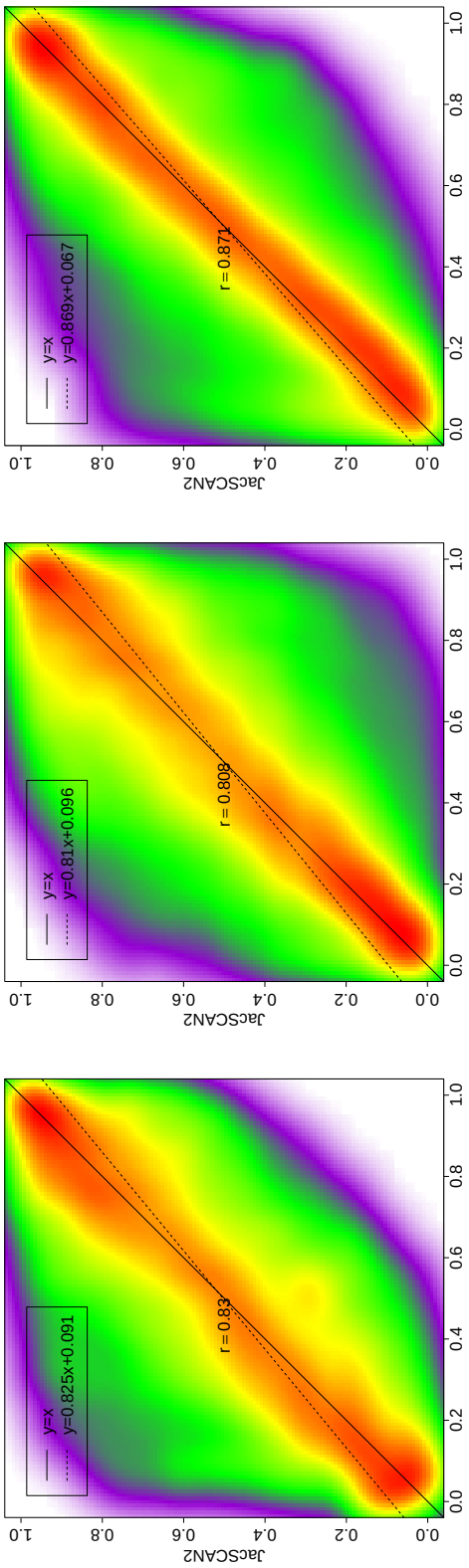

Figure A.6. Scatter plots of percentile Jacobian for human subjects (continue): H-10, H-11, H-12.

A.2 Reproducibility of intensity-based method

In this section, we will provide some supplemental results for Chapter 3, the reproducibility study on intensity-based ventilation measurements.

Figure A.7 shows coronal and sagittal views of the original CT image, the SAC map calculated from scan one and from scan two, and the gamma map for animal S-1 (with distance-to-agreement (DTA) of 4 mm and ventilation difference criterion of 5%). Non-pulmonary voxels that are outside the range [-999, -250] HU were not processed. The SAC image from scan two (SAC_{T2}) is transformed through the T0 transformation to be converted into the coordinate system of scan one, producing $T0 \circ SAC_{T2}$. The T0 transformation allows the two SAC images to be directly compared in the same coordinate framework, and allows us to compute the voxel-by-voxel gamma comparison γ_{SAC}.

Figures A.8 and A.9 show the coronal and sagittal views of the original CT image, the SAC map calculated from scan one and from scan two, and the gamma comparison map for human subjects H-4 and H-9. As with the animal subjects, the scan two SAC image has been transformed into the coordinate system of scan one using the T0 transformation. Subjects H-4 and H-9 were selected to illustrate cases with good and poor reproducibility when comparing the scan one to scan two results.

As shown in Equation 3.3, the SAC maps are computed by using the intensity information (HU) of registered CT images EE, EI and the displacement field from image registration. Consequently the noise in the SAC maps and poor reproducibility may derive from two sources, noise in original CT images and image registration error.

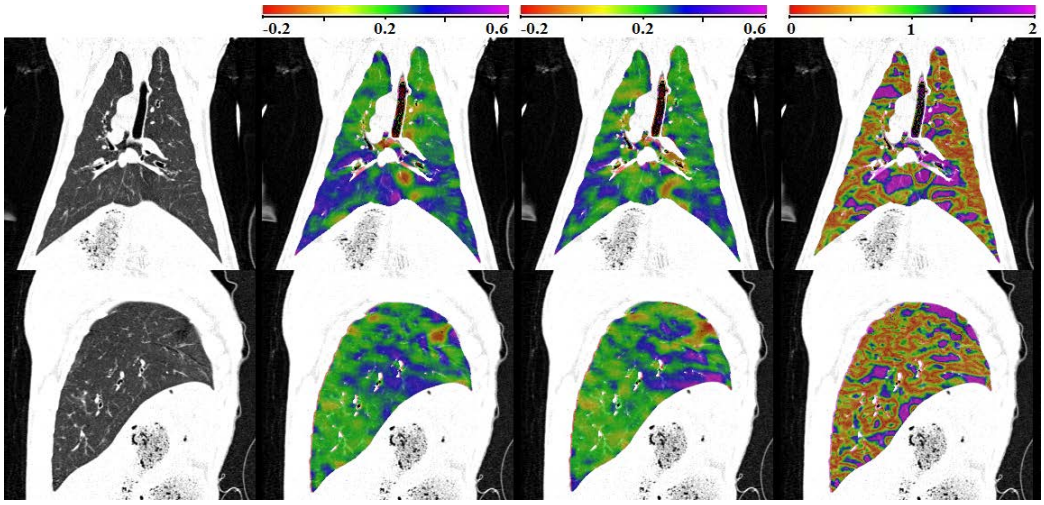

Figure A.7. Coronal (top) and sagittal (bottom) views of (left to right) the original CT, $\mathrm{SAC}_{\mathrm{T1}}$, $\mathrm{T0} \circ \mathrm{SAC}_{\mathrm{T2}}$, and γ_{SAC} for animal subject S-1. Color scales are -0.2 to 0.6 for $\mathrm{SAC}_{\mathrm{T1}}$ and $\mathrm{T0} \circ \mathrm{SAC}_{\mathrm{T2}}$, and 0 to 2 for γ_{SAC}.

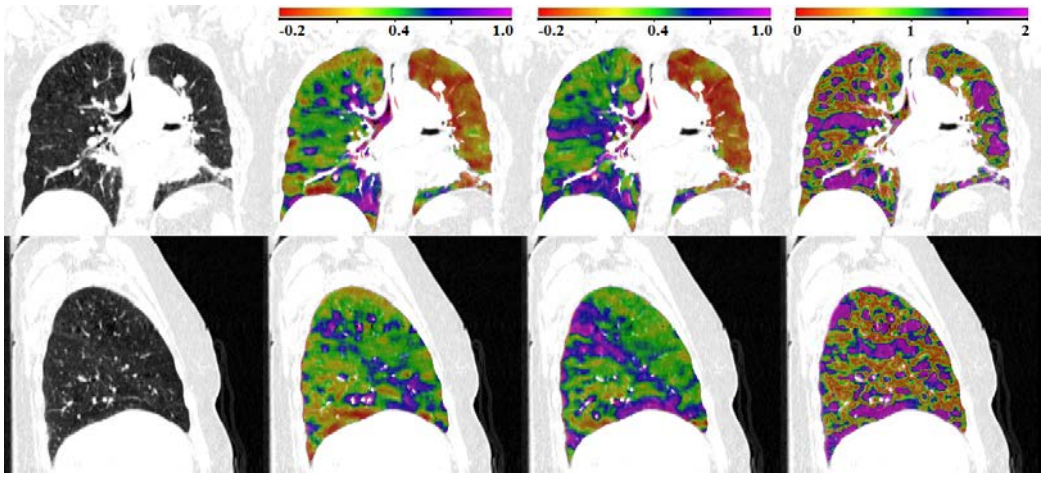

Figure A.8. Transverse (top) and coronal (bottom) views of (left to right) the original CT, $\mathrm{SAC}_{\mathrm{T1}}$, $\mathrm{T0} \circ \mathrm{SAC}_{\mathrm{T2}}$ and γ_{SAC} for human subject H-4. Color scales are -0.2 to 1.0 for $\mathrm{SAC}_{\mathrm{T1}}$ and $\mathrm{T0} \circ \mathrm{SAC}_{\mathrm{T2}}$, and 0 to 2 for γ_{SAC}.

Figures A.10 show the color maps after the highest level of filtering on original CT images (neighborhood kernel size 15 mm $\times$ 15 mm $\times$ 15 mm). The color maps of $T0 \circ SAC_{T2}$ and γ_{SAC}after specific air volume normalization are shown in the third column of Figure A.10. Correspondingly, Figure A.11 shows the change of the 2D kernel density estimates for subject H-9 with different levels of filtering on CT images.

Figure A.12 and Figure A.13 show the SAC scatter plots for three animal subjects and nine human subjects. Figure A.14 shows the SAC Bland-Altman plots for one typical animal subject S-1 and three typical human subjects H-2, H-8, H-9.

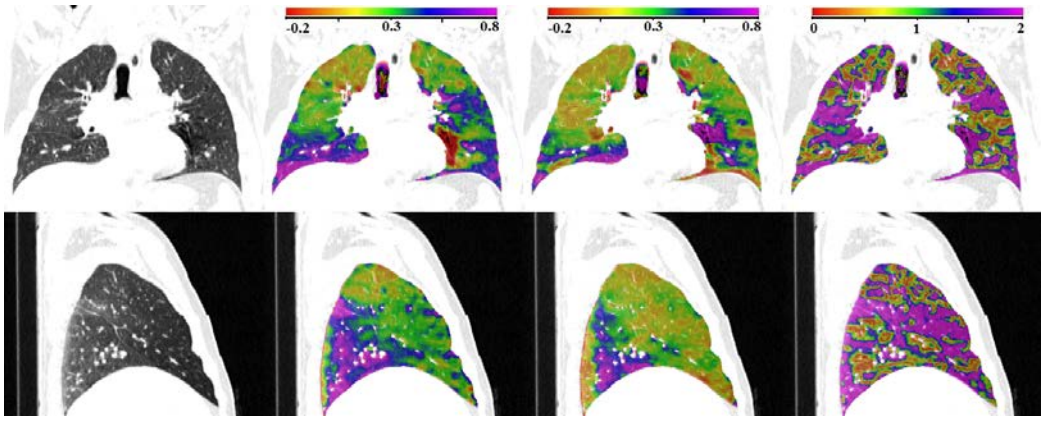

Figure A.9. Transverse (top) and coronal (bottom) views of (left to right) the original CT, $\mathrm{SAC}_{\mathrm{T1}}$, $\mathrm{T0} \circ \mathrm{SAC}_{\mathrm{T2}}$ and γ_{SAC} for human subject H-9. Color scales are -0.2 to 0.8 for $\mathrm{SAC}_{\mathrm{T1}}$ and $\mathrm{T0} \circ \mathrm{SAC}_{\mathrm{T2}}$, and 0 to 2 for γ_{SAC}.

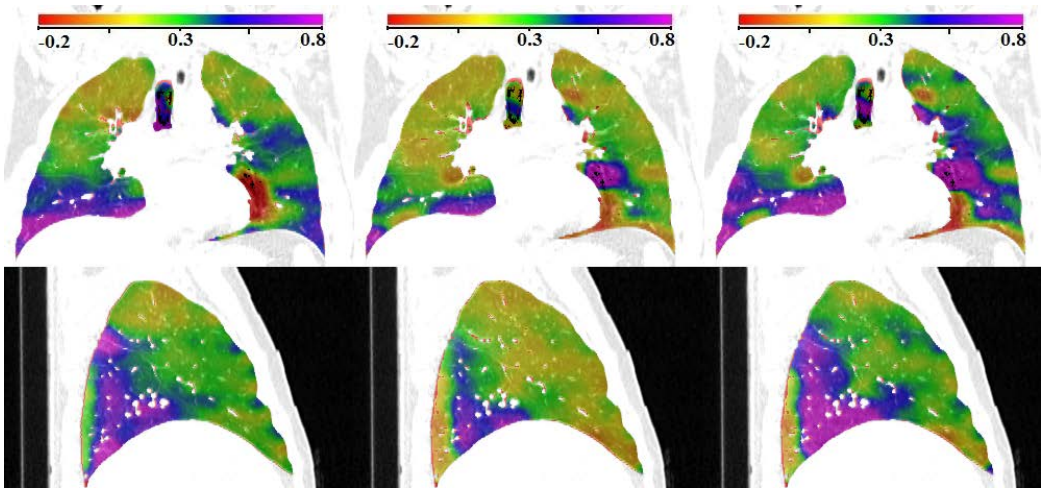

Figure A.10. Transverse (top) and coronal (bottom) views of (left to right) $\mathrm{SAC}_{\mathrm{T1}}$, $\mathrm{T0} \circ \mathrm{SAC}_{\mathrm{T2}}$ and normalized $\mathrm{T0} \circ \mathrm{SAC}_{\mathrm{T2}}$ for human subject H-9, after high level of filtering on original CT images with local average kernel $15 \times 15 \times 15$. Color scales are -0.2 to 0.8 for all ventilation maps.

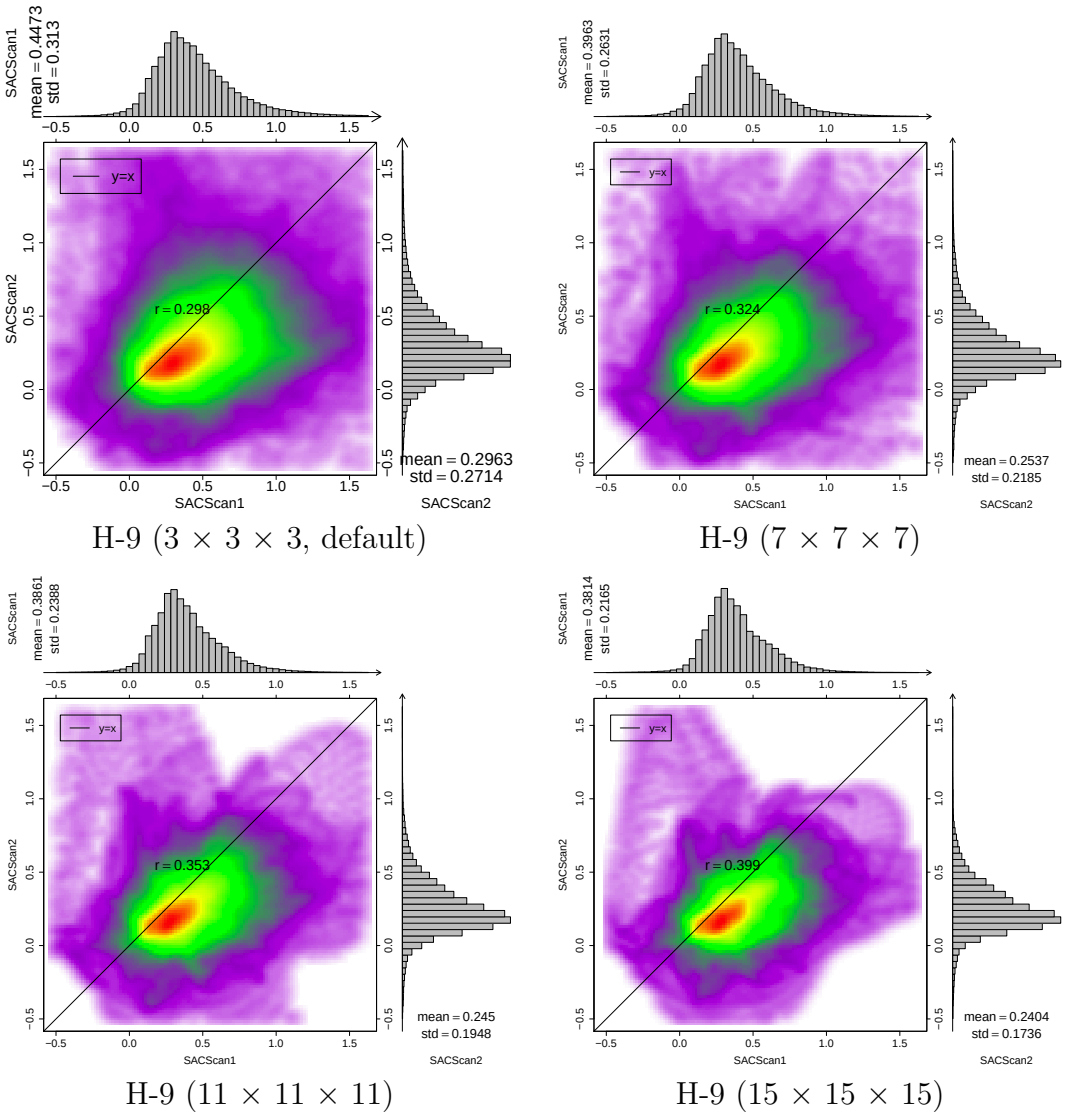

Figure A.11. Smoothed color density scatter plot and marginal histograms of $\mathrm{SAC}_{\mathrm{T1}}$ and $\mathrm{T0} \circ \mathrm{SAC}_{\mathrm{T2}}$ for one human subjects H-9 with different levels of filtering on the original CT images. Ordered left to right and top to bottom, the local average kernel sizes are $3 \times 3 \times 3$, $7 \times 7 \times 7$, $11 \times 11 \times 11$, and $15 \times 15 \times 15$. Histograms and summary statistics for the $\mathrm{SAC}_{\mathrm{T1}}$ and $\mathrm{SAC}_{\mathrm{T2}}$ data are given along the top and right side of each plot.

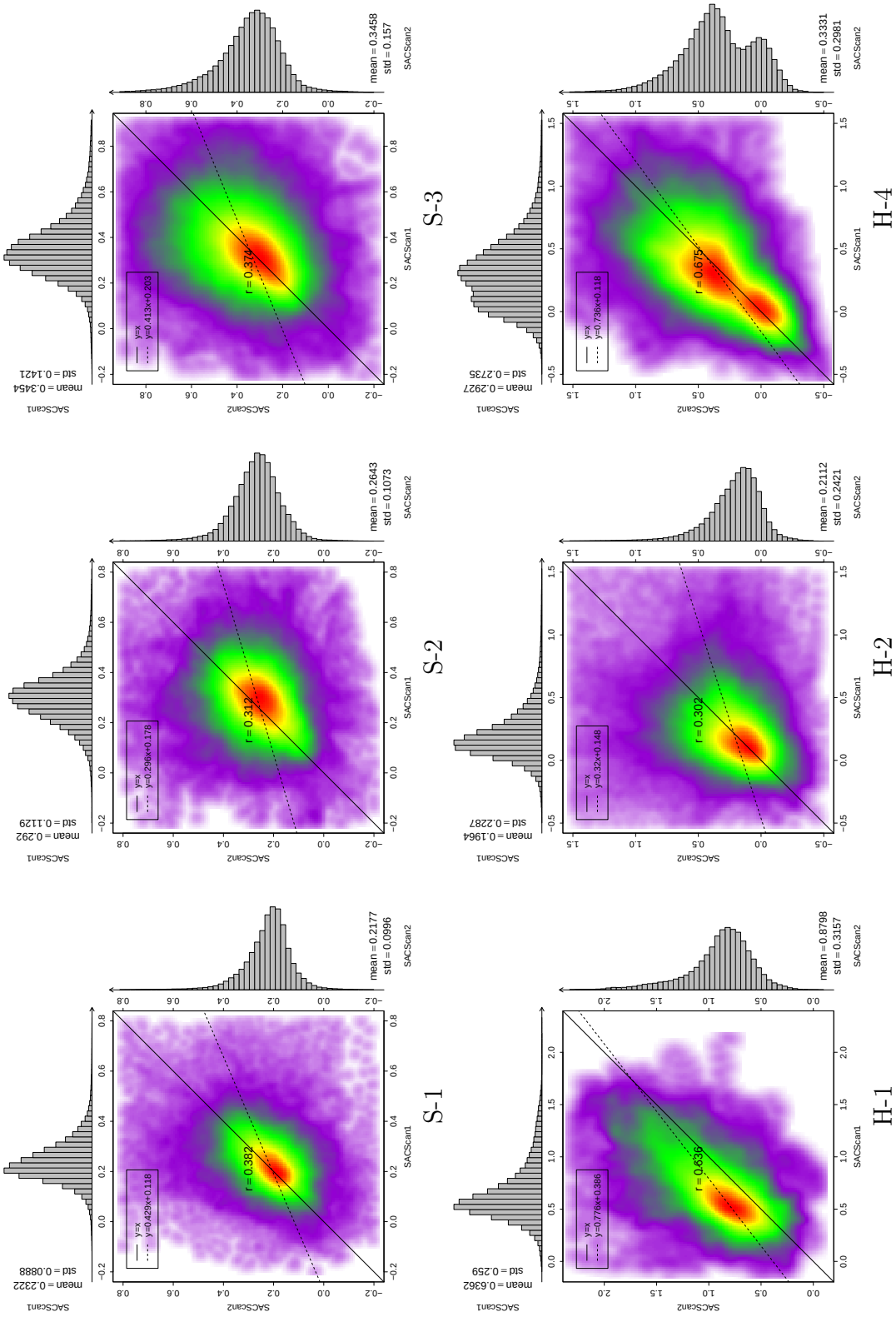

Figure A.12. SAC scatter plots for animal subjects and human subjects subjects.

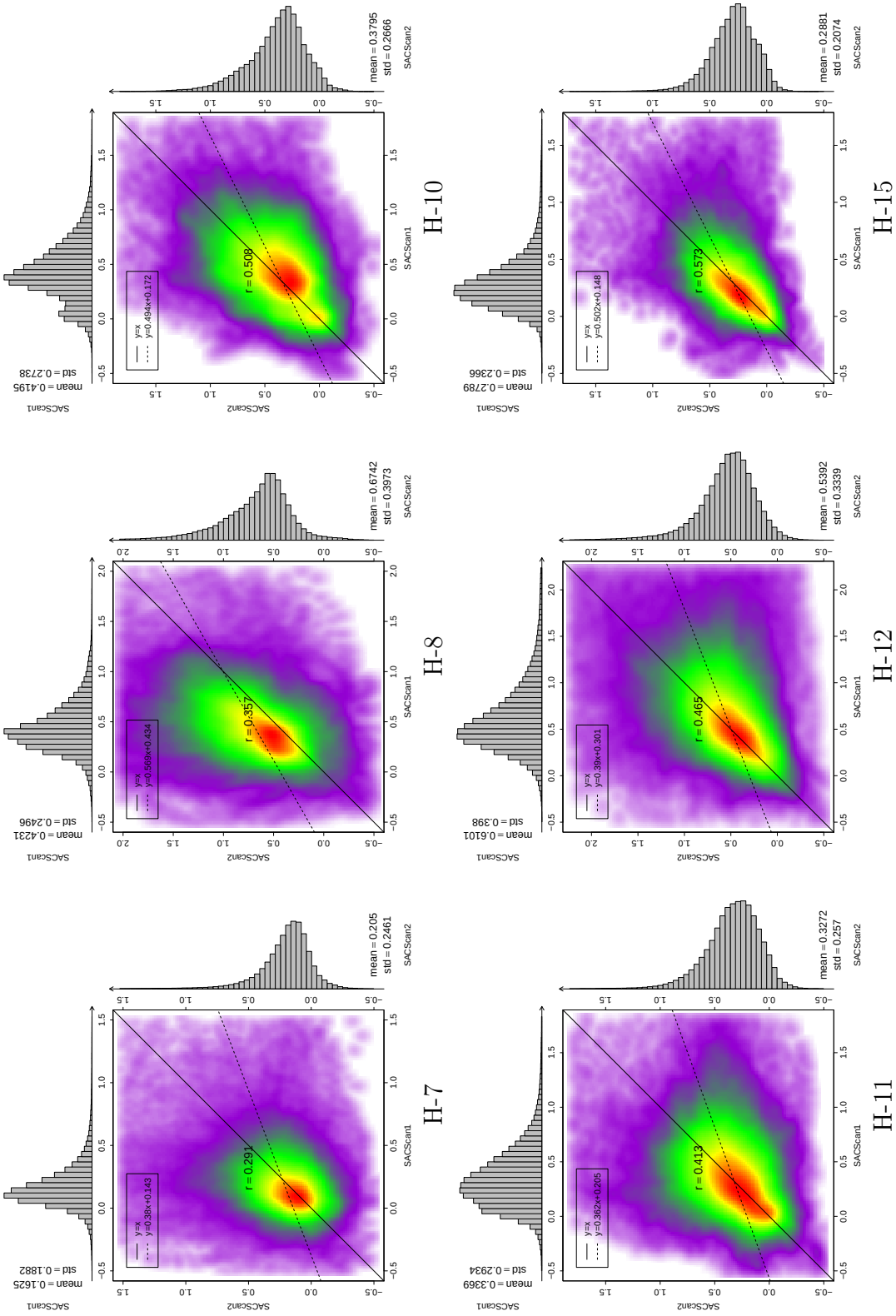

Figure A.13. SAC scatter plots for animal subjects and human subjects subjects (continue).

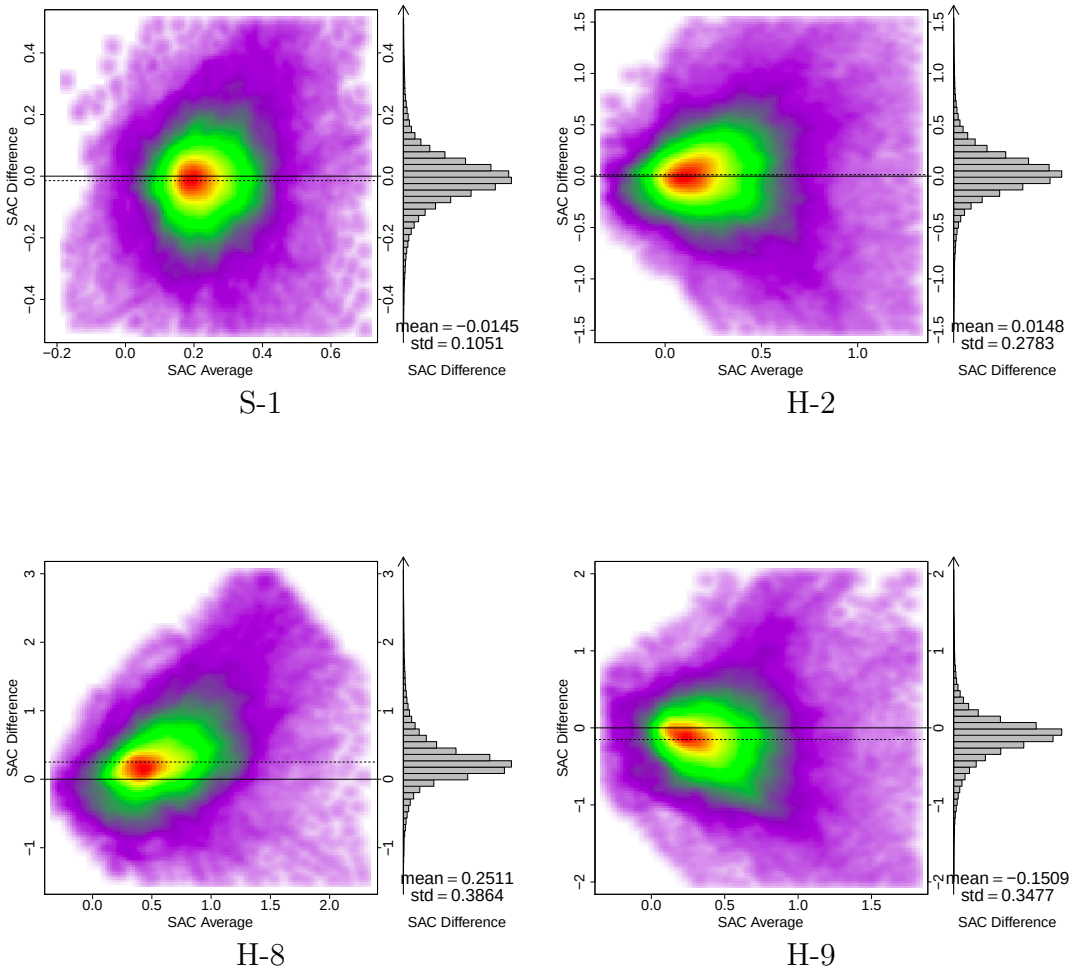

Figure A.14. SAC Bland-Altman plots for one typical animal subject S-1 and three typical human subjects H-2, H-8, H-9.

APPENDIX B

SUPPLEMENTAL EFFORT CORRECTION RESULTS

B.1 Improvement of reproducibility

Figure B.1 shows the improvement of reproducibility which is characterized by reduced MSE and increased gamma pass rate. It can observed that the improvement of reproducibility is more significant for subjects with larger tidal volume difference between scan one and two. We can also notice that if the tidal volume difference is less than 150 cc, the effect of global normalization is close to ETV and ELV, and ETV or ELV may deteriorate the reproducibility.

In addition to the MSE and gamma pass rate shown in Figure 4.14 in Chapter 4, Figure B.2 shows the relationship between the tidal volume difference in two scans and the change of reproducibility after global normalization, after ETV and/or ELV, presented with two additional reproducibility parameters such as mean and coefficient of variation (CV) of $\mathrm{JAC}_{\mathrm{RATIO}}$ map. The horizontal axis is tidal volume difference in liters. Mathematically the CV of $\mathrm{JAC}_{\mathrm{RATIO}}$ does not change after global normalization, therefore it is not shown in figure B.2 (b). The improvement of reproducibility manifests itself in the ways of closeness of $\mathrm{JAC}_{\mathrm{RATIO}}$ mean and one, and reduced CV.

In addition to the gamma pass rate curves for subject H-8 shown in Figure 4.13 (b) in Chapter 4, Figure B.3 summarizes the averaged gamma pass rate curves for before correction, after ETV correction, and after ELV correction, for all subjects (shown in (a)) and the subjects that had tidal volume difference greater than 100 cc

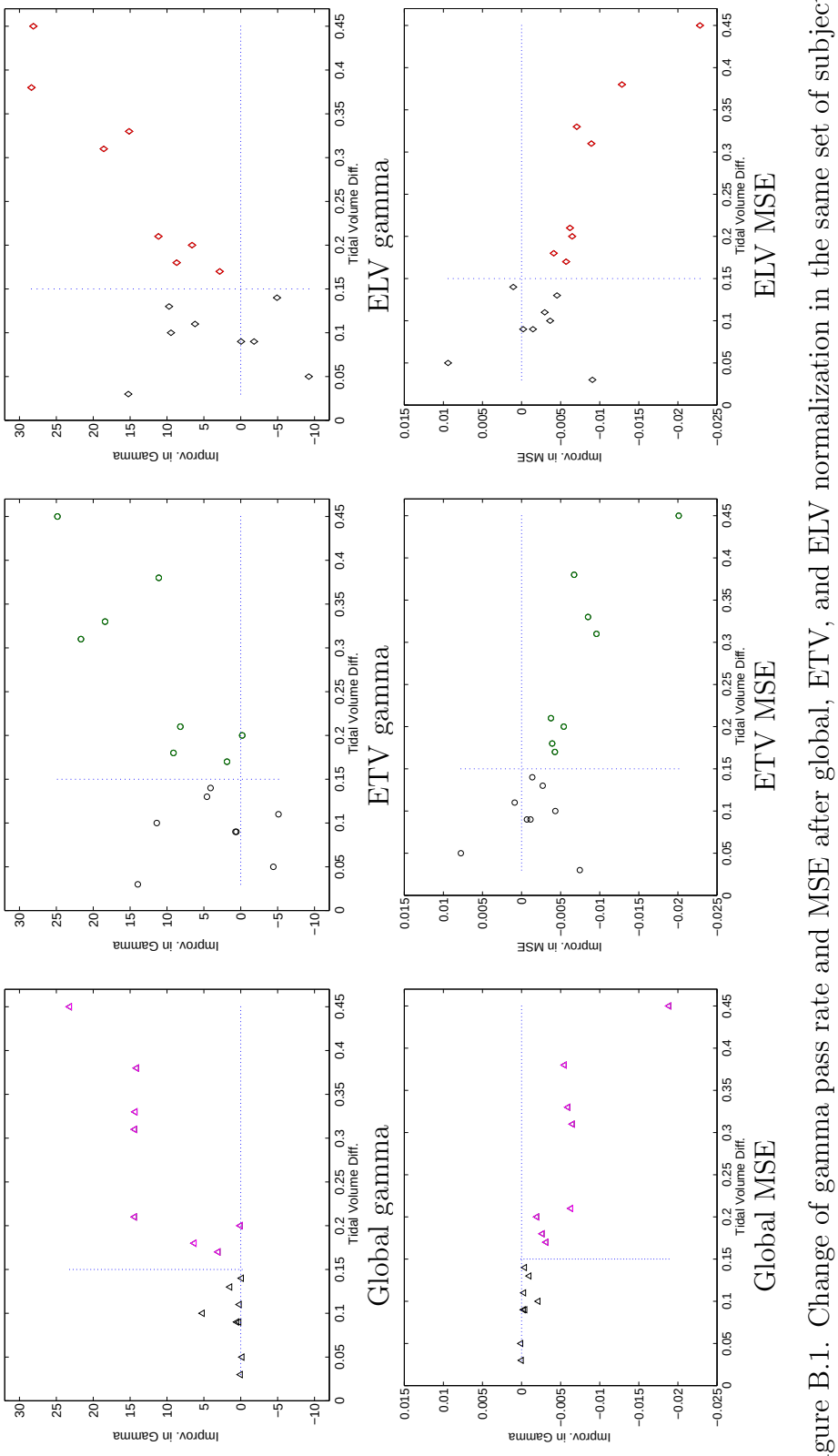

Figure B.1. Change of gamma pass rate and MSE after global, ETV, and ELV normalization in the same set of subjects.

(shown in (b)). Additionally, Figure B.4, B.5, B.6 and B.7 list the gamma pass rate curves for each subject.

Figure B.8 shows lobar tissue expansion pattern from EE to each respiratory phase, for both scans of subject H-9. Average tissue expansion from EE to each respiratory phase for each lobe and the whole lung is shown in (a) (for scan one) and (c) (for scan two). Tissue expansion for lobes LU, LL, RU, RM, relative to lobe RL is shown in (b) (for scan one) and (d) (for scan two). These results demonstrates that the ventilation rate is not uniform throughout the lung, not even at the lobar level. The ventilation rate for the left lower lobe is similar to the right lower lobe, but the upper and middle lobes show more heterogeneous air filling rates.

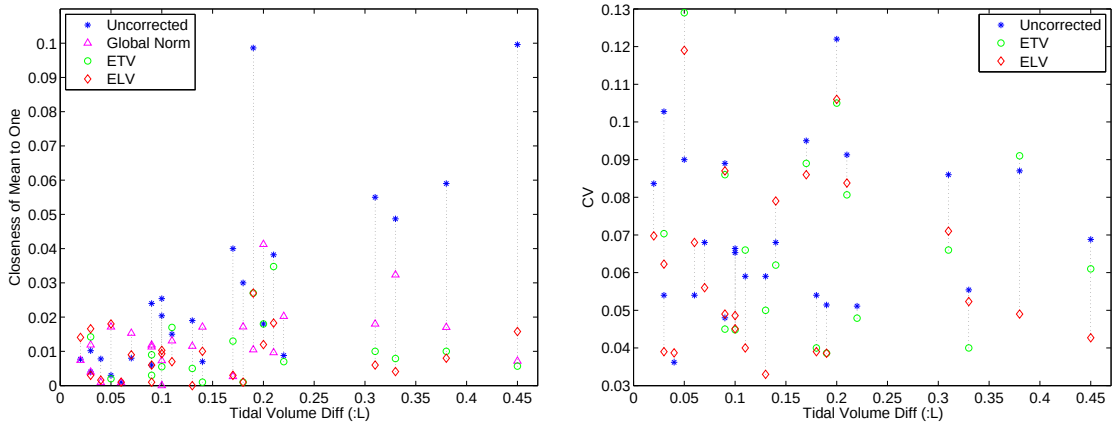

(a) (b)

Figure B.2. Relationship between the tidal volume difference in two scans and the change of reproducibility after global normalization, after ETV and/or ELV, presented with two reproducibility parameters as mean and coefficient of variation (CV) of JAC_{RATIO} map. The horizontal axis is tidal volume difference in liters. (a) Mean of JAC_{RATIO}. (b) CV of JAC_{RATIO}.

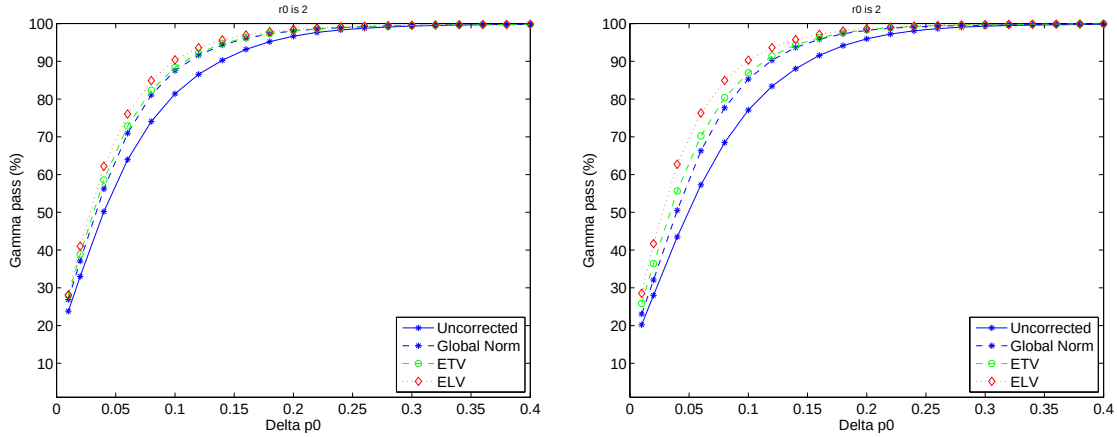

(a) (b)

Figure B.3. Averaged gamma pass rate curves for before correction, after ETV correction, and after ELV correction. (a) For all subjects. (b) For the subjects that had tidal volume difference greater than 100 cc.

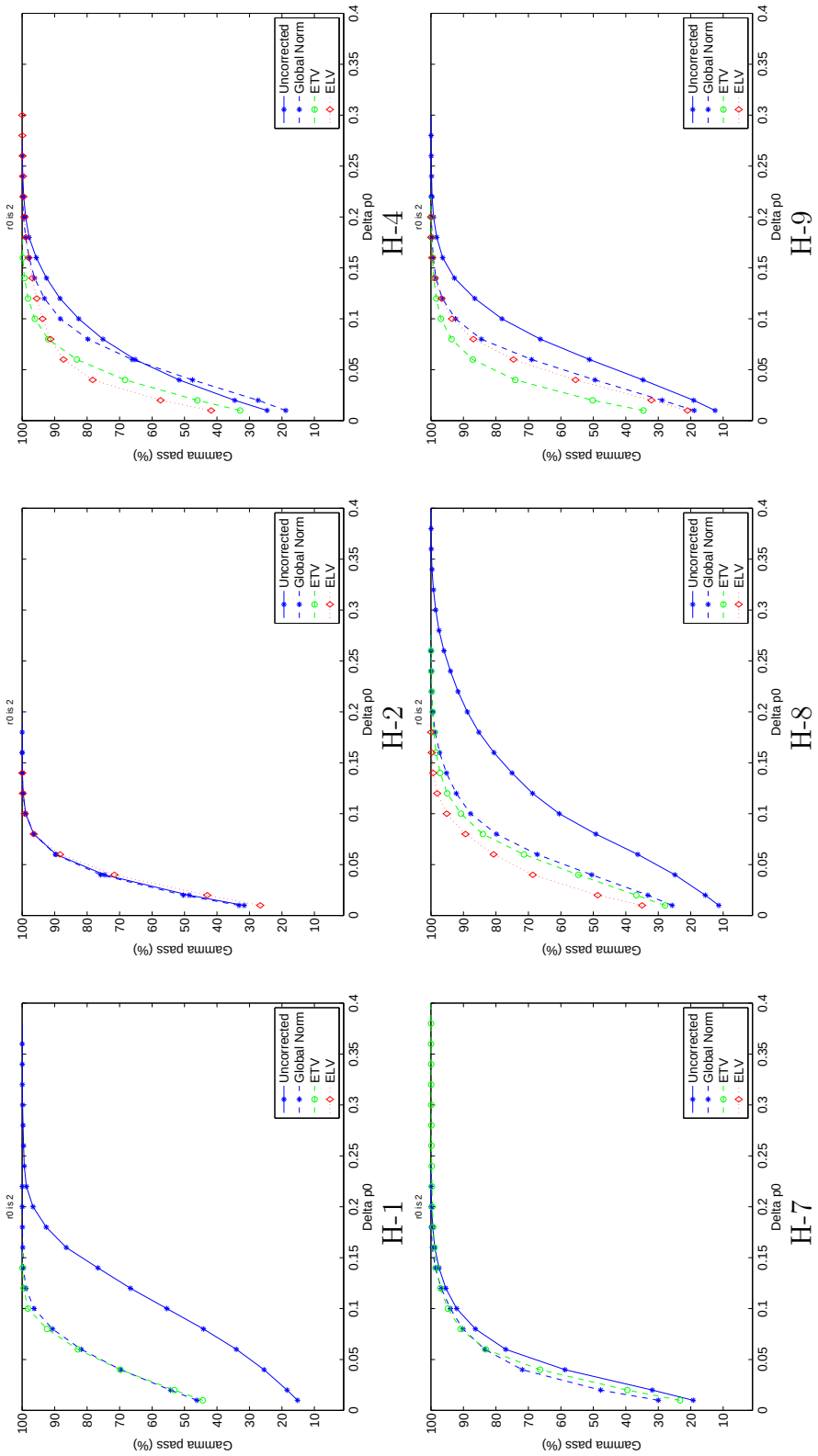

Figure B.4. Gamma pass rate curves before correction, after global, ETV, and ELV normalization for each subject.

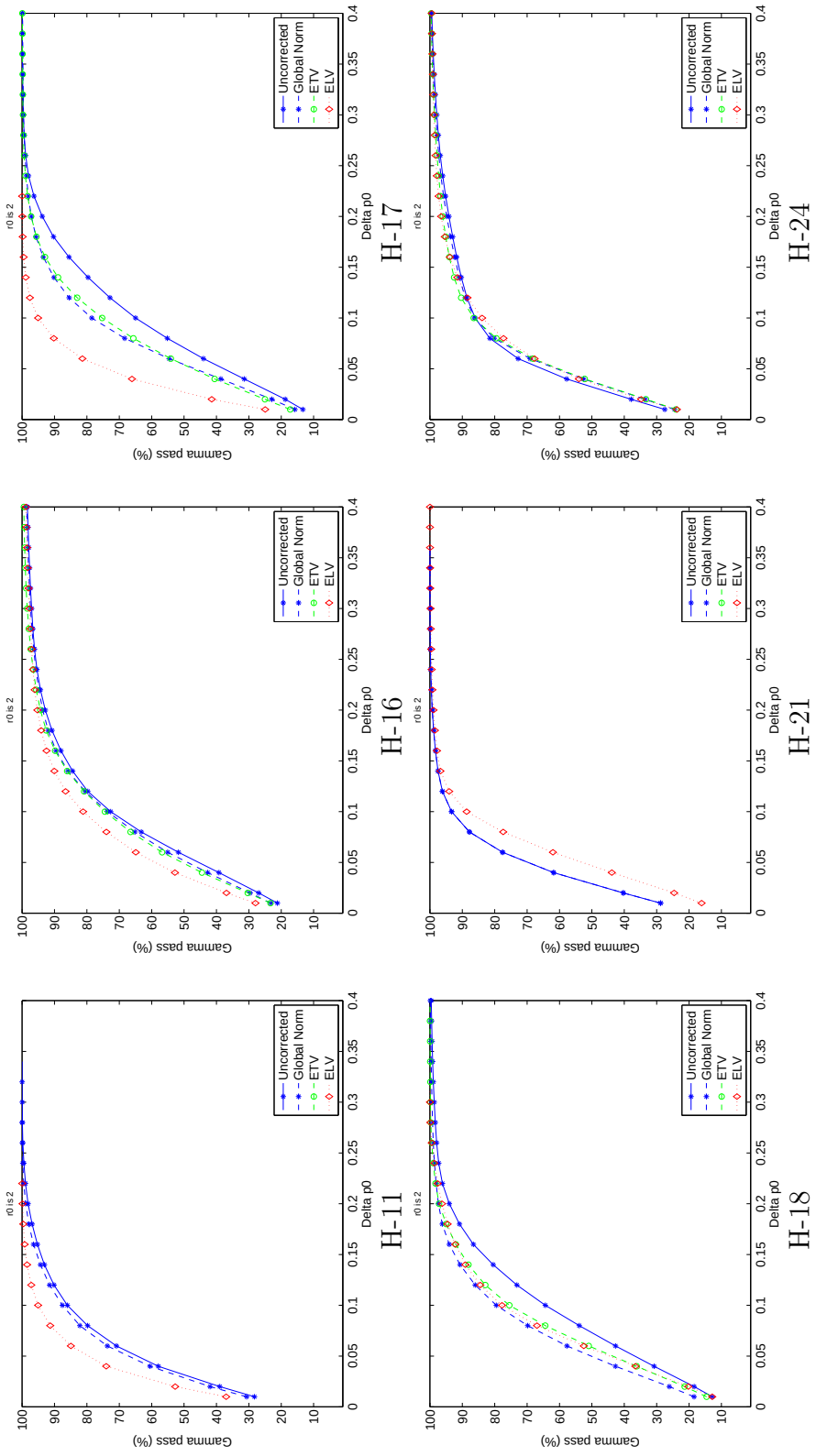

Figure B.5. Gamma pass rate curves before correction, after global, ETV, and ELV normalization for each subject (continue).

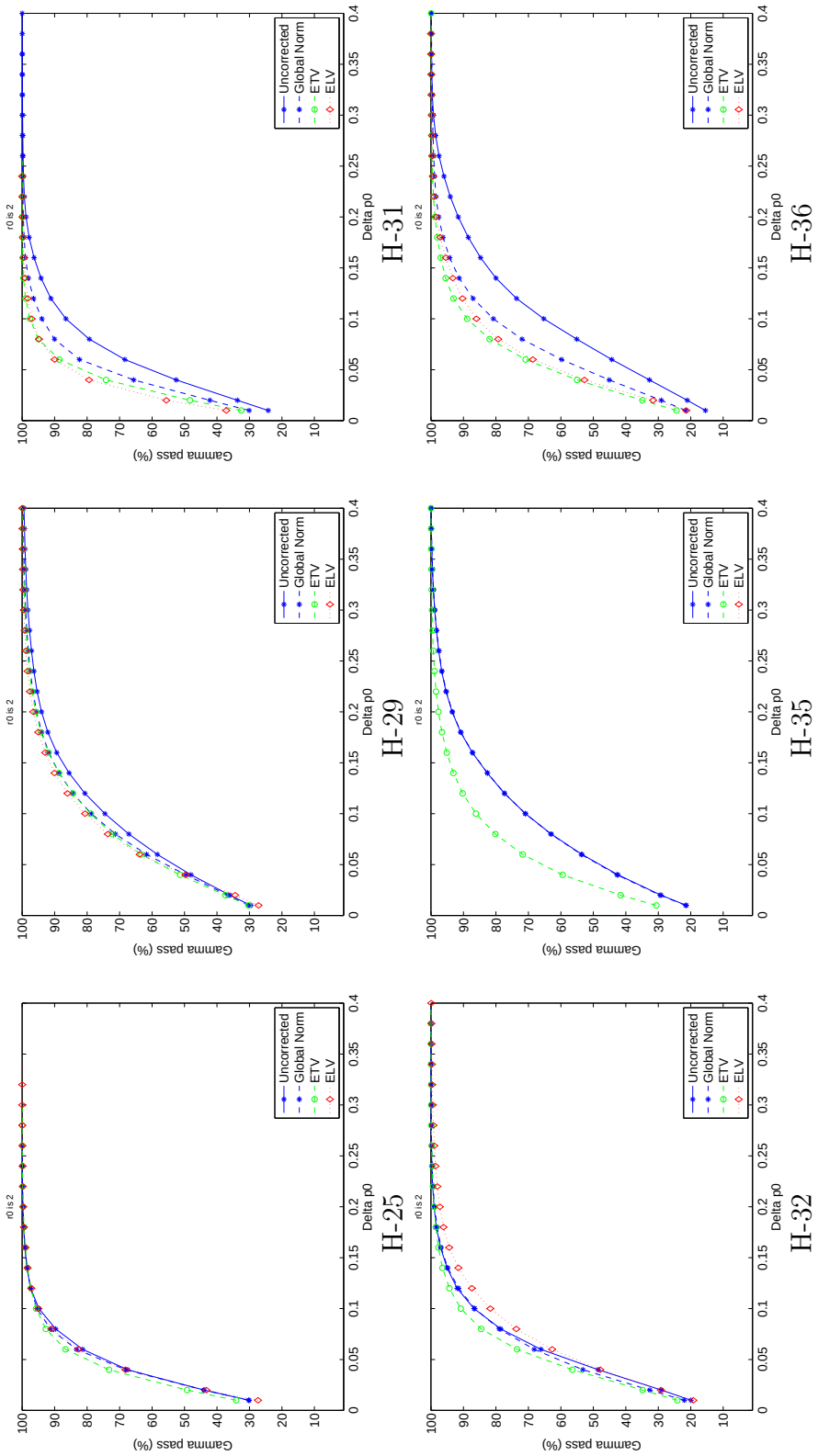

Figure B.6. Gamma pass rate curves before correction, after global, ETV, and ELV normalization for each subject (continue).

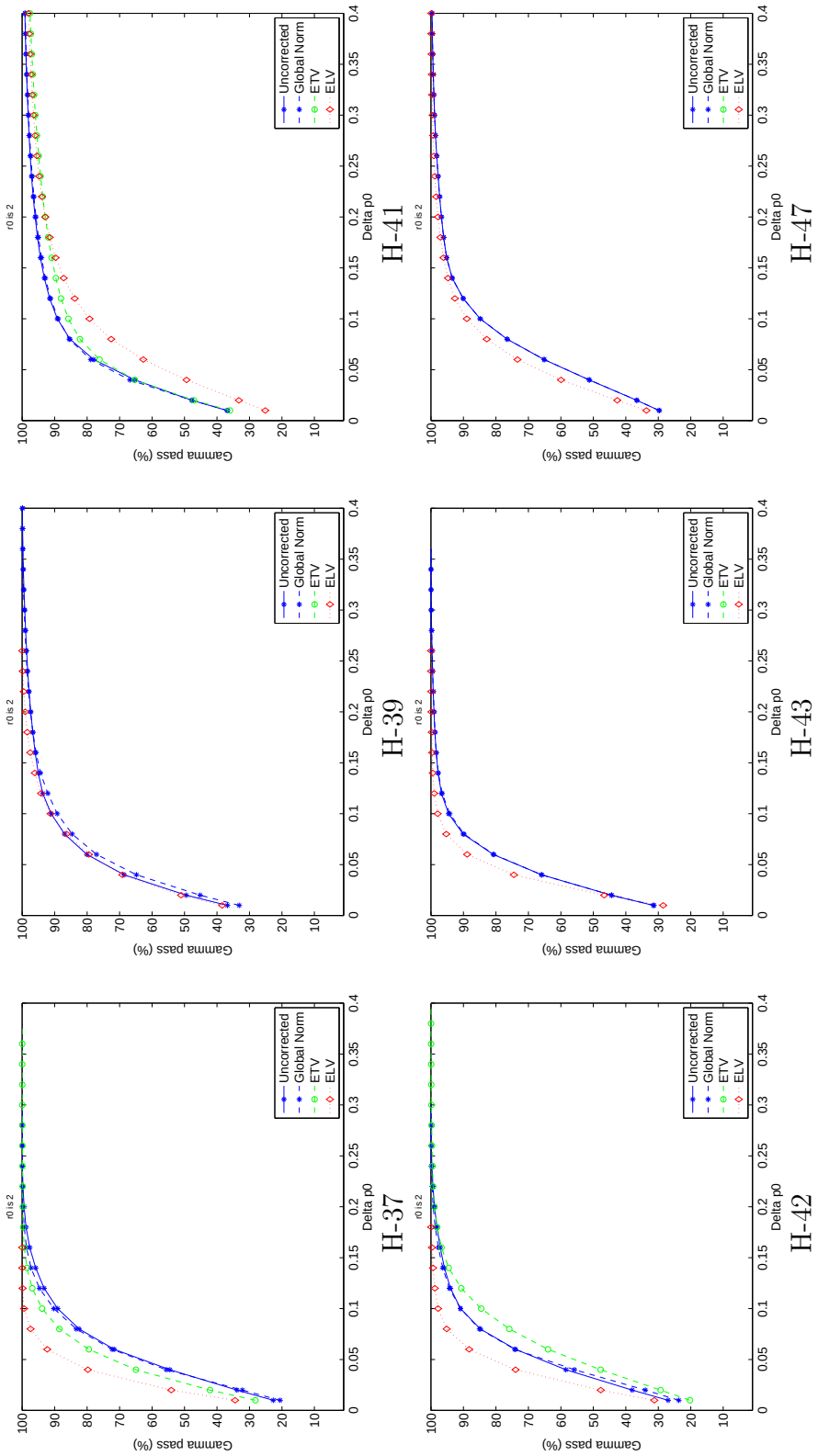

Figure B.7. Gamma pass rate curves before correction, after global, ETV, and ELV normalization for each subject (continue).

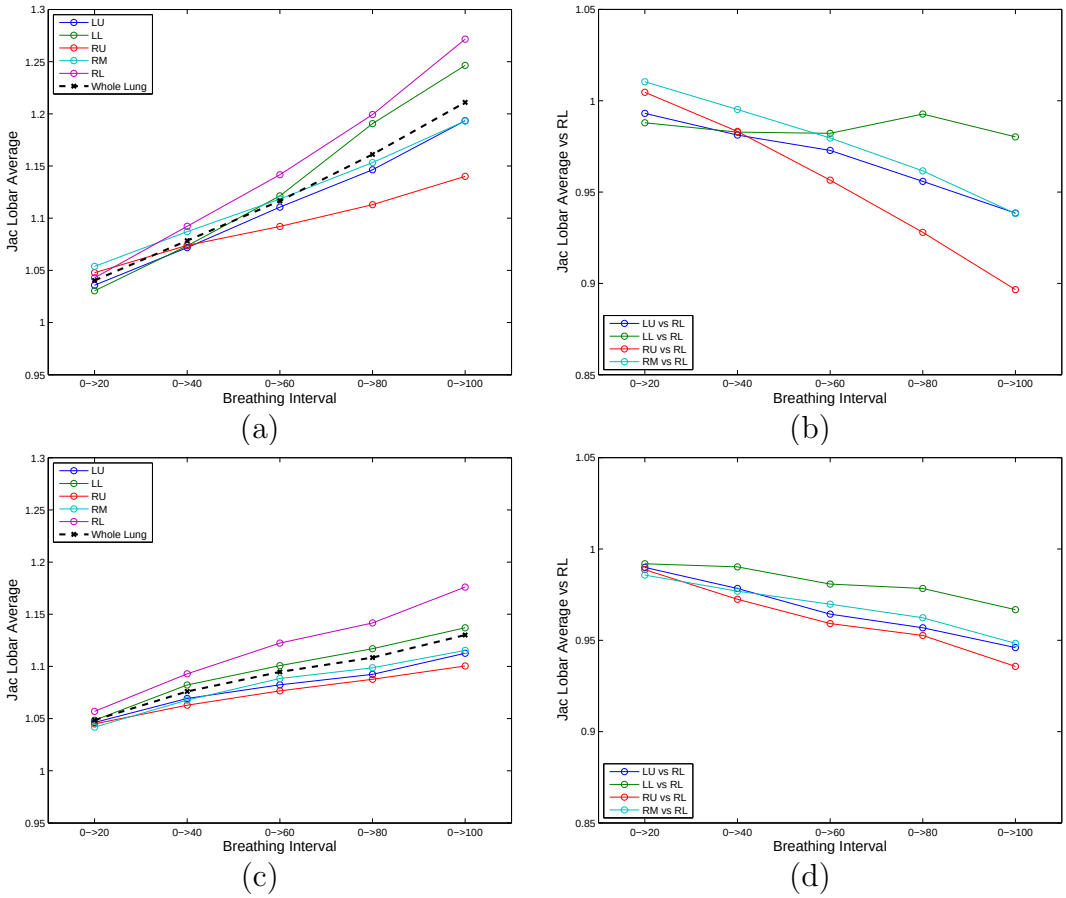

Figure B.8. Lobar tissue expansion pattern from EE to each respiratory phase. (a) Scan one average tissue expansion from EE to each respiratory phase for each lobe and the whole lung. (b) Scan one tissue expansion for lobes LU, LL, RU, RM, relative to lobe RL. (c) Scan two average tissue expansion from EE to each respiratory phase for each lobe and the whole lung. (d) Scan two tissue expansion for lobes LU, LL, RU, RM, relative to lobe RL.

APPENDIX C

DERIVATION OF INTENSITY-BASED VENTILATION

C.1 Alternate derivation of intensity-based Jacobian

First we are going to show the alternate derivation of Equation 3.6. From the definition of SAC, we have,

$$\begin{aligned} \text{SAC} &= \frac{\Delta V_{\text{air}}}{V_{\text{air},1}} \\ &= \frac{V_{\text{air},2} - V_{\text{air},1}}{V_{\text{air},1}} \\ &= \frac{V_{\text{air},2}}{V_{\text{air},1}} - 1 \\ &= \frac{V_2 f_2}{V_1 f_1} - 1 \end{aligned}$$

If we define the volume ratio, VR, as

$$\text{VR} = \frac{V_2}{V_1},$$

We can get the same result as Equation 3.6:

$$\text{SAC} + 1 = \frac{f_2}{f_1}\,\text{VR}$$

We can explore further about this. From Simon's and Hoffman's work [12, 107, 108], if we assume that there is no tissue volume change between conditions 1 and 2, then $V_{\text{tissue}} = V_{\text{tissue},1} = V_{\text{tissue},2}$, we have

$$\begin{aligned} f_1 &= \frac{\text{HU}_{\text{tissue}} - \text{HU}_1}{\text{HU}_{\text{tissue}} - \text{HU}_{\text{air}}} \\ f_2 &= \frac{\text{HU}_{\text{tissue}} - \text{HU}_2}{\text{HU}_{\text{tissue}} - \text{HU}_{\text{air}}} \end{aligned}$$

then from Equation C.1, we have

$$\mathrm{SAC}+1=\frac{\mathrm{HU}_{\mathrm{tissue}}-\mathrm{HU}_2}{\mathrm{HU}_{\mathrm{tissue}}-\mathrm{HU}_1}\,\mathrm{VR}$$

If we assume the air is -1000 HU and the tissue is 0 HU, then

$$\mathrm{SAC}+1=\frac{\mathrm{HU}_2}{\mathrm{HU}_1}\,\mathrm{VR}$$

Secondly we will show the alternate derivation of Equation 3.9. If we assume $V_{\mathrm{tissue}}=V_{\mathrm{tissue},1}=V_{\mathrm{tissue},2}$, then

$$\begin{aligned}
\mathrm{VR} &= \frac{V_2}{V_1}\\
&= \frac{V_{\mathrm{tissue}}+V_{\mathrm{air},2}}{V_{\mathrm{tissue}}+V_{\mathrm{air},1}}\\
&= \frac{1+\frac{V_{\mathrm{air},2}}{V_{\mathrm{tissue}}}}{1+\frac{V_{\mathrm{air},1}}{V_{\mathrm{tissue}}}}\\
&= \frac{1+\frac{V_2(-\frac{\mathrm{HU}_2}{1000})}{V_2(1-(-\frac{\mathrm{HU}_2}{1000}))}}{1+\frac{V_1(-\frac{\mathrm{HU}_1}{1000})}{V_1(1-(-\frac{\mathrm{HU}_1}{1000}))}}\\
&= \frac{1000+\mathrm{HU}_1}{1000+\mathrm{HU}_2},
\end{aligned}$$

which is exactly the same as Equation 3.9.

APPENDIX D

ANALYTICAL ANALYSIS OF NOISE

D.1 Intensity-based SAC

The propagation of errors for the general function $x = f(u, v)$, is given by the relation [111]:

$$\sigma_x^2 = \sigma_u^2 \left(\frac{\partial x}{\partial u}\right)^2 + \sigma_v^2 \left(\frac{\partial x}{\partial v}\right)^2 + 2\sigma_{uv}^2 \left(\frac{\partial x}{\partial u}\right)\left(\frac{\partial x}{\partial v}\right) \tag{D.1}$$

We can evaluate the propagation of CT image noise to the noise of intensity-based SAC using Equation D.1. To simplify the analysis, we assume the transformation from the fixed image to the moving image is the identity transformation. Since I_f and I_m are measurements obtained from two separate acquisitions, they can be assumed to be independent, and thus the covariance term in Equation D.1 is zero [111]. In fact, even if I_f and I_m are not truly independent, the covariance terms are usually one to two orders of magnitude smaller than the variance terms [111].

From Equation 3.3, if we let $u = I_f$, $v = I_m$, and $x = \frac{\Delta V}{V_f}$, then we have:

$$x = \frac{1000(v-u)}{u(v+1000)},$$

and then,

$$\begin{aligned} \frac{\partial x}{\partial u} &= \frac{-1000u(v+1000) - 1000(v-u)(v+1000)}{(u(v+1000))^2} \\ &= \frac{-1000v}{u^2(v+1000)}, \end{aligned}$$

and,

$$\begin{aligned}\frac{\partial x}{\partial v} &= \frac{1000u(v+1000)-1000(v-u)u}{(u(v+1000))^2} \\ &= \frac{1000(u+1000)}{u(v+1000)^2}.\end{aligned}$$

If we assume the CT noise variance in the fixed image and the moving image to be the same, we have $\sigma_u^2 = \sigma_v^2 = \sigma_{\text{CT}}^2$, and,

$$\begin{aligned}\sigma_{\text{SAC}}^2 = \sigma_x^2 &= \sigma_u^2\left(\frac{\partial x}{\partial u}\right)^2 + \sigma_v^2\left(\frac{\partial x}{\partial v}\right)^2 \\ &= \sigma_{\text{CT}}^2\left(\left(\frac{\partial x}{\partial u}\right)^2 + \left(\frac{\partial x}{\partial v}\right)^2\right) \\ &= \sigma_{\text{CT}}^2\left(1000^2\frac{u^2(u+1000)^2 + v^2(v+1000)^2}{u^4(v+1000)^4}\right).\end{aligned}$$

The impact of CT noise on the coefficient of variation (CV) of SAC is:

$$\begin{aligned}\frac{\sigma_x}{\mu_x} &= \frac{\sigma_{\text{CT}}\sqrt{1000^2\frac{u^2(u+1000)^2+v^2(v+1000)^2}{u^4(v+1000)^4}}}{\frac{1000(v-u)}{u(v+1000)}} \\ &= \sigma_{\text{CT}}\frac{\sqrt{u^2(u+1000)^2 + v^2(v+1000)^2}}{u(v-u)(v+1000)}.\end{aligned}$$

D.2 Intensity-based Jacobian

Similar to the analytical analysis of noise in intensity-based SAC in Appendix D.1, we can use the same error propagation theory on intensity-based Jacobian. Similarly, we assume the transformation from the fixed image to the moving image is the identity transformation to ignore the covariance term in Equation D.1. From Equation 3.9, if we let $u = I_f$, $v = I_m$, and use IJAC as the intensity-based Jacobian, then we have:

$$\text{IJAC} = \frac{u+1000}{v+1000},$$

and then,

$$\frac{\partial \text{IJAC}}{\partial u} = \frac{1}{v+1000}$$

and,

$$\begin{aligned}\frac{\partial \text{IJAC}}{\partial v} &= \frac{(v+1000)-(u+1000)}{(v+1000)^2} \\ &= \frac{v-u}{(v+1000)^2}.\end{aligned}$$

If we assume the CT noise variance in the fixed image and the moving image to be the same, we have $\sigma_u^2 = \sigma_v^2 = \sigma_{\text{CT}}^2$, and,

$$\begin{aligned}\sigma_{\text{IJAC}}^2 &= \sigma_u^2\left(\frac{\partial \text{IJAC}}{\partial u}\right)^2 + \sigma_v^2\left(\frac{\partial \text{IJAC}}{\partial v}\right)^2 \\ &= \sigma_{\text{CT}}^2\left(\left(\frac{\partial \text{IJAC}}{\partial u}\right)^2 + \left(\frac{\partial \text{IJAC}}{\partial v}\right)^2\right) \\ &= \sigma_{\text{CT}}^2\left(\frac{(v+1000)^2+(v-u)^2}{(v+1000)^4}\right).\end{aligned}$$

The impact of CT noise on the coefficient of variation (CV) of IJAC is:

$$\begin{aligned}\frac{\sigma_{\text{IJAC}}}{\mu_{\text{IJAC}}} &= \frac{\sigma_{\text{CT}}\sqrt{\frac{(v+1000)^2+(v-u)^2}{(v+1000)^4}}}{\frac{u+1000}{v+1000}} \\ &= \sigma_{\text{CT}}\frac{\sqrt{(v+1000)^2+(v-u)^2}}{(u+1000)(v+1000)}.\end{aligned}$$

REFERENCES

[1] J. Lubliner, *Plasticity Theory*. Mineola, NY: Dover Publication, 2008.

[2] K. Ding, *Regional lung function and mechanics using image registration*. PhD thesis, University of Iowa, 2010.

[3] G. Zhang, T. J. Dilling, C. W. Stevens, and K. M. Forster, "Functional lung imaging in thoracic cancer radiotherapy," *Cancer Control*, vol. 15, no. 2, pp. 112–119, Apr 2008.

[4] A. C. Society, *Cancer facts & figures*. American Cancer Society, Atlanta, GA, 2010.

[5] K. Latifi, *Assessment of the Dependence of Ventilation Image Calculation from 4D-CT on Deformation and Ventilation Algorithms*. PhD thesis, University of South Florida, 2011.

[6] F. M. Kong, R. K. Ten Haken, M. J. Schipper, M. A. Sullivan, M. Chen, C. Lopez, G. P. Kalemkerian, and J. A. Hayman, "High-dose radiation improved local tumor control and overall survival in patients with inoperable/unresectable non-small-cell lung cancer: long-term results of a radiation dose escalation study," *Int. J. Radiat. Oncol. Biol. Phys.*, vol. 63, no. 2, pp. 324–333, Oct 2005.

[7] B. P. Yaremko, T. M. Guerrero, J. Noyola-Martinez, R. Guerra, D. G. Lege, L. T. Nguyen, P. A. Balter, J. D. Cox, and R. Komaki, "Reduction of normal lung irradiation in locally advanced non-small-cell lung cancer patients, using ventilation images for functional avoidance," *Int. J. Radiat. Oncol. Biol. Phys.*, vol. 68, no. 2, pp. 562–571, Jun 2007.

[8] M. V. Graham, J. A. Purdy, B. Emami, W. Harms, W. Bosch, M. A. Lockett, and C. A. Perez, "Clinical dose-volume histogram analysis for pneumonitis after 3D treatment for non-small cell lung cancer (NSCLC)," *Int. J. Radiat. Oncol. Biol. Phys.*, vol. 45, no. 2, pp. 323 – 329, 1999.

[9] S. L. Kwa, J. V. Lebesque, J. C. Theuws, L. B. Marks, M. T. Munley, G. Bentel, D. Oetzel, U. Spahn, M. V. Graham, R. E. Drzymala, J. A. Purdy, A. S. Lichter, M. K. Martel, and R. K. T. Haken, "Radiation pneumonitis as a function of mean lung dose: An analysis of pooled data of 540 patients," *Int. J. Radiat. Oncol. Biol. Phys.*, vol. 42, no. 1, pp. 1 – 9, 1998.

[10] L. B. Marks, S. M. Bentzen, J. O. Deasy, F. M. Kong, J. D. Bradley, I. S. Vogelius, I. El Naqa, J. L. Hubbs, J. V. Lebesque, R. D. Timmerman, M. K. Martel, and A. Jackson, "Radiation dose-volume effects in the lung," *Int. J. Radiat. Oncol. Biol. Phys.*, vol. 76, no. 3 Suppl, pp. S70–76, Mar 2010.

[11] J. M. Reinhardt, K. Ding, K. Cao, G. E. Christensen, E. A. Hoffman, and S. V. Bodas, "Registration-based estimates of local lung tissue expansion compared to xenon CT measures of specific ventilation," *Medical Image Analysis*, vol. 12, no. 6, pp. 752 – 763, 2008.

[12] B. A. Simon, "Non-invasive imaging of regional lung function using X-Ray computed tomography," *Journal Of Clinical Monitoring and Computing*, vol. 16(5), pp. 433–442, 2000.

[13] T. Guerrero, K. Sanders, J. Noyola-Martinez, E. Castillo, Y. Zhang, R. Tapia, R. Guerra, Y. Borghero, and R. Komaki, "Quantification of regional ventilation from treatment planning CT," *Int. J. Radiat. Oncol. Biol. Phys.*, vol. 62, no. 3, pp. 630 – 634, 2005.

[14] R. Castillo, E. Castillo, J. Martinez, and T. Guerrero, "Ventilation from four-dimensional computed tomography: density versus Jacobian methods," *Physics in Medicine and Biology*, vol. 55(16), pp. 4661–4685, 2010.

[15] K. Ding, J. E. Bayouth, J. M. Buatti, G. E. Christensen, and J. M. Reinhardt, "4DCT-based measurement of changes in pulmonary function following a course of radiation therapy," *Med. Phys.*, vol. 37(3), pp. 1261–1273, 2010.

[16] S. S. Watharkar, "Attenuation based quantification of interstitial lung disease using high resolution computed tomography and correlation with pulmonary function tests," 2010.

[17] M. Ward and P. T. Macklem, "The act of breathing and how it fails," *Chest*, vol. 97, no. 3 suppl, pp. 36s–39s, Mar 1990.

[18] J. Bates, *Lung Mechanics: An Inverse Modeling Approach*. Cambridge University Press, 2009.

[19] J. B. West, "Ventilation/blood flow and gas exchange," 1977.

[20] L. Mathew, *Quantification of Pulmonary Ventilation using Hyperpolarized 3He Magnetic Resonance Imaging*. PhD thesis, The University of Western Ontario, London, Ontario, Canada, 2011.

[21] P. Pratt, *Emphysema and chronic airways disease*, pp. 654–659. Springer-Verlag, 1998. edited by D. Dail and S. Hammar.

[22] L. Sarna, L. Evangelista, D. Tashkin, G. Padilla, C. Holmes, M. L. Brecht, and F. Grannis, "Impact of respiratory symptoms and pulmonary function on quality of life of long-term survivors of non-small cell lung cancer," *Chest*, vol. 125, pp. 439–445, 2004.

[23] J. S. Temel, W. F. Pirl, and T. J. Lynch, "Comprehensive symptom management in patients with advanced-stage non-small-cell lung cancer," *Clin Lung Cancer*, vol. 7, no. 4, pp. 241–249, Jan 2006.

[24] V. R. Shannon, "Role of pulmonary rehabilitation in the management of patients with lung cancer," *Curr Opin Pulm Med*, vol. 16, no. 4, pp. 334–339, Jul 2010.

[25] B. Movsas, T. A. Raffin, A. H. Epstein, and C. J. Link, "Pulmonary radiation injury," *Chest*, vol. 111, no. 4, pp. 1061–1076, Apr 1997.

[26] S. L. Faria, M. Aslani, F. S. Tafazoli, L. Souhami, and C. R. Freeman, "The challenge of scoring radiation-induced lung toxicity," *Clin Oncol (R Coll Radiol)*, vol. 21, no. 5, pp. 371–375, Jun 2009.

[27] V. Mehta, "Radiation pneumonitis and pulmonary fibrosis in non-small-cell lung cancer: Pulmonary function, prediction, and prevention," *Int. J. Radiat. Oncol. Biol. Phys.*, vol. 63, no. 1, pp. 5 – 24, 2005.

[28] P. Rubin and G. W. Casarett, "Clinical radiation pathology as applied to curative radiotherapy," *Cancer*, vol. 22, no. 4, pp. 767–778, Oct 1968.

[29] N. Takabatake, S. Toriyama, Y. Takeishi, Y. Shibata, T. Konta, S. Inoue, S. Abe, A. Igarashi, Y. Tokairin, M. Ishii, *et al.*, "A nonfunctioning single nucleotide polymorphism in olfactory receptor gene family is associated with the forced expiratory volume in the first second/the forced vital capacity values of pulmonary function test in a japanese population," *Biochemical and biophysical research communications*, vol. 364, no. 3, pp. 662–667, 2007.

[30] http://www.pennmedicine.org/health_info/asthma/000154.html.

[31] Anaethesia, FRCA. http://www.frca.co.uk/.

[32] E. Hoffman, T. Behrenbeck, P. Chevalier, and E. Wood, "Estimation of pleural surface expansile forces in intact dogs," *Journal of Applied Physiology*, vol. 55(3), pp. 935–948, 1983.

[33] H. Robertson, R. Glenny, D. Stanford, L. Mclnnes, D. Luchtel, and D. Covert, "High-resolution maps of regional ventilation utilizing inhaled fluorescent microspheres," *Journal of Applied Physiology*, vol. 82(3), pp. 943–953, 1997.

[34] R. D. Hubmayr, W. Bosch, P. Chevalier, J. R. Rodarte, and L. Olson, "Topographical distribution of regional lung volume in anesthetized dogs," *Journal of Applied Physiology*, vol. 54(4), pp. 1048–1056, 1983.

[35] D. P. Schuster, "Positron emission tomography: theory and its application to the study of lung disease," *Am. Rev. Respir. Dis.*, vol. 139, pp. 818–40, 1989.

[36] T. Wellman, T. Winkler, E. Costa, G. Musch, R. S. Harris, J. G. Venegas, and M. F. V. Melo, "Measurement of regional specific lung volume change using respiratory-gated PET of inhaled 13N-nitrogen," *J. Nucl. Med.*, vol. 51, pp. 646–53, 2010.

[37] R. S. Harris and D. P. Schuster, "Visualizing lung function with positron emission tomography," *J Appl Physiol*, vol. 102, no. 1, pp. 448–458, 2007.

[38] J. G. Venegas, T. Winkler, G. Musch, M. F. V. Melo, D. Layfield, N. Tgavalekos, A. J. Fischman, R. J. Callahan, G. Bellani, and R. S. Harris, "Self-organized patchiness in asthma as a prelude to catastrophic shifts," *Nature*, vol. 7034, no. 2-3, pp. 777–782, 2005.

[39] H. E. Moller, X. J. Chen, B. Saam, K. D. Hagspiel, G. A. Johnson, T. A. Altes, E. E. de Lange, and H.-U. Kauczor, "MRI of the lungs using hyperpolarized noble gases," *Magnetic Resonance in Medicine*, vol. 47, no. 6, pp. 1029–1051, 2002.

[40] J. M. Wild, M. N. Paley, L. Kasuboski, A. Swift, S. Fichele, N. Woodhouse, P. D. Griffiths, and E. J. van Beek, "Dynamic radial projection MRI of inhaled hyperpolarized 3He gas," *Magn Reson Med*, vol. 49, pp. 991–997, Jun 2003.

[41] E. J. van Beek, J. M. Wild, H.-U. Kauczor, W. Schreiber, J. P. M. III, and E. E. de Lange, "Functional MRI of the lung using hyperpolarized 3-helium gas," *Journal Of Magnetic Resonance Imaging*, vol. 20, no. 4, pp. 550–554, 2004.

[42] N. Woodhouse, J. Wild, M. N. Paley, S. Fichele, Z. Said, A. Swift, and E. J. R. van Beek, "Combined helium-3/proton magnetic resonance imaging measurement of ventilated lung volumes in smokers compared to never-smokers," *Journal of magnetic resonance imaging*, vol. 21(4), pp. 365–369, 2005.

[43] E. A. Hoffman and E. van Beek, "Hyperpolarized media MR imaging - expanding the boundaries?," *Academic Radiology*, vol. 13, no. 8, pp. 929–931, 2006.

[44] C. Marcucci, D. Nyhan, and B. A. Simon, "Distribution of pulmonary ventilation using Xe-enhanced computed tomography in prone and supine dogs," *J Appl Physiol*, vol. 90, no. 2, pp. 421–430, 2001.

[45] J. K. Tajik, D. Chon, C.-H. Won, B. Q. Tran, and E. A. Hoffman, "Subsecond multisection CT of regional pulmonary ventilation," *Academic Radiology*, vol. 9, pp. 130–146, 2002.

[46] D. Chon, B. A. Simon, K. C. Beck, H. Shikata, O. I. Saba, C. Won, and E. A. Hoffman, "Differences in regional wash-in and wash-out time constants for xenon-CT ventilation studies," *Respiratory Physiology & Neurobiology*, vol. 148, no. 1-2, pp. 65 – 83, 2005.

[47] T. Guerrero, K. Sanders, E. Castillo, Y. Zhang, L. Bidaut, and T. P. R. Komaki, "Dynamic ventilation imaging from four-dimensional computed tomography," *Phys Med Biol.*, vol. 51, no. 4, pp. 777–791, Feb. 21 2006.

[48] G. E. Christensen, J. H. Song, W. Lu, I. E. Naqa, and D. A. Low, "Tracking lung tissue motion and expansion/compression with inverse consistent image registration and spirometry.," *Med Physics*, vol. 34, no. 6, pp. 2155–2165, June 2007.

[49] M. K. Fuld, R. B. Easley, O. I. Saba, D. Chon, J. M. Reinhardt, E. A. Hoffman, and B. A. Simon, "CT-measured regional specific volume change reflects regional ventilation in supine sheep," *J Appl Physiol*, vol. 104, no. 4, pp. 1177–1184, 2008.

[50] T. Yamamoto, S. Kabus, T. Klinder, C. Lorenz, J. von Berg, T. Blaffert, B. W. L. Jr, and P. J. Keall, "Investigation of four-dimensional computed tomography-based pulmonary ventilation imaging in patients with emphysematous lung regions," *Physics in Medicine and Biology*, vol. 56, pp. 2279–2298, 2011.

[51] L. Mathew, A. Wheatley, R. Castillo, E. Castillo, G. Rodrigues, T. Guerrero, and G. Parraga, "Hyperpolarized (3)He Magnetic Resonance Imaging: Comparison with Four-dimensional X-ray Computed Tomography Imaging in Lung Cancer," *Acad Radiol*, vol. 19, no. 12, pp. 1546–1553, Dec 2012.

[52] D. Han, J. Bayouth, S. Bhatia, M. Sonka, and X. Wu, "Motion artifact reduction in 4d helical ct: Graph-based structure alignment," in *Medical Computer Vision. Recognition Techniques and Applications in Medical Imaging*, B. Menze, G. Langs, Z. Tu, and A. Criminisi, eds., vol. 6533 of *Lecture Notes in Computer Science*, pp. 63–73, Springer Berlin Heidelberg, 2011.

[53] Z. Luo, Z. Xi, J. Wang, and D. Tang, "Sorting 4DCT images based on manifold learning," in *Intelligent Computation Technology and Automation (ICICTA)*, vol. 2, pp. 181–185, 2008.

[54] K. Yuan, C. Duan, and Z. Tian, "A 4D CT sorting algorithm based on image boundary discontinuity," in *Medical Image Analysis and Clinical Applications (MIACA)*, pp. 147–150, 2010.

[55] G. Xiong, C. Chen, J. Chen, Y. Xie, and L. Xing, "Tracking the motion trajectories of junction structures in 4D CT images of the lung," *Phys Med Biol*, vol. 57, no. 15, pp. 4905–4930, Aug 2012.

[56] D. Han, J. E. Bayouth, S. Bhatia, M. Sonka, and X. Wu, "Motion artifact reduction in 4D helical CT: Graph-based structure alignment," in *MICCAI Workshop on Medical Computer Vision*, 2010.

[57] L. Ibanez, W. Schroeder, L. Ng, and J. Cates, *The ITK Software Guide*. Kitware, Inc, 2005.

[58] W. R. Crum and T. Hartkens, "Non-rigid image registration: Theory and practice," *British Journal of Radiology*, vol. 77, pp. 140–153, 2004.

[59] S. Klein and M. Staring, "elastix, the manual," 2012.

[60] D. Rueckert, L. Sonoda, C. Hayes, D. Hill, M. Leach, and D. Hawkes, "Nonrigid registration using free-form deformations: application to breast MR images," *IEEE Transactions on Medical Imaging*, vol. 18, no. 8, pp. 712 –721, aug. 1999.

[61] K. Cao, K. Ding, G. Christensen, M. Raghavan, R. Amelon, and J. Reinhardt, "Unifying vascular information in intensity-based nonrigid lung CT registration," in *Biomedical Image Registration*, B. Fischer, B. Dawant, and C. Lorenz, eds., vol. 6204 of *Lecture Notes in Computer Science*, pp. 1–12, Springer Berlin Heidelberg, 2010.

[62] K. Cao, K. Ding, J. M. Reinhardt, and G. E. Christensen, "Improving intensity-based lung ct registration accuracy utilizing vascular information," *International journal of biomedical imaging*, vol. 2012, 2012.

[63] Y. Yin, E. A. Hoffman, and C.-L. Lin, "Mass preserving nonrigid registration of CT lung images using cubic B-spline," *Medical Physics*, vol. 36, no. 9, pp. 4213–4222, 2009.

[64] V. Gorbunova, P. Lo, H. Ashraf, A. Dirksen, M. Nielsen, and M. de Bruijne, "Weight preserving image registration for monitoring disease progression in lung CT," in *MICCAI*, vol. 5242, pp. 863–870, 2008.

[65] K. Cao, G. E. Christensen, K. Ding, and J. M. Reinhardt, "Intensity-and-landmark-driven, inverse consistent, B-spline registration and analysis for lung imagery," in *Second International Workshop on Pulmonary Image Analysis*, 2009.

[66] K. Cao, *Mechanical analysis of lung CT images using nonrigid registration*. PhD thesis, University of Iowa, 2012.

[67] R. H. Byrd, P. Lu, J. Nocedal, and C. Zhu, "A limited memory algorithm for bound constrained optimization," *SIAM J. Sci. Comput.*, vol. 16, no. 5, pp. 1190–1208, 1995.

[68] Y. Choi and S. Lee, "Injectivity conditions of 2D and 3D uniform cubic B-spline functions," *Graphical Models*, vol. 62, no. 6, pp. 411–427, 2000.

[69] M. Modat, J. McClelland, and S. Ourselin, "Lung registration using the NiftyReg package," in *Grand Challenges in Medical Image Analysis*, 2010.

[70] S. Ourselin, A. Roche, G. Subsol, X. Pennec, and N. Ayache, "Reconstructing a 3D structure from serial histological sections," *Image and Vision Computing*, vol. 19, no. 1-2, pp. 25–31, Dec. 2000.

[71] M. Staring, S. Klein, J. H. Reiber, W. J. Niessen, and B. C. Stoel, "Pulmonary image registration with elastix using a standard intensity-based algorithm," in *Grand Challenges in Medical Image Analysis*, 2010.

[72] X. Han, "Feature-constrained nonlinear registration of lung CT images," in *Grand Challenges in Medical Image Analysis*, 2010.

[73] G. Song, N. Tustison, B. Avants, and J. C. Gee, "Lung CT image registration using diffeomorphic transformation models," in *Grand Challenges in Medical Image Analysis*, 2010.

[74] S. Kabus and C. Lorenz, "Fast elastic image registration," in *Grand Challenges in Medical Image Analysis*, 2010.

[75] T. Guerrero, G. Zhang, T. C. Huang, and K. P. Lin, "Intrathoracic tumour motion estimation from CT imaging using the 3D optical flow method," *Phys Med Biol*, vol. 49, no. 17, pp. 4147–4161, Sep 2004.

[76] G. Janssens, J. O. de Xivry, S. Fekkes, A. Dekker, B. Macq, P. Lambin, and W. van Elmpt, "Evaluation of nonrigid registration models for interfraction dose accumulation in radiotherapy," *Med Phys*, vol. 36, no. 9, pp. 4268–4276, Sep 2009.

[77] T. Vercauteren, X. Pennec, A. Perchant, and N. Ayache, "Diffeomorphic demons: efficient non-parametric image registration," *Neuroimage*, vol. 45, no. 1 Suppl, pp. 61–72, Mar 2009.

[78] E. Castillo, R. Castillo, J. Martinez, M. Shenoy, and T. Guerrero, "Four-dimensional deformable image registration using trajectory modeling," *Phys Med Biol*, vol. 55, no. 1, pp. 305–327, Jan 2010.

[79] C. T. Metz, S. Klein, M. Schaap, T. van Walsum, and W. J. Niessen, "Nonrigid registration of dynamic medical imaging data using nD + t B-splines and a groupwise optimization approach," *Med Image Anal*, vol. 15, no. 2, pp. 238–249, Apr 2011.

[80] J. Vandemeulebroucke, S. Rit, J. Kybic, P. Clarysse, and D. Sarrut, "Spatiotemporal motion estimation for respiratory-correlated imaging of the lungs," *Med Phys*, vol. 38, no. 1, pp. 166–178, Jan 2011.

[81] G. Wu, Q. Wang, J. Lian, and D. Shen, "Estimating the 4D respiratory lung motion by spatiotemporal registration and building super-resolution image," *Med Image Comput Comput Assist Interv*, vol. 14, no. Pt 1, pp. 532–539, 2011.

[82] G. Wu, Q. Wang, J. Lian, and D. Shen, "Estimating the 4D respiratory lung motion by spatiotemporal registration and super-resolution image reconstruction," *Medical Physics*, vol. 40, no. 3, p. 031710, 2013.

[83] K. Ding, K. Cao, M. K. Fuld, K. Du, G. E. Christensen, E. A. Hoffman, and J. M. Reinhardt, "Comparison of image registration based measures of regional lung ventilation from dynamic spiral CT with Xe-CT," *Med Phys*, 2012.

[84] R. Amelon, K. Cao, K. Ding, G. E. Christensen, J. M. Reinhardt, and M. L. Raghavan, "Three-dimensional characterization of regional lung deformation," *J Biomech*, vol. 44, no. 13, pp. 2489–2495, Sep 2011.

[85] J. R. Taylor, *An Introduction Error Analysis: The Study of Uncertainties in Physical Measurements*. University science books, 1997.

[86] T. Yamamoto, S. Kabus, J. von Berg, C. Lorenz, M. P. Chung, J. C. Hong, B. W. Loo, and P. J. Keall, "Reproducibility of four-dimensional computed tomography-based lung ventilation imaging," *Acad Radiol*, vol. 19, no. 12, pp. 1554–1565, Dec 2012.

[87] K. Du, J. E. Bayouth, K. Cao, G. E. Christensen, K. Ding, and J. M. Reinhardt, "Reproducibility of registration-based measures of lung tissue expansion," *Med. Phys.*, vol. 39(3), 2012.

[88] K. Du, J. E. Bayouth, K. Ding, G. E. Christensen, K. Cao, and J. M. Reinhardt, "Reproducibility of intensity-based measures of lung ventilation," *Medical Physics*, vol. (accepted), 2013.

[89] T. Yamamoto, S. Kabus, J. von Berg, C. Lorenz, and P. J. Keall, "Impact of four-dimensional computed tomography pulmonary ventilation imaging-based functional avoidance for lung cancer radiotherapy," *Int. J. Radiat. Oncol. Biol. Phys.*, vol. 79, no. 1, pp. 279–288, Jan 2011.

[90] H. Zhong, J. Y. Jin, M. Ajlouni, B. Movsas, and I. J. Chetty, "Measurement of regional compliance using 4DCT images for assessment of radiation treatment," *Med Phys*, vol. 38, pp. 1567–1578, Mar 2011.

[91] Y. Y. Vinogradskiy, R. Castillo, E. Castillo, A. Chandler, M. K. Martel, and T. Guerrero, "Use of weekly 4DCT-based ventilation maps to quantify changes in lung function for patients undergoing radiation therapy," *Medical Physics*, vol. 39, no. 1, pp. 289–298, 2012.

[92] T. B. Nyeng, J. F. Kallehauge, M. Høyer, J. B. Petersen, P. R. Poulsen, and L. P. Muren, "Clinical validation of a 4D-CT based method for lung ventilation measurement in phantoms and patients," *Acta Oncol*, vol. 50, pp. 897–907, Aug 2011.

[93] K. Murphy, B. van Ginneken, J. Reinhardt, S. Kabus, K. Ding, X. Deng, K. Cao, K. Du, G. Christensen, V. Garcia, T. Vercauteren, N. Ayache, O. Commowick, G. Malandain, B. Glocker, N. Paragios, N. Navab, V. Gorbunova, J. Sporring, M. de Bruijne, X. Han, M. Heinrich, J. Schnabel, M. Jenkinson, C. Lorenz, M. Modat, J. McClelland, S. Ourselin, S. Muenzing, M. Viergever, D. De Nigris, D. Collins, T. Arbel, M. Peroni, R. Li, G. Sharp, A. Schmidt-Richberg, J. Ehrhardt, R. Werner, D. Smeets, D. Loeckx, G. Song, N. Tustison, B. Avants, J. Gee, M. Staring, S. Klein, B. Stoel, M. Urschler, M. Werlberger, J. Vandemeulebroucke, S. Rit, D. Sarrut, and J. Pluim, "Evaluation of Registration Methods on Thoracic CT: The EMPIRE10 Challenge," *IEEE Trans Med Imaging*, May 2011.

[94] T. Waldron, J. Bayouth, S. Bhatia, and J. Buatti, "Use of music-based breathing training to stabilize breathing motion in respiration correlated imaging and radiation delivery," *Int. J. Radiat. Oncol. Biol. Phys.*, vol. 72, no. 1, Supplement 1, pp. S659 – S659, 2008.

[95] T. Yamamoto, U. Langner, B. W. Loo, J. B. Shen, and P. J. Keall, "Retrospective analysis of artifacts in four-dimensional CT images of 50 abdominal and thoracic radiotherapy patients," *Int. J. Radiat. Oncol. Biol. Phys.*, vol. 72, pp. 1250–1258, 2008.

[96] D. Han, J. Bayouth, S. Bhatia, M. Sonka, and X. Wu, "Characterization and identification of spatial artifacts during 4D-CT imaging," *Medical Physics*, vol. 38, pp. 2074–2087, 2011.

[97] K. Cao, K. Ding, G. E. Christensen, and J. M. Reinhardt, "Tissue volume and vesselness measure preserving nonrigid registration of lung CT images," in *Proc. SPIE 7623, 762309*, 2010.

[98] K. Cao, K. Du, K. Ding, J. M. Reinhardt, and G. E. Christensen, "Regularized nonrigid registration of lung CT images by preserving tissue volume and vesselness measure," in *Medical Image Analysis for the Clinic: A Grand Challenge*, 2010.

[99] K. Murphy, B. van Ginneken, S. Klein, M. Staring, B. de Hoop, M. Viergever, and J. Pluim, "Semi-automatic construction of reference standards for evaluation of image registration," *Medical Image Analysis*, vol. 15(1), pp. 71–84, 2011.

[100] K. Ding, K. Cao, R. E. Amelon, G. E. Christensen, M. L. Raghavan, and J. M. Reinhardt, "Comparison of intensity- and Jacobian-based estimates of lung regional ventilation," in *Third International Workshop on Pulmonary Image Analysis*, 2010.

[101] J. Adler, *R in a Nutshell*. O'Reilly Media, 2010.

[102] S. B. Shaker, A. Dirksen, L. C. Laursen, L. T. Skovgaard, and N. Holstein-Rathlou, "Volume adjustment of lung density by computed tomography scans in patients with emphysema," *Acta Radiol*, vol. 45(4), pp. 417–423, 2004.

[103] P. O. Alderson and B. R. Line, "Scintigraphic evaluation of regional pulmoanry ventilation," *Semin. Nucl. Med.*, vol. 10, pp. 219–42, 1980.

[104] W. M. Burch, P. J. Sullivan, and C. J. Mclaren, "Technegas - a new ventiltion agent for lung scanning," *Nucl. Med. Commun*, vol. 7, pp. 865–71, 1986.

[105] K. Suga, "Technical and analytical advances in pulmonary ventilation SPECT with xenon-133 gas and tc-99m-technegas," *Annals of Nuclear Medicine*, vol. 16, no. 5, pp. 303 – 310, 2002.

[106] E. H. Fleming, "Functions of several variables," in *(New York: Springer)*, 1977.

[107] E. A. Hoffman and E. L. Ritman, "Effect of body orientation on regional lung expansion in dog and sloth," *J Appl Physiol*, vol. 59, no. 2, pp. 481–491, 1985.

[108] E. A. Hoffman, J. M. Reinhardt, M. Sonka, B. A. Simon, J. Guo, O. Saba, D. Chon, S. Samrah, H. Shikata, J. Tschirren, K. Palagyi, K. C. Beck, and G. McLennan, "Characterization of the interstitial lung diseases via density-based and texture-based analysis of computed tomography images of lung structure and function," *Academic Radiology*, vol. 10, no. 10, pp. 1104 – 1118, 2003.

[109] K. Du, K. Ding, K. Cao, J. E. Bayouth, G. E. Christensen, and J. M. Reinhardt, "Registration-based measurement of regional expiration volume ratio using dynamic 4DCT imaging," in *Biomedical Imaging: From Nano to Macro, ISBI 2011. 8th IEEE International Symposium on Biomedical Imaging*, 2011.

[110] E. A. Hoffman, "Effect of body orientation on regional lung expansion: a computed tomographic approach," *J. Appl. Physiol.*, vol. 59, no. 2, pp. 468–480, Aug 1985.

[111] P. Bevington and D. Robinson, *Data reduction and error analysis for the physical sciences*. New York: McGraw-Hill, Inc., 1992.

[112] J. L. Garcia-Ramirez, S. Mutic, J. F. Dempsey, D. A. Low, and J. A. Purdy, "Performance evaluation of an 85-cm-bore X-ray computed tomography scanner designed for radiation oncology and comparison with current diagnostic CT scanners," *Int. J. Radiat. Oncol. Biol. Phys.*, vol. 52, no. 4, pp. 1123–1131, Mar 2002.

[113] D. A. Low and J. F. Dempsey, "Evaluation of the gamma dose distribution comparison method," *Medical Physics*, vol. 30, pp. 2455–2464, 2003.

[114] J. Bayouth, K. Du, G. Christensen, B. Smith, J. Buatti, and J. Reinhardt, "Establishing a relationship between radiosensitivity of lung tissue and ventilation," *Int. J. Radiat. Oncol. Biol. Phys.: Proceedings of ASTRO's 54th Annual Meeting*, vol. 84, no. 3, Supplement, pp. S31 – S32, 2012.

[115] Y. Seppenwoolde, S. H. Muller, J. C. Theuws, P. Baas, J. S. Belderbos, L. J. Boersma, and J. V. Lebesque, "Radiation dose-effect relations and local recovery in perfusion for patients with non-small-cell lung cancer," *Int. J. Radiat. Oncol. Biol. Phys.*, vol. 47, pp. 681–690, Jun 2000.

[116] J. Zhang, J. Ma, S. Zhou, J. L. Hubbs, T. Z. Wong, R. J. Folz, E. S. Evans, R. J. Jaszczak, R. Clough, and L. B. Marks, "Radiation-induced reductions in regional lung perfusion: 0.1-12 year data from a prospective clinical study," *Int. J. Radiat. Oncol. Biol. Phys.*, vol. 76, pp. 425–432, Feb 2010.

[117] E. Rietzel, T. Pan, and G. T. Chen, "Four-dimensional computed tomography: image formation and clinical protocol," *Med Phys*, vol. 32, pp. 874–889, Apr 2005.

[118] S. S. Vedam, P. J. Keall, V. R. Kini, H. Mostafavi, H. P. Shukla, and R. Mohan, "Acquiring a four-dimensional computed tomography dataset using an external respiratory signal," *Phys Med Biol*, vol. 48, pp. 45–62, Jan 2003.

[119] B. Ohnesorge, T. Flohr, C. Becker, A. F. Kopp, U. J. Schoepf, U. Baum, A. Knez, K. Klingenbeck-Regn, and M. F. Reiser, "Cardiac imaging by means of electrocardiographically gated multisection spiral CT: initial experience," *Radiology*, vol. 217, no. 2, pp. 564–571, Nov 2000.

[120] K. Du, K. Ding, K. Cao, J. M. Reinhardt, G. E. Christensen, and J. E. Bayouth, "Evaluate reproducibility of 4DCT registration-based lung ventilation measurement with gamma comparison method," in *AAPM*, 2011.

[121] H. Bass, "The flow volume loop: normal standards and abnormalities in chronic obstructive pulmonary disease," *Chest*, vol. 63, pp. 171–176, Feb 1973.

[122] R. E. Hyatt, D. P. Schilder, and D. L. Fry, "Relationship between maximum expiratory flow and degree of lung inflation," *J Appl Physiol*, vol. 13, pp. 331–336, Nov 1958.

[123] L. Xing, B. Thorndyke, E. Schreibmann, Y. Yang, T. F. Li, G. Y. Kim, G. Luxton, and A. Koong, "Overview of image-guided radiation therapy," *Med Dosim*, vol. 31, no. 2, pp. 91–112, 2006.